UNIVERSITY OF OKLAHOMA

GRADUATE COLLEGE

X-RAY SPECTRAL ANALYSIS IN X-RAY FLUORESCENCE IMAGING FOR BREAST CANCER DETECTION

A DISSERTATION

SUBMITTED TO THE GRADUATE FACULTY

in partial fulfillment of the requirements for the

Degree of

DOCTOR OF PHILOSOPHY

By

LIQIANG REN
Norman, Oklahoma
2016

X-RAY SPECTRAL ANALYSIS IN X-RAY FLUORESCENCE IMAGING FOR BREAST CANCER DETECTION

A DISSERTATION APPROVED FOR THE
SCHOOL OF ELECTRICAL AND COMPUTER ENGINEERING

BY

Dr. Hong Liu, Chair

Dr. Xingru Wu

Dr. John Dyer

Dr. James Sluss

Dr. Bin Zheng

This dissertation is dedicated to my parents and sister.

Acknowledgements

First of all, I would like to express my sincere gratitude and respect to my supervisor, Dr. Hong Liu, for providing me the precious opportunity to be his student and offering me tireless guidance, constant support and continued encouragement throughout my doctoral study at the University of Oklahoma.

Then, I want to give my special thanks to Dr. Xingru Wu, Dr. John Dyer, Dr. James Sluss and Dr. Bin Zheng for their time and contributions serving on my Ph.D. Program Committee.

I also appreciate the helpful discussions and friendship with all the other lab members: Dr. Yuhua Li, Dr. Molly Wong, Zheng Li, Di Wu and Ghani U. Muhammad in Dr. Hong Liu’s lab, Dr. Maxine Tan, Faranak Aghaei, Nastaran Emaminejad, Yunzhi Wang, Rohith Reddy Gundreddy and Dr. Yuchen Qiu in Dr. Bin Zheng’s lab, and Dr. Liangzhong Xiang, Dr. Shanshan Tang, Dr. Jian Chen and Pratik Samant in Dr. Liangzhong Xiang’s lab. Special thanks give to Di Wu, who provides me a profusion of helpful suggestions regarding X-ray spectral measurement and 3D printing.

Last, I would like to acknowledge the support by the grant from the University of Oklahoma Charles and Peggy Stephenson Cancer Center funded by the Oklahoma Tobacco Settlement Endowment Trust, and the support of the Charles and Jean Smith Chair endowment fund.

Table of Contents

List of Tables

List of Figures

Abstract

The knowledge of X-ray spectrum plays a major role in exploiting and optimizing the X-ray utilizations, especially in biomedical application fields. Over the past decades, extensive research efforts have been made in better characterizing the X-ray spectral features in experimental and simulation studies. The objectives of this dissertation are to investigate the applications of X-ray spectral measurement and analysis in X-ray fluorescence (XRF) and micro-computed tomography (micro-CT) imaging modalities, to facilitate the development of new imaging modalities or to optimize the imaging performance of currently available imaging systems.

The structure and primary discoveries of this dissertation are as follows: after a brief introduction of the objectives of this dissertation in Chapter 1, Chapter 2 gives a comprehensive background including electromagnetic properties, various applications, and different generation mechanisms of X-rays and their interactions with matter, X-ray spectral measurement and analysis methods, XRF principles and applications for cancer detection, and micro-CT system. Considering relatively high fluorescence production probability and sufficient penetrability of gold Kα fluorescence signals, Chapter 3 establishes a theoretical model of a gold nanoparticle (GNP) K-shell XRF imaging prototype consisting of a pencil-beam X-ray for excitation and a single collimated spectrometer for XRF detection. Then, the optimal energy windows of 66.99 ± 0.56keV and 68.80 ± 0.56keV for two gold Kα fluorescence peaks are determined in Chapter 4. Also, the linear interpolation method for background estimation under the Kα fluorescence peaks is suggested in this chapter. Chapters 5 and 6 propose a novel XRF based imaging modality, X-ray fluorescence mapping (XFM) for the purpose of breast

cancer detection, especially emphasizing on the detection of breast tumor located posteriorly, close to the chest wall musculature. The mapping results in these two chapters match well with the known spatial distributions and different GNP concentrations in 2D/3D reconstructions. Chapter 7 presents a method for determining the modulation transfer function (MTF) in XRF imaging modality, evaluating and improving the imaging performance of XFM. Moreover, this dissertation also investigates the importance of X-ray spectral measurement and analysis in a rotating gantry based micro-CT system. A practical alignment method for X-ray spectral measurement is first proposed using 3D printing technology in Chapter 8. With the measured results and corresponding spectral analysis, Chapter 9 further evaluates the impact of spectral filtrations on image quality indicators such as CT number uniformity, noise, and contrast to noise ratio (CNR) in the micro-CT system using a mouse phantom comprising 11 rods for modeling lung, muscle, adipose, and bones (various densities). With a baseline of identical entrance exposure to the imaged mouse phantom, the CNRs are degraded with improved beam quality for bone with high density and soft tissue, while are enhanced for bone with low density, lung, and muscle. Finally, Chapter 10 summarizes the whole dissertation and prospects the future research directions.

Chapter 1: Introduction

1.1 Objective

Since the discovery of X-rays by Roentgen in 1895, they have been widely utilized in various areas such as medicine, security, astronomy, industrial application and scientific research [1-6]. X-rays can be primarily generated by conventional X-ray tubes, synchrotron radiation facilities, and radioactive isotopes [7-9]. The knowledge of X-ray spectrum plays an important role in evaluating and optimizing the X-ray utilizations, especially in biomedical application fields such as calculating the radiation dose delivered to the object, optimizing imaging parameters, selecting spectral filtrations, and improving dual- or multi-energy imaging performances [10-13].

Over the past decades, great deals of researches have been performed to better characterize the X-ray spectral features, including direct methods with gas-filled, scintillation-based and semiconductor-based spectrometers, and indirect methods based on transmission measurement, Compton scattering and computer simulation [14-19]. Considering the high detection efficiency and excellent energy resolving power, a direct spectral measurement method using cadmium telluride (CdTe) spectrometer is employed in this dissertation, in an effort to investigate the applications of X-ray spectral measurement and analysis in X-ray fluorescence (XRF) and micro-computed tomography (micro-CT) imaging modalities, facilitating the development of new imaging modalities or optimizing the imaging performance of currently available imaging systems [13, 20, 21].

1.2 Organization of the dissertation

This dissertation focuses on applying X-ray spectral measurement and analysis in XRF and micro-CXT imaging modalities, as aforementioned. The structure of the subsequent chapters in this dissertation is organized as following:

Chapter 2 first describes the properties, applications, and generation mechanisms of X-rays, and their interactions with matter such as scattering and absorption. Second, two types of X-ray spectral measurement methods are introduced: direct and indirect methods. Also, energy calibration and quantitative analysis methods such as background removal, energy resolution determination, measurement uncertainty, and mean energy computation in an X-ray spectrum are discussed. The third part of this chapter provides the background of XRF spectroscopic analysis and its application for cancer detection. Last, the importance and difficulty of X-ray spectral measurement and analysis in a rotating gantry based micro-CT system are introduced.

Chapter 3 starts with a theoretical analysis of gold XRF mechanism and preliminary experimental validation of the penetrability of the gold XRF fluorescence peaks, based on which two K-shell gold XRF fluorescence peaks, $K_{\alpha 2}$ and $K_{\alpha 1}$, show great interests. Then, a standard gold K-shell XRF imaging prototype consisting of a pencil-beam X-ray from a polychromatic source for sample excitation and a collimated spectrometer detector placed at a right angle with respect to the axis of the excitation beam is established. The challenges of realizing a quantitative analysis of gold nanoparticle (GNP) concentrations are discussed as well.

Though a good estimation of background below each fluorescence peak can be obtained experimentally through acquiring the background spectrum of a water solution, it inevitably leads to an unnecessary second exposure in reality. Therefore, Chapter 4 first determines the optimal energy windows and corresponding neighboring energy bins for each of the gold K-shell fluorescence peaks using fluorescence-only spectra acquired in an experimental way. Then, several numerical methods such as trapezoidal shape estimation, interpolation by polynomial fitting and SNIP (Statistics sensitive Nonlinear Iterative Peak-Clipping) algorithm are performed on the original spectra acquired from GNP solutions to estimate the background. The optimal energy windows and background estimation method determined in this chapter will be adopted in the following chapters.

Chapter 5 investigates the feasibility of applying K-shell XRF technique to early breast cancer diagnosis and treatment using a novel approach for three-dimensional (3D) X-ray fluorescence mapping (XFM) of GNP-loaded objects in a physical phantom at the technical level. All the theoretical analysis and experiments are conducted under the condition of using X-ray pencil beam and a compactly integrated X-ray spectrometer. A physical phantom made of BR12 (breast tissue mimicking phantom: 47% glandular/53% adipose, Oprax Medical Inc., Southern California, US) is designed to translate in 3D space with three precise linear stages and subsequently a step by step XFM scanning is performed. The reconstructed mapping results indicate that both of the spatial distribution and the relative concentration of the embedded GNPs can be well identified and quantified.

Chapter 6 demonstrates the proof of concept of XFM imaging to address the issue of accurately depicting breast tumors located posteriorly, close to the chest wall musculature, which is a technical challenge with conventional mammography. A tissue-equivalent gel phantom is designed to mimic structures in the central part of a compressed breast. The posterior aspect of the breast and adjacent pectoralis major muscle are represented by another 10-mm-thickness BR12 that is attached to the back of the gel phantom as a region of interest (ROI). Two GNP solutions are embedded into the ROI to simulate varying GNP uptake within breast lesions. The ROI is imaged through performing the XFM technique with an X-ray pencil-beam and a single spectrometer. A 2D mapping of the middle plane in the ROI demonstrates the feasibility and matches well with the known spatial distributions and the GNP concentrations. 3D reconstruction of the ROI is easily rendered by repeating the 2D mapping process.

Chapter 7 describes a method for determining the modulation transfer function (MTF) in direct XFM imaging. With a standard container filled with homogeneous GNP solution (1% mass percentage), sharp edges are formed and utilized to acquire the data for edge spread function (ESF). Through necessary data processing, MTF can be determined. Influencing factors of MTF determination in XFM imaging are thoroughly discussed in theory and validated by experiments.

Chapter 8 presents a practical alignment method for X-ray spectral measurement in a rotating gantry based micro-CT system using 3D printing technology. In order to facilitate the placement of spectrometer inside the gantry, supporting structures including a cover and a stand are dedicatedly designed and printed using a 3D printer. According to the relative position between the spectrometer system and the stand, the upright projection of the spectrometer collimator onto the stand is determined and then marked by a tungsten pinhole. Thus, a visible alignment indicator of the X-ray central beam and the spectrometer collimator represented by the pinhole can be established under the micro-CT live mode (projection view). Then, a rough alignment is achieved through repeatedly adjusting and imaging the stand until the pinhole is located at the center of the acquired projection image. With the spectrometer being positioned back onto the stand, the precise alignment is completed by slightly translating the spectrometer-stand assembly around the rough location, until finding a “sweet spot” with the highest photon rate and proper distribution of the X-ray photons in the resultant spectrum.

Chapter 9 aims to evaluate the impact of spectral filtrations on image quality in the micro-CT system described in the previous chapter. A mouse phantom comprising 11 rods for modeling lung, muscle, adipose, and bones is scanned with 17 s and 2 min, respectively. The current (μA) for each scan is adjusted to achieve identical entrance exposure to the phantom, providing a baseline for image quality evaluation. For each ROI within specific composition, CT number variations, noise levels, and contrast-to-noise ratios (CNRs) are evaluated from the reconstructed images. CT number variations and CNRs for bone with high density, muscle, and adipose are compared with theoretical predictions.

Chapter 2: Background and basic concepts

2.1 X-ray and its properties

A typical electromagnetic (EM) radiation spectrum includes radio waves, microwaves, infrared light, visible light, ultraviolet light, X-rays, and gamma-rays, as indicated in Fig. 1. Three parameters are commonly used to characterize the EM radiation: wavelength (λ), frequency (ν), and energy (E), and they are correlated with each other by Eq. (1) [22].

$$E = h\nu = \frac{hc}{\lambda} \tag{1}$$

Where $h = 6.626 \times 10^{-34} J \cdot s = 4.136 \times 10^{-18} keV \cdot s$ is the Planck's constant. Particularly when E is expressed in kilo-electron-volts (keV) and λ in nanometers (nm), we simply have

$$E(keV) = \frac{1.24}{\lambda(nm)} \tag{2}$$

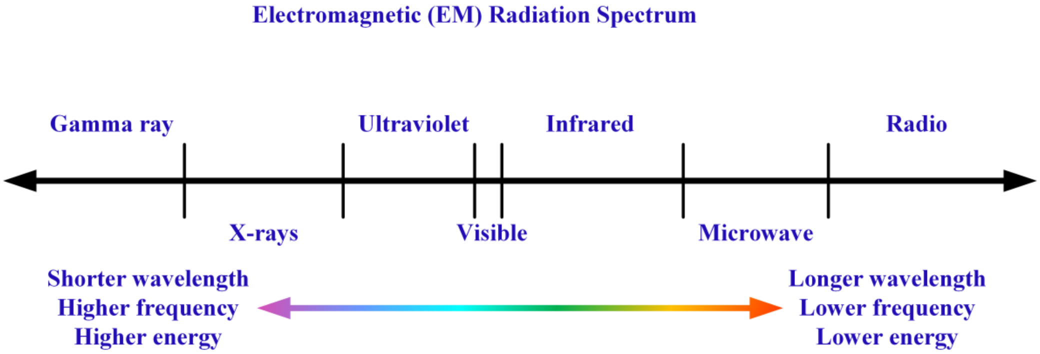

Figure 1. A typical electromagnetic (EM) radiation spectrum covering radio waves, microwaves, infrared light, visible light, ultraviolet light, X-rays, and gamma-rays.

As part of the EM radiation spectrum, X-rays have the same nature as other types of EM radiation such as ultraviolet, visible and infrared lights, but occupy a distinguishable range in wavelength from 10 to 0.01nm, corresponding to an energy ranging from around 0.1 to 120keV [22]. Note that the X-rays with higher energy could also be produced with different X-ray generation mechanisms [23]. Considering the specific EM radiation properties such as short wavelength and high energy, X-rays have a variety of applications, including but not limited to airport security inspection, astronomy, life science, drug discovery and research, computer chip design, chemical composition analysis, material crystallography, semiconductor material analysis, geological material analysis, cancer treatment and biomedical imaging [22, 24-26].

There are three major devices to generate X-rays: conventional X-ray tube, synchrotron radiation facility, and radioactive isotope.

2.1.1 X-rays generated using a conventional X-ray tube

A conventional X-ray tube typically consists of several core components: a heated filament cathode as an electron source, an empty vacuum providing the path for electron acceleration, an anode serving as the target of the electron, and a high voltage source applied between the cathode and the anode to supply a potential difference. Due to the high voltage between the electrodes, the electrons released from the filament surface are accelerated and attain kinetic energies, as they travel from the cathode to the anode in the vacuum. Then, these fast-moving electrons are suddenly decelerated and stopped by interactions with the target material, and during this process, a small fraction of the kinetic energy of these highly energetic electrons is converted into EM radiation and emitted in the form of X-ray photons, as demonstrated in Fig. 2 [8].

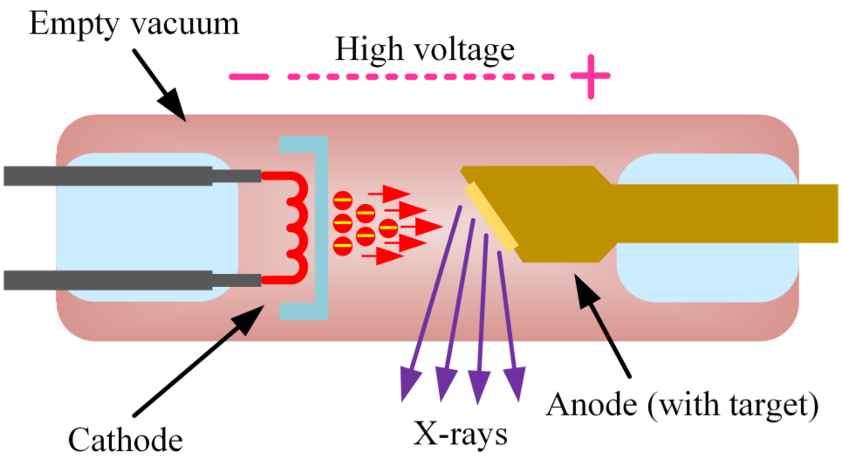

Figure 2. Schematic of a conventional X-ray tube consisting of a cathode, an anode, an empty vacuum path and a high voltage supply.

Since more than 90% of the electron kinetic energies give rise to heat after the interactions with the anode target rather than converting to EM radiation, the duration of X-ray production in a conventional X-ray tube, especially with a stationary anode configuration and at large tube current, must be limited. Therefore, conventional X-ray tubes designed with fixed anode are usually used in some mobile X-ray machines and fluoroscopy systems capable of tolerating small tube current and lower X-ray output.

In order to avoid overheating and produce high power X-rays, an efficient alternative is to employ a rotating anode configuration in the form of a cylinder, as utilized in most X-ray generators. In this way, the heat caused by the collision from the incident electrons is distributed over a cylindrical surface, which is a much larger area compared to that in a fixed anode configuration [27-30].

Attempts have been made to further improve the heat-management and optimize the X-ray source output. Typical examples include new micro-focus X-ray tubes with addition optical elements (1μS High Brilliance, Incoatec [31]) and liquid metal anodes

(MetalJet, Excillum [32]). Also, various types of X-ray tube head are developed for different imaging applications. For example, transmission tube head is used in the area of high resolution analysis [33], reflection tube head is to provide high power, while rod anode tubes offer the possibility of imaging the components where the area of interest is difficult to access [34]. However, the basic interaction mechanisms of the accelerated electrons with the target are similar in these aforementioned X-ray tubes, resulting in two kinds of radiation emission: bremsstrahlung (braking radiation) and characteristic emission.

Bremsstrahlung spectrum:

Braking radiation, or so-called bremsstrahlung, is intrinsically caused by the electrical force attraction from the atomic nucleus in the target material on the incident electrons, whose directions are thereby changed and part of the kinetic energies are lost and transformed to the emission of X-ray photons. The energy of each emitted X-ray photon is equal to the kinetic energy loss of the attracted electron, as determined by the distance between the target nucleus and that incident electron. In a very rare condition of a direct collision with the atomic nucleus, the electron losses all its kinetic energy converting to an X-ray photon with the maximum energy equal to that of the incident electron. In most cases, however, there is a distance between the target nucleus and incident electron and only part of the electron's kinetic energy is lost due to the electrical force attraction. Since that the electrical force is inversely proportional to the square of the nucleus-to-electron distance, the amount of the electron's energy loss (X-ray photon energy) gradually decreases with increased nucleus-to-electron distance.

This process of the X-ray production is called bremsstrahlung or braking radiation, of which the corresponding spectrum is a continuous distribution of emitted X-ray photons at a function of photon energy (keV) [22, 34].

Characteristic spectrum:

Characteristic radiation associated with the target atomic structure is also present during the interaction between the incident electrons and the target material. An atomic structure is given in Fig. 3 as an example, where all the electrons are distributed in different shells named as K, L, M, N and so on. Each shell has a specific electron binding energy which is a characteristic of the corresponding element. The binding energies for K, L, and M shells of two commonly used target material, tungsten (W) and molybdenum (Mo) are listed in Table. 1 [35].

Table 1. Electron binding energies for W and Mo (keV)

Electron shell	Tungsten (W: 74)	Molybdenum (Mo: 42)
K	69.5	20.0
L	10.2	~2.6
M	1.9	~0.45

When the energy of the incident electron exceeds the binding energy of an orbital electron, the orbital electron can be ejected from its original shell, leaving a vacancy on that shell and causing the atom in an excited state. In order to keep the atom stable, a second electron from an outer shell with less binding energy is immediately transferred to fill the vacancy. During this process, an X-ray photon is emitted with a characteristic energy equal to the binding energy difference between these two shells

[36, 37]. The characteristic lines for each shell are named in Fig. 3 as well. The competing process of Auger emission will be discussed later in this chapter.

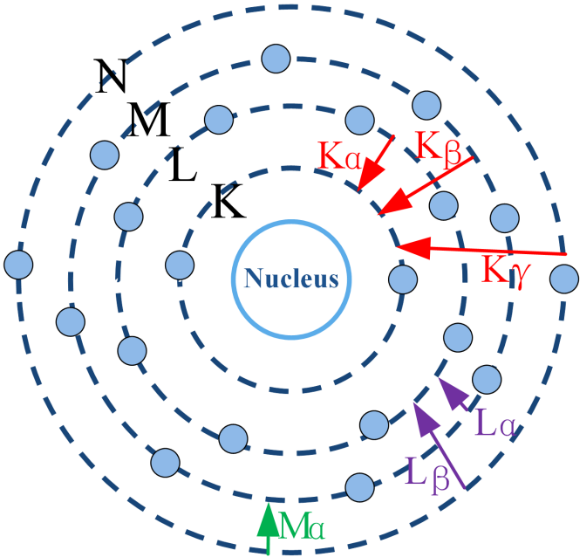

Figure 3. A typical atomic structure including nucleus and electrons; the characteristic lines for K, L and M shells are also indicated.

Characteristic X-rays are superimposed on the bremsstrahlung spectrum in a resultant X-ray spectrum. Two spectrum examples using W anode and under different voltages are shown in Fig. 4, where two K-shell characteristic peaks are present in the spectrum acquired under 100kVp (K shell binding energy of W: 69.2keV) while L-shell characteristic peaks are acquired in another spectrum with 40kVp (L shell binding energy of W: 10.2keV). Note that the characteristic peaks from L shell emission are omitted in the 100kVp spectrum for a better comparison with the one acquired under 40kVp.

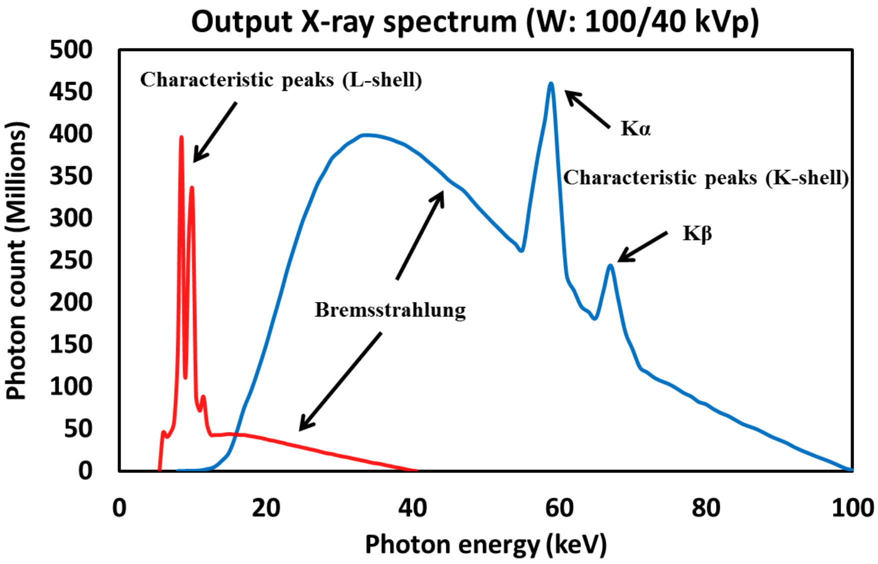

Figure 4. Spectra comparison with W anode under voltages of 40kVp and 100kVp.

Factors affecting the output X-ray spectrum:

The output X-ray spectrum can be affected by several factors including anode target material influencing the overall spectrum shape and characteristic peak energies, tube voltage (kVp) determining the maximum X-ray photon energy and the presence of characteristic peaks, tube current and exposure [mAs: milliamp (mA) times exposure time (s)], and intrinsic and/or additional filtrations removing the X-ray photons with lower energies [22].

Anode target material: The material of the anode target affects the bremsstrahlung radiation efficiency as well as the characteristic X-ray emission energies, due to the specific atomic structures [38]. Two spectra from an X-ray tube using W and Mo under identical voltage, current, and filtrations are presented in Fig. 5, showing the influence of different anode target materials.

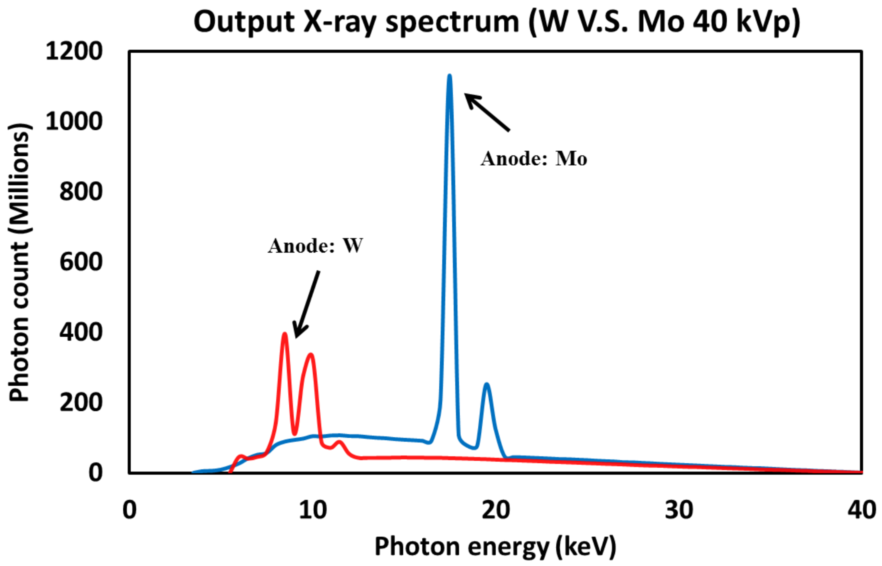

Figure 5. Spectra comparison with different target materials under 40kVp.

Tube voltage (kVp): Tube voltage not only determines the maximum energy level of the produced X-ray photons, as introduced above, but also significantly affects the quality of the output spectrum. The definition of X-ray beam quality as well as the corresponding evaluation methods such as half value layer (HVL) and mean energy will be discussed later in this chapter. Again, two X-ray spectra acquired under different tube voltages, 100kVp and 65kVp, are demonstrated in Fig. 6. Note that no characteristic peaks from K shell are produced with 65kVp because the maximum electron's kinetic energy is below the K shell binding energy of W atom (69.5keV). As an approximate estimation within the energy range between 20keV to 150keV, generally for diagnostic imaging, the X-ray tube output is proportional to the square of the applied tube voltage.

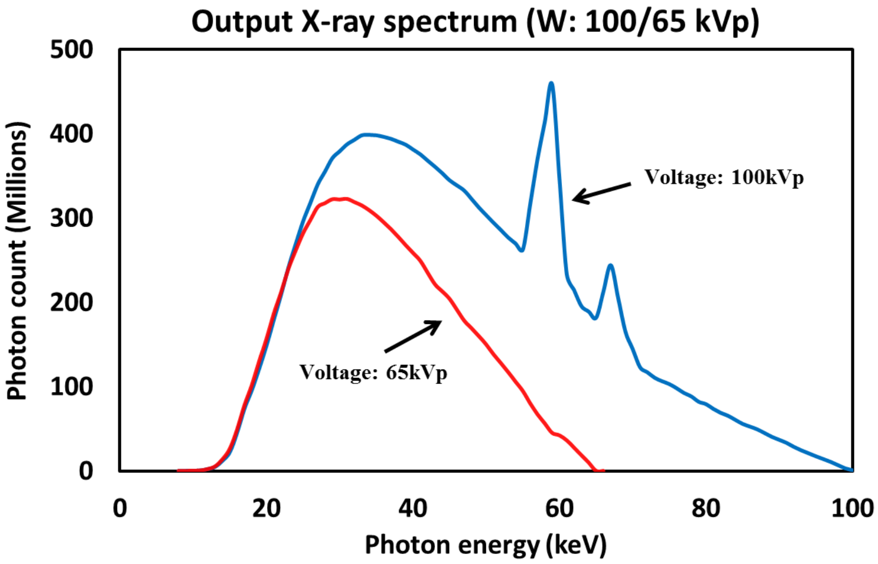

Figure 6. Spectra comparison with different voltages.

Tube current and exposure time (mAs): For a given target material and identical voltage and filtration settings, both of the tube current and the exposure time are proportional to the amount of electrons flowing from the cathode to the anode, and further proportional to the X-ray tube output. An example shown in Fig. 7 indicates a 3 times improvement of X-ray output when the mAs setting is increased by 3 times.

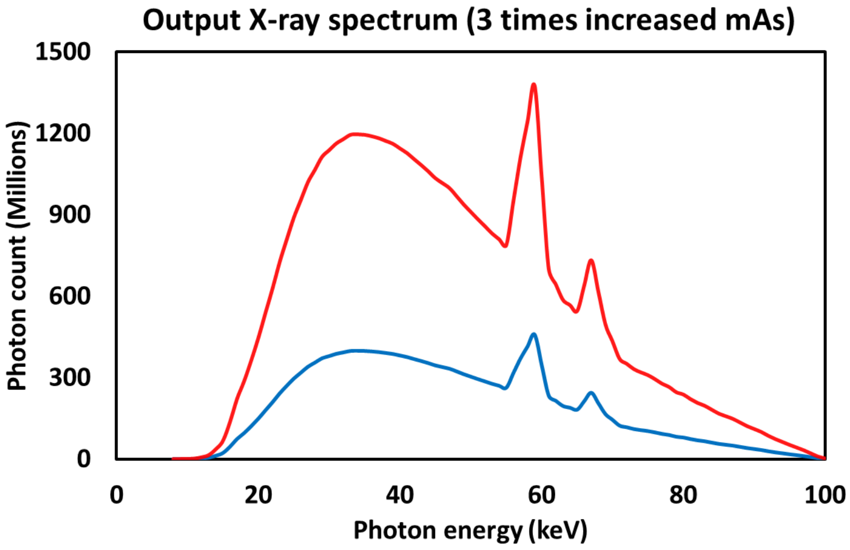

Figure 7. Spectra comparison with different mAs.

Beam filtration: Through preferentially removing the X-ray photons with lower energies, beam filtration influences both of the quality and quantity of the X-ray output spectrum. As observed in Fig. 8, applying additional 5mm aluminum (Al) filtration significantly increases the X-ray beam quality through blocking more low energy X-ray photons. More details regarding beam filtration will be discussed later in this chapter, emphasizing on its impacts and applications in diagnostic imaging. All the spectra data in Fig. 4-8 are acquired using a computer simulation tool, of which the algorithms are described in [38, 39], and note that all the characteristic X-ray peaks from L shell of W with a voltage above 40kVp are not provided.

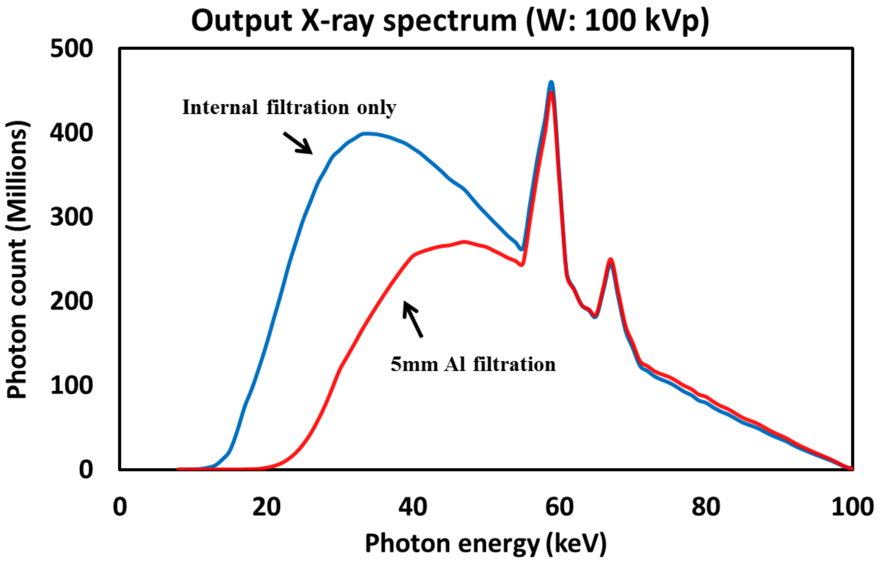

Figure 8. Spectra comparison with different filtrations; one is with internal filtration only while the other is with additional 5mm Al filtration.

2.1.2 X-rays generated using a synchrotron radiation facility

As a national user facility, synchrotron produces extremely powerful X-rays by highly energetic electrons circulating in a large circle [7, 40-42]. The mechanism of generating X-rays is quite different with that of using aforementioned conventional X-ray tubes. A typical synchrotron facility consists of four components: a linear accelerator, a booster synchrotron, a storage ring, and a beamline. The electrons produced in an electron gun are accelerated by the linear accelerator to a high kinetic energy and then injected into the booster synchrotron, where the electrons are further accelerated to a higher energy in GeV level and sent to the storage ring. The boosted electrons travel at nearly the speed of light in the storage ring and pass through different types of magnets forcing the path of the electrons to match the curvature of the storage ring. Due to the direction change and the consequent energy loss of the electrons when passing through the magnets, a very high energy radiation (synchrotron radiation) is emitted tangentially to the electron beam plane. The synchrotron emission from the bending magnet is composed of a wide and continuous spectrum ranging from microwaves to hard X-rays. The emitted radiation photons are then directed into different beamlines surrounding the storage ring for various types of experiments and investigations. A typical sketch of a synchrotron is demonstrated in Fig. 9, where only one set of bending magnet and beam line is presented for illustration.

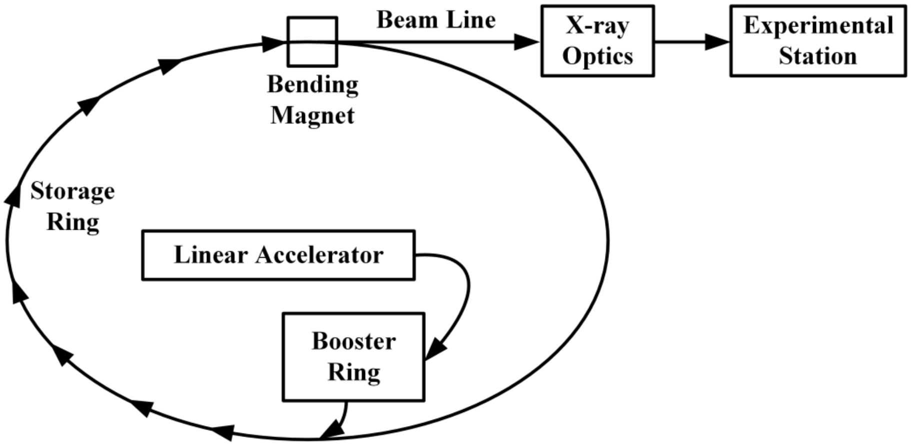

Figure 9. A typical sketch of a synchrotron consisting of linear accelerator, booster ring, storage ring and beam line.

The powerful synchrotron radiation provides the possibility to isolate a monochromatic beam with a single wavelength/energy from the polychromatic spectrum while maintaining a very high intensity. The isolation process is generally achieved by employing so-called monochromators based on Bragg's Law. The filtration of the original polychromatic radiation from synchrotron is completely determined by the interaction between X-rays and crystals within the monochromator.

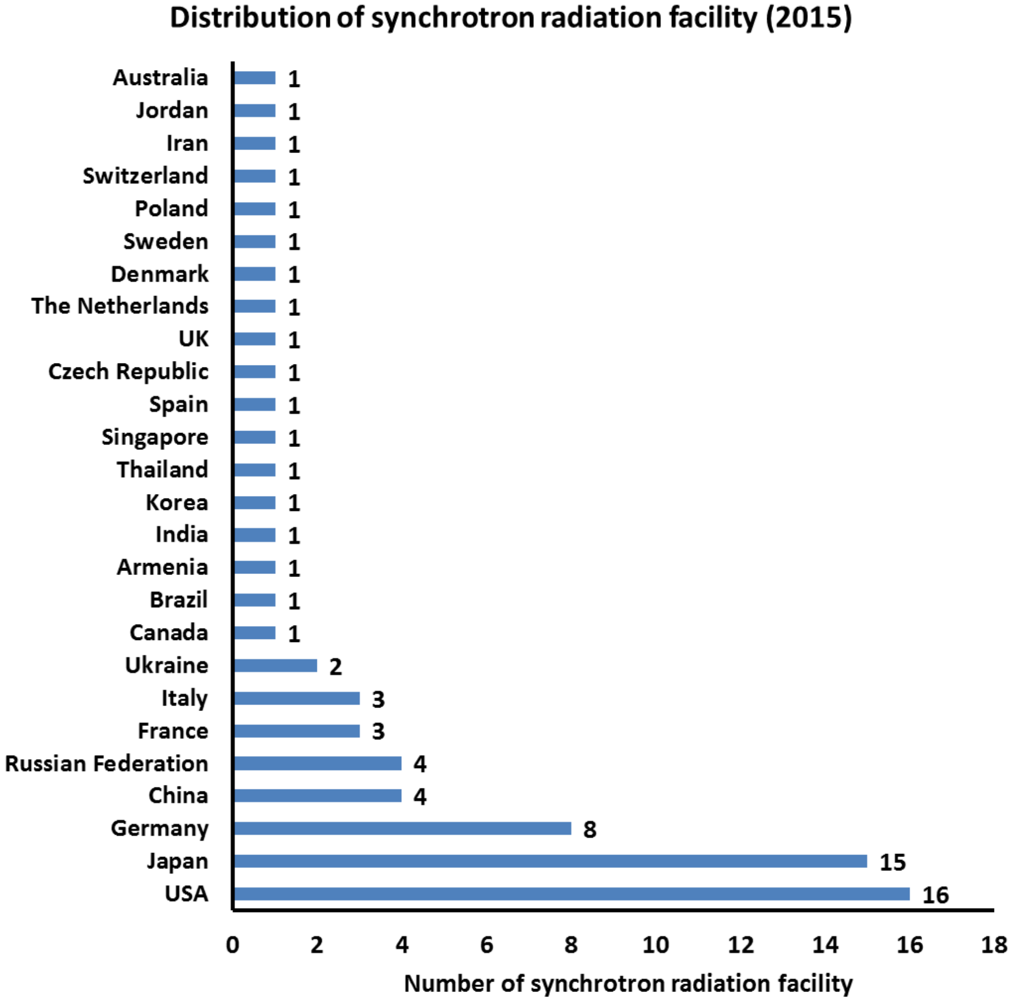

Figure 10. Distribution of synchrotron radiation facilities (data from lightsources.org).

Even though smaller synchrotron radiation facilities such as compact light source have been developed, the access of synchrotrons is still extremely limited, as shown in Fig. 10, for specific applications such as diagnostic imaging. That is the reason why the investigated XRF and micro-CT imaging systems in this dissertation employ conventional X-ray tubes rather than a synchrotron radiation facility.

2.1.3 X-rays generated using a radioactive isotope

A radioactive isotope, also called radioactive nuclide, radioisotope, or radionuclide, is an unstable atom with excess nuclear energy which is released through radioactive decay by emitting radiations in the form of alpha particles, beta particles, gamma rays and conversion electrons. Compared to alpha particles, beta particles and gamma rays those are directly emitted out from nucleus decay process, conversion electrons are occurred in one of the radioactive decay processes called internal conversion, during which the excess nuclear energy is transferred to one orbital electron of the unstable atom. Since the transferred energy, if larger than the binding energy of the electron, causes the electron to be ejected, a vacancy appears in that electron shell and can be filled by other electrons from outer shells. This process is identical to that of producing characteristic X-rays in conventional X-ray tubes, thus also creating characteristic X-rays corresponding to the unstable radioactive isotope [9, 43]. Another process that also emanates X-rays is called electron capture [44]. This process typically happens to a proton-rich isotope which captures or absorbs an inner-shell electron to form a neutron (proton + electron) and stabilize the nucleus. Analogous to internal conversion, this process also creates a hole at the original electron shell of captured electron and generates characteristic X-rays through electron transition. Therefore, those radioactive isotopes emitting X-rays during their decay process can be used as X-ray sources.

Compared to conventional X-ray sources and synchrotrons, radioactive isotopes are generally compact, portable, and more importantly, only have a few discrete energy values (characteristic X-rays) in the produced X-ray spectrum. However, this type of radiation source cannot be turned off and careful radiation protection must be provided constantly.

2.1.4 Interactions of X-rays with matter

When passing through the matter, part of the X-ray photons can penetrate without interaction, while part interacts with matter in terms of either scatter (Rayleigh scatter and Compton scatter) or absorption (photoelectric absorption), as described in Fig. 11 [22].

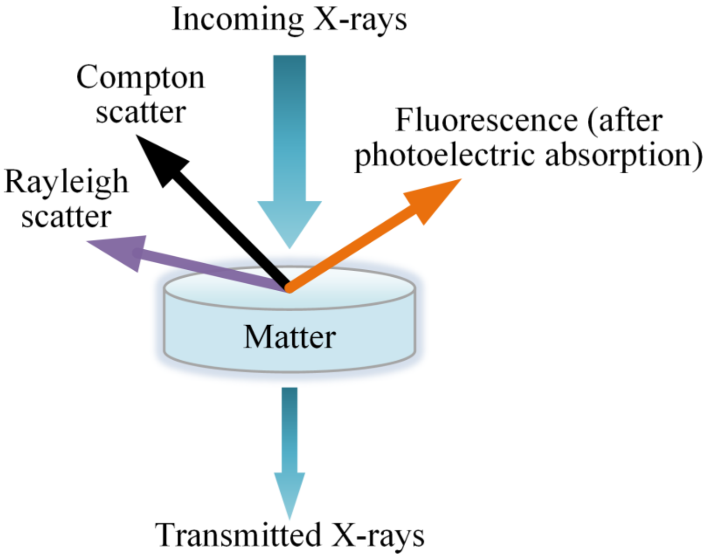

Figure 11. Part of the X-ray photons can penetrate without interaction, while part interacts with matter by scatter and absorption.

Rayleigh scatter: Rayleigh scatter, also called coherent or classical scatter, refers to the interaction of the incident X-ray photons with the total atom. During this interaction, all the electrons stay in their shells but the whole atom starts to oscillate in phase. Then, a photon with the same energy as the incident X-ray photon is immediately emitted in a different direction. This process seems like the incident X-ray photon is scattered by the atom [45, 46].

Compton scatter: Compton scatter, also called inelastic or non-classical scatter, indicates the interaction of incident X-ray photons with the orbital electrons. During this scattering process, an electron on the outer shell is most likely to be ejected from the atom becoming a Compton electron with a kinetic energy of $E_{ejected}$, and incident photon is scattered with a reduction of energy from E to E_c. Note that $E_{ejected} = E - E_c$ due to the energy conservation law, and the energy of the X-ray photon scattered into an angle of θ respect to the original direction can be determined using Eq. (3), where c and m_e are the light speed and electron mass, respectively [22].

$$E_c = \frac{E}{1 + (E / m_e c^2)(1 - \cos\theta)} \tag{3}$$

Photoelectric absorption: the classical model of an atom has been briefly introduced when discussing the generation of characteristic X-rays in conventional X-ray tubes. In this model, the nucleus (protons + neutrons) is surrounded by electrons which are located in discrete shells named as K, L, M, etc. During the process of photoelectric absorption, all the energy of the incident X-ray photon is absorbed and transferred to an electron, which is immediately ejected from atom with energy equal to the difference between the incident photon energy and the binding energy of the ejected electron. In order to eject an electron, the incident photon must have an energy which is greater than or at least equal to the electron’s binding energy [47-49]. Analogue to the process of ejecting an electron by fast-moving high energetic electron beam, photoelectric absorption creates a vacancy on the shell where the electron is ejected. The left vacancy will be filled by an electron from one of the outer shells and excess energy between these two shells will be released by either fluorescent emission or Auger electron emission. The details of X-ray fluorescence and Auger electron emission will be discussed later in this chapter with more details.

2.2 X-ray spectral measurement and analysis

2.2.1 The importance of X-ray spectral measurement and analysis

As aforementioned, the output X-rays from either conventional X-ray tubes or synchrotron radiation facilities cover a wide range of energy (wavelength) spectrum. Through accurately measuring the X-ray spectrum, full information regarding the distribution of X-ray photons at a function of photon energy can be acquired. The measurement and analysis of X-ray spectrum are of significant importance for quality assurance (QA) and quality control (QC) especially for the realm of diagnostic imaging systems, because the knowledge of X-ray spectrum is generally the prerequisite for calculating the radiation dose delivered to the patient [50], estimating tissue composition, optimizing imaging system parameters and performance, selecting spectral filtrations, and developing new imaging modalities such as X-ray spectral imaging and dual/multiple energy imaging [10-13, 50]. The acquisition methods of an X-ray spectrum can be categorized into two groups: direct and indirect methods.

2.2.2 Direct X-ray spectral measurement

The X-ray spectrum can be directly measured by a detecting device called spectrometer which yields a statistical distribution of the incident X-ray photons with respect to the photon energies. In order to illustrate the process of producing an X-ray spectrum using a spectrometer, several important terms are described below before introducing several types of spectrometers.

Interaction: the term of interaction typically refers to the interaction of a single X-ray photon with detector material by ionization or excitation.

Event: the term of event mostly refers to a single interaction, but sometimes two or more nearly simultaneous interactions may be also regarded as one event.

Pulse mode: pulse mode and current mode are two fundamental ways of the detection system to process the signal. Compared to the current mode which averages all the electrical signals form individual interactions, pulse mode processes each interaction individually. Spectrometer generally works in the pulse mode to distinguish the energy of each photon.

Count: the term of count indicates the number of the processed and registered interactions or events.

Gas-Filled Spectrometer:

As shown in Fig.12, a typical gas-filled detector consists of a volume filled with air or other gas, two electrodes (anode and cathode) with a voltage difference applied, and a measuring device of electrical current. The incident X-ray photons ionize the gas and create ion pairs (electrons and cations) which are then passed through the gas and attached to the electrodes. When the electrons travel in the circuit to recombine with the cations, an electrical current is generated and measured by a measuring device such as an ammeter [15].

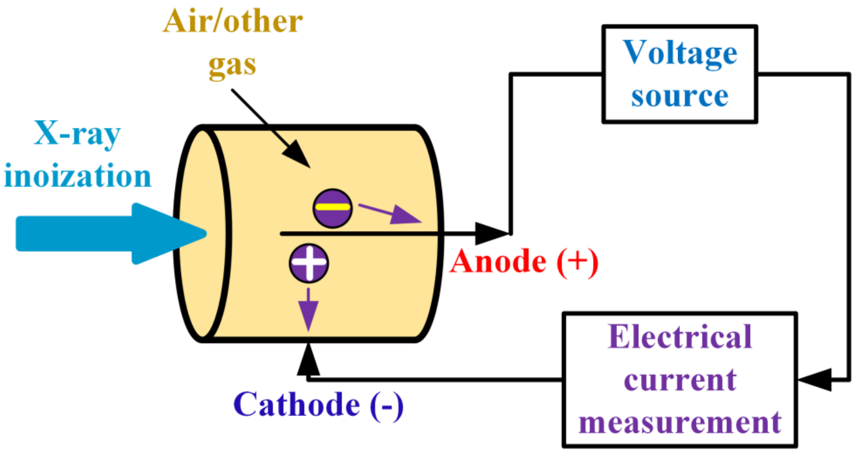

Figure 12. A typical gas-filled detector consists of an air volume, two electrodes with a voltage difference applied, and a current measuring device.

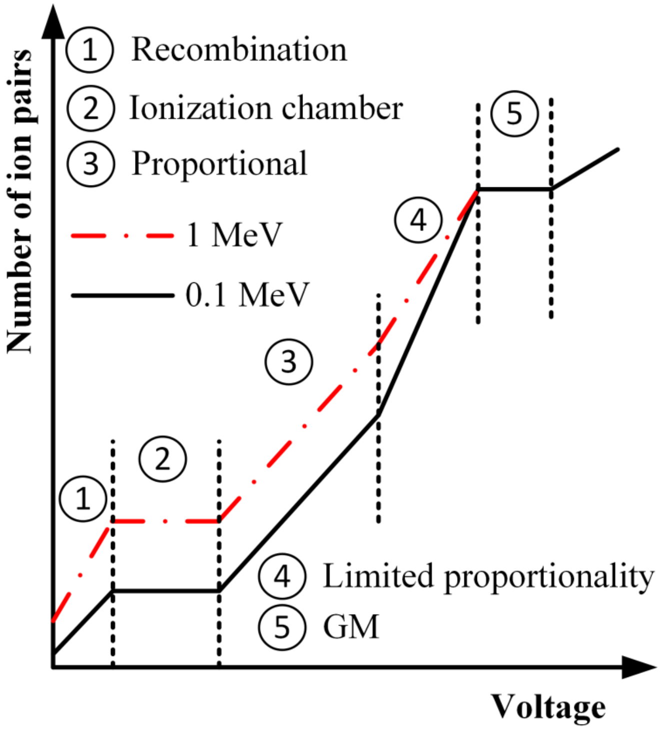

Figure 13. Working regions for ionization chambers, proportional counters and GM counters.

According to the voltage difference applied between two electrons, gas-filled detectors can be classified into three subtypes: ionization chambers, proportional counters, and Geiger-Mueller (GM) counters. The working regions for these three gas-fill detectors are indicated in Fig. 13, where no detectors work in the regions of recombination and limited proportionality [15].

In ionization and proportional regions where the ionization chambers and the proportional counters are operated, the amount of collected electrical charges is proportional to the energy deposited into the gas volume by each individual interaction. However, due to the lack of gas multiplication under a lower voltage range, the electrical charge amount from an individual interaction in an ionization chamber is difficult to detect. Thus, ionization chambers are mostly used in a current mode rather than in a pulse mode. On the contrary, proportional counters are capable of collecting enough amount of electrical charge for each interaction due to the gas multiplication, and potentially are able to work in a pulse mode as spectrometers. The restriction of utilizing proportional counters in spectroscopy is due to the low energy resolution, as will be introduced later in this chapter, caused by statistical fluctuations during both of the initial ionization and the subsequent gas multiplication processes. Since the collected ion pairs generated in a GM counter is independent of the energy deposition by the interaction, as shown in Fig. 13, GM counters typically provide no resolving capabilities of photon energies as spectrometers do, though they do work in a pulse mode.

Scintillation-based spectrometer:

Scintillation is the process that visible light or ultraviolet radiation is emanated from materials called scintillators during their interactions with incident X-ray photons. Though those light can be directly viewed by dark-adapted eyes, mostly the light photons are amplified and recorded either by photographic film or electronic devices such as photomultiplier tube (PMT) and image-intensifier tubes through converting them into electrical signals. The combination of a scintillator and a photographic film or electronic device composes a scintillation detector. Since the amount of emanated light photons is proportional to the deposited energy from each individual X-ray photon, scintillation detectors can be utilized as spectrometers when operating in the pulse mode. Scintillation-based spectrometers, such as thallium-doped sodium iodide [NaI(TI)] and bismuth germinate (BGO), are popularly used in nuclear imaging, due to their high quantum detection efficiencies (Z of iodine = 53 and Z of bismuth = 83) and the manufacturability into a large scale. However, scintillation-based spectrometers are commonly not employed for depicting fine structures from radiation-producing objects because of the poor energy resolution resulted from the relatively low conversion efficiency of scintillation [16].

Semiconductor-based spectrometer:

Semiconductor detectors (solid-state detectors) detect the electron-hole pairs generated in semiconductors due to the energy deposition from ionization radiation [14]. Fig. 14 shows the energy bands of semiconductor materials such as silicon and germanium, including a conduction band, a valence band, and a band gap between the two. Under normal conditions, all the electrons participate in covalent bonds in valence band while no electrons exist in the conduction band. The band gap between the conduction band and the valence band is about 1eV or less compared to that in an insulator (~5eV). Therefore, a flow of electrons from valence band to conduction band becomes possible if the valence-band electrons obtain enough energy from the interaction with high energy radiation such as X-rays, leaving a hole with positive charge at the valence band. This process described above in semiconductor is similar to that of generating ion pairs in a gas-filled detector.

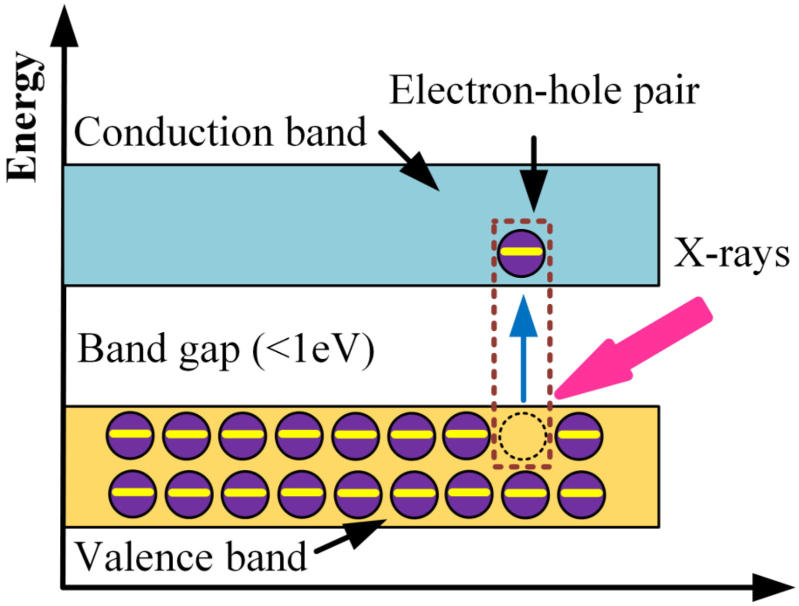

Figure 14. Energy bands in a semiconductor, including a conduction band, a valence band, and a band gap.

Through doping with a trace amount of impurities and applying a reversed external voltage, the reverse-biased semiconductor is able to detect a small radiation–induced current. Semiconductor detectors are functioned as spectrometers thanks to the proportionality between the radiation-induced current and the deposited energy by the interaction. Three major semiconductor-based spectrometers are introduced as below:

Semiconductor-based spectrometer using silicon (Si): the semiconductor-based spectrometer using Si is typically used as photodiodes to detect visible or ultraviolet light. They can be also applied to detect X-rays and gamma-rays but within a relatively low energy range (20keV~40keV), because of the low Z number (Z=14) of Si.

Semiconductor-based spectrometer using germanium (Ge): compared to the semiconductors using Si, Ge-based detectors provide superb absorption efficiency thanks to its relatively high Z number (Z=32). Therefore, this type of semiconductor is capable of detecting radiation up to several MeV. Moreover, high energy resolution could be achieved due to high conversion efficiency from deposited energy to charge carriers (ion pairs). However, requirement of cooling during the operation of this semiconductor spectrometer to minimize the noise caused by the thermal energy significantly limits its applications. Other drawbacks of this type of semiconductor detector include high expense and limitation on manufacturability into a large size.

Semiconductor-based spectrometer using cadmium telluride (CdTe) and cadmium zinc telluride (CdZnTe or CZT): CdTe and CZT are leading candidates utilized in semiconductor-based spectrometers to detect high energy radiations such as X-ray and gamma-ray because of their high densities, Z(Cd)=48, Z(Zn)=30 and Z(Te)=52 [51]. Considering a wide band gap and high resistivity of these materials, CdTe and CZT can be operated at room temperature or incorporated with a thermal-cooler to further reduce the electronic noise in the detector and the preamplifier.

Pulse height analyzer:

Pulse height analyzer is an important component capable of accepting and analyzing the electrical pulses generated by proportional counters, scintillation-based and semiconductor-based spectrometers. There are two types of pulse height analyzer: single-channel analyzer (SCA) and multichannel analyzer (MCA) [22].

Single-channel analyzer (SCA): in a SCA, basically two voltage levels are set to compare with the voltage pulse and only the one with pulse voltage height located between these two levels can be processed and registered. A spectrum is plotted through sweeping the voltage levels from low voltage to high voltage with a constant voltage window between two voltage levels.

Multichannel analyzer (MCA): compared to SCA, MCA acquires an energy spectrum much more quickly without a sweeping process of the voltage levels. A MCA typically consists of an analog-to-digital convertor (ADC) converting the voltage pulses after amplification into binary digital signals, a memory with many channels from 256 up to around 8k, a controlling circuitry, and a method for displaying the detected spectrum. For each converted digital signal which is proportional to the amplitude of the analog voltage pulse, the MCA assigns it to a designated channel in the memory. Nowadays, the spectrum acquisition process can be displayed and monitored on digital computers in real time.

The impact of count rate on spectrometer performance:

All the spectrometers must work based on single event, meaning that each time only one voltage pulse should be processed. The minimum time interval required to distinguish two adjacent interactions is called the dead time of the spectrometer, preventing the detection of the second pulse arrived within the dead time. Two mathematical models are used to describe the spectrometer performance if two voltage pulses are arrived within the dead time: paralyzable model and non-paralyzable model [52].

The dead time for each model can be determined using Eq. (4) - (6), where A_{rec} and A_{inc} are the recorded count rate and the incident count rate, respectively, $P(A_{inc}\tau)$ donates the probability of the counts being recorded, and τ is the dead time.

$$A_{rec} = A_{inc} \times P(A_{inc}\tau) \tag{4}$$

$$P(A_{inc}\tau)\,|_{\text{non-paralyzable}} = 1/(1 + A_{inc}\tau) \tag{5}$$

$$P(A_{inc}\tau)\,|_{\text{paralyzable}} = exp(-A_{inc}\tau) \tag{6}$$

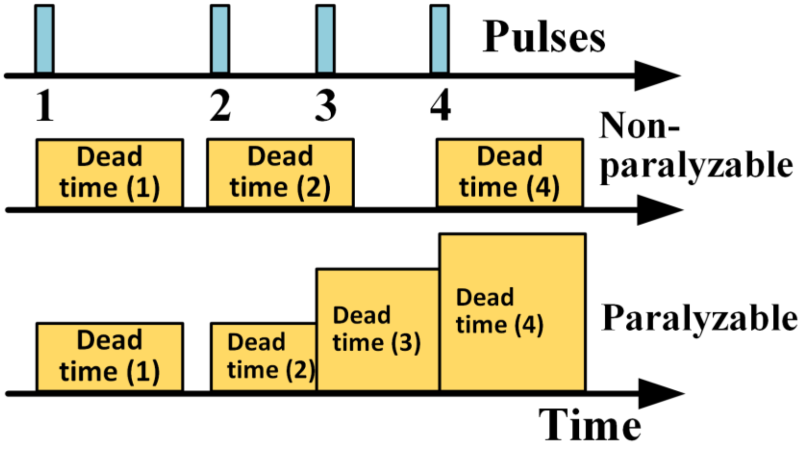

Figure 15. Illustration of two mathematical models describing the spectrometer performance.

The major difference between these two models is whether the latter interaction arrived within the dead time of the former one will extend the dead time. As illustrated in Fig. 15, the third pulse doesn’t extend the dead time caused by the second pulse in the non-paralyzable model, so that the spectrometer returns to an active state before processing the fourth pulse and totally three pulses are processed and registered. In contrast, only two pulses are registered in the analyzable model because the third pulse extends and the fourth pulse further extends the dead time. Note that in either model, part of the interactions occurred within the dead time can’t be processed and registered, such as pulse 3 in the non-paralyzable model and pulses 3 and 4 in paralyzable model. The overall detector behaviors described using two models are shown in Fig. 16.

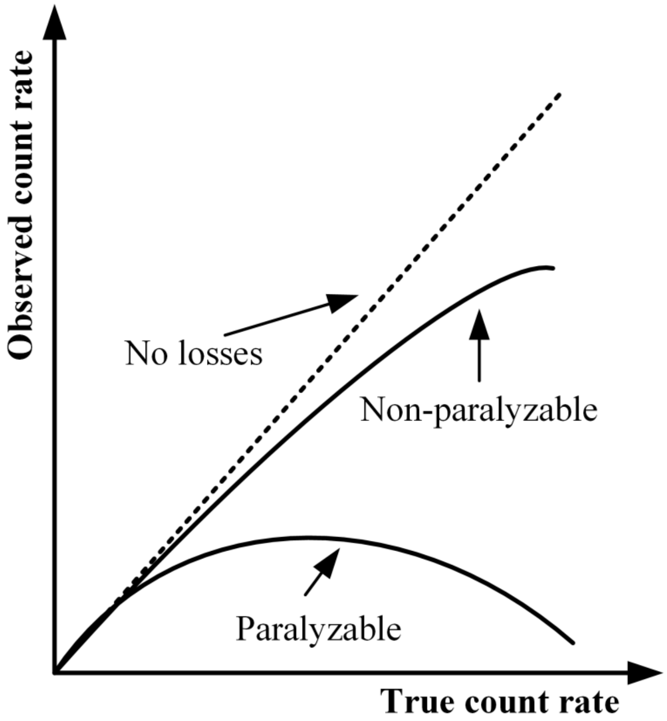

Figure 16. Count rate effect on spectrometer performance using non-paralyzable and paralyzable models.

On the other hand, if two or more nearly simultaneous interactions occur, they may be counted as one single pulse with larger amplitude, as shown below, the effect of which is called pile-up resulting in a misplacement of detected pulse and a distortion of the resultant spectrum. Pile-up effect becomes significant with increased count rate from the radiation sources and therefore, measuring strategies must be considered to reduce the count rate in direct X-ray spectral measurement [22].

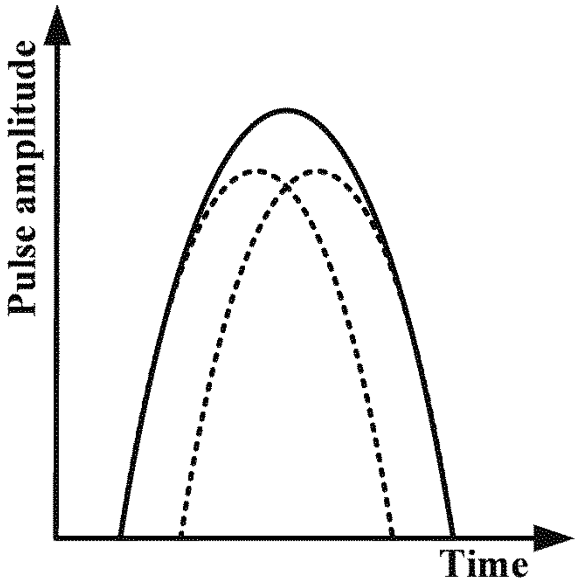

Figure 17. Schematic for pile-up effect with two nearly simultaneous incident pulses.

2.2.3 Indirect X-ray spectral measurement and estimation

Under certain clinical imaging circumstances, directly measuring the primary X-ray spectrum is very difficult because of the high photon flux (count rate) produced by X-ray tubes and the limited source-to-detector distance, such as in CT scanner and mammography. Therefore, indirect methods for X-ray spectral measurement and estimation have been proposed and gained wide applications.

Transmission measurement based indirect method:

The transmission measurement based method is relatively simple but provides satisfactory X-ray spectrum measuring results [18, 53, 54]. This method is generally performed in two steps. First, transmission data from a phantom with known dimensions and compositions (e.g. Al phantom in a step-wedge shape) is acquired. Second, the X-ray spectrum is reconstructed through solving the linear equations representing the attenuation processes of X-ray photons through the phantom. The mathematical model for describing the transmission measurement process is presented in Eq. (7), where p is the transmission ratio between the transmitted (I) and incident (I_0) photon intensities; E represents the photon energy, and E_{max} and E_{min} are the maximum and minimum photon energy; the detector response $D(E)$ and the X-ray source spectrum $s(E)$ constitute the overall spectrum $W(E)$; the linear attenuation coefficient under energy E and the total path are donated as $\mu(E,r)$ and L [18].

$$\begin{aligned} p = \frac{I}{I_0} &= \int_{E\,min}^{E\,max} D(E)s(E)\,exp[-\int_L \mu(E,r)dl]dE \\ &= \int_{E\,min}^{E\,max} W(E)\,exp[-\int_L \mu(E,r)dl]dE \end{aligned} \tag{7}$$

Eq. (7) can be converted into a linear system, as shown in Eq. (8), where M , N , A and w_i are the total number of measurements, the number of samplings for the spectrum, the measurement matrix derived from $\mu(E,r)$ and L , and the spectrum sampling, respectively. In order to solve the linear problem, various methods have been proposed such as expectation maximization method.

$$p_j = \sum_{i=1}^{N} A_{i,j} w_i , \quad j = 1,2,\ldots,M ,$$
$$A_{i,j} = exp[-\int_L \mu_j (E_i , r) dl] \tag{8}$$

Compton scattering based indirect method:

The Compton scattering based indirect method for X-ray spectrum measurement is another alternative to overcome the pile-up effect occurred in the direct method. This indirect method first acquires the Compton scattered photons from a scattering object using an energy resolved detector (spectrometer) at 90° with respect to the primary X-ray beam. Then, the primary spectrum from the X-ray tube can be extracted through applying an energy correction and the Klein-Nishina formula.

Klein-Nishina formula, as described in Eq. (9), is the differential cross section ($\frac{d\delta_{KN}}{d\Omega}$) of a photon with energy of E scattering into a given angle (θ) [55-57].

$$\frac{d\delta_{KN}}{d\Omega}(E,\theta) = \alpha^2 \gamma_C^2 P(F,\theta)^2 \left[P(E,\theta) + P(E,\theta)^{-1} - 1 + cos^2 \theta \right] / 2 \tag{9}$$

Where $d\Omega$, α , and γ_c are an infinitesimal solid angle element, the fine structure constant, and the reduced Compton wave length of the electron, respectively.

$$P(E,\theta) = \frac{E_c}{E} = \frac{1}{1 + (E / m_e c^2)(1 - cos\,\theta)} \tag{10}$$

$P(E,\theta)$, the ratio of photon energy after and before the Compton scattering, is defined in Eq. (10), where E_c , c , and m_e are the photon energy after the Compton scattering, the speed of light, and the electron mass, respectively [22].

Compton scattering based indirect method can be applied to determine the X-ray spectrum in the energy range from 26keV up to 30MeV, during which the Compton scattering is the predominant interaction of X-ray photons with matter. In order to apply this method for X-ray spectrum measurement with lower energy range such as for mammography, both of Rayleigh scattering and Compton scattering should be carefully considered, because Rayleigh scattering mainly occurs within the energy range of 15-30keV [58].

Computer simulation based indirect method:

In this indirect method, the X-ray spectrum is estimated through simulating the physical parameters such as the kinetic energy of the incident electrons, the physical properties (density, linear attenuation coefficient, and thickness) of the target material, the target angle, and other output settings (internal and additional filtrations, and collimators), based on empirical or semi-empirical physical models. In the past decades, several important simulation codes have been developed and well recognized, such as xcomp5r, Srs-78, TASMIP, Specgen T, Specgen B and xraytbc [19]. It is noteworthy that all the computer simulation methods should be carefully validated by experimental results before their full applications [59].

2.2.4 X-ray spectral measurement using a CdTe spectrometer

Given all the considerations such as superb energy resolution, high quantum efficiency and convenient operation, a semiconductor-based spectrometer using CdTe material is employed in this dissertation for X-ray spectral measurements in XRF and micro-CT imaging systems. The utilized spectrometer system (X-123CdTe, Amptek Inc., Bedford, US) has an energy resolution of 1.2keV at 122keV and an optimum energy range from 5keV to 150keV with 1mm thickness of CdTe. Due to the fact that the CdTe detector is mounted on a thermoelectric cooler, this spectrometer can be operated in a temperature range from -20 to +50 °C.

In order to achieve an accurate X-ray spectral measurement, a precise alignment between the radiation source (X-ray tube) and the spectrometer is of significant importance and usually achieved with the aid of lasers, pinhole collimators and other optical components [20, 60, 61]. Through slightly and gradually adjusting the spectrometer height and angle relative to the X-ray primary beam, a “sweet spot” with the highest photon rate and proper distribution of the X-ray photons in the resultant spectrum can be determined.

Also, as aforementioned, the incident count rate should be carefully restricted within a certain range to avoid the pile-up effects while to maintain sufficient counting statistics. There are basically three important strategies used to adjust the incident count rate. The first way is to change the distance between the X-ray focal spot and the spectrometer. According to the inverse-square law, the further is the spectrometer placed away from the X-ray focal spot, the lower is the recorded incident count rate. The second way is to cover the sensitive area of the spectrometer, which is $25mm^2$ for X-123CdTe, with a set of pinhole collimators. Smaller pinhole collimator can significantly reduce the incident count rate, but increases the difficulty of achieving a precise alignment. The third way, the simplest one among all of the three without moving the spectrometer or changing the collimator sizes is to regulate the incident count rate by selecting different X-ray current settings. Note that the applied X-ray tube voltages and additional filtrations would also significantly influence the incident count rate, but they alter the output spectral characteristic as well, as demonstrated in Fig. 6 and 8, so that they are not the ideal approaches to achieve a desired count rate.

Since that the fluorescence X-rays are generated in a relatively low rate especially when imaging the NPs with trace concentrations and that the spectrometer is generally placed perpendicular with respect to the primary X-ray beam, it is not challenging to reduce the incident count rate in XRF imaging, even with high X-ray tube currents applied and small distance between the NPs and the spectrometer [62]. A pinhole collimator is still employed not only to limit the fluorescence X-rays, but essentially to achieve a necessary spatial resolution. The details can be found in Chapter 3 when describing a theoretical model of a K-shell XRF imaging prototype.

X-ray spectral measurement in a rotating gantry based micro-CT system poses a great challenge due to the extremely limited space inside the gantry. Regular alignment methods and photon count reduction strategies specifically proposed for general X-ray imaging systems being operated in open space cannot be directly applicable or completely transferrable to this specific imaging scenario. Therefore, dedicated efforts are required to perform accurate X-ray spectral alignment and measurement, and to achieve appropriate incident count rate in a micro-CT system. The alignment and measurement method assisted by 3D printing technology will be given in details in Chapter 8.

2.2.5 X-ray spectral analysis and optimization

The X-ray or gamma ray photons are recorded through their interactions with CdTe materials. Instead of directly indicating the energy or generated pulse height for each detected photon, the spectrometer assigns the photons into different channels associated with photon energies utilizing a MCA. A linear energy calibration of converting channel number to photon energy, therefore, is necessary to acquire the X-ray or gamma ray spectrum. For this end, at least two pairs of corresponding energy value and channel number are required to establish the energy calibration mentioned above. The calibration can be expressed as in Eq. (11), where E is the photon energy, C is the corresponding channel number, and A, B are two calibration coefficients.

$$E = A + B \times C \tag{11}$$

Though the calibration accuracy could be further improved if more energy-to-channel pairs are selected, the energy calibration performed in this dissertation only uses two pairs in either primary X-ray spectrum or fluorescence spectrum [63]. Specifically, in primary X-ray spectrum, two pairs are determined by the characteristic peaks from the anode of the X-ray tube such as K_α of 59.32keV and K_β of 67.24keV for tungsten (W), as shown in Fig. 18.

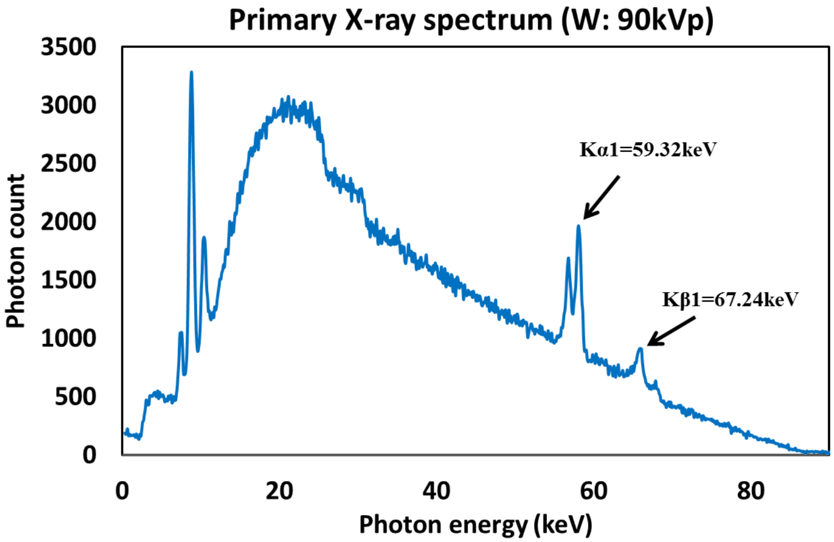

Figure 18. X-ray spectrum from the primary X-ray beam acquired under 90kVp and tungsten (W) target; two typically used characteristic peaks from W for energy calibration are indicated; the original spectral data are collected into 1024 channels.

On the other hand, the pairs used for energy calibration in fluorescence spectrum are selected from gold fluorescence peaks: $K_{\alpha 2}$ energy peak of 66.99keV and $K_{\alpha 1}$ energy peak of 68.80keV, using 100% pure GNPs or GNP solution with very high concentration (mass percentage). Note that the energy peaks selected in the gold fluorescence spectrum can also be other fluorescence peaks, as will be listed in Table. 2 in Section 2.3.3, purposely depending on the utilized fluorescence peaks for XRF imaging. A typical spectrum acquired from gold fluorescence X-rays is shown in Fig. 19.

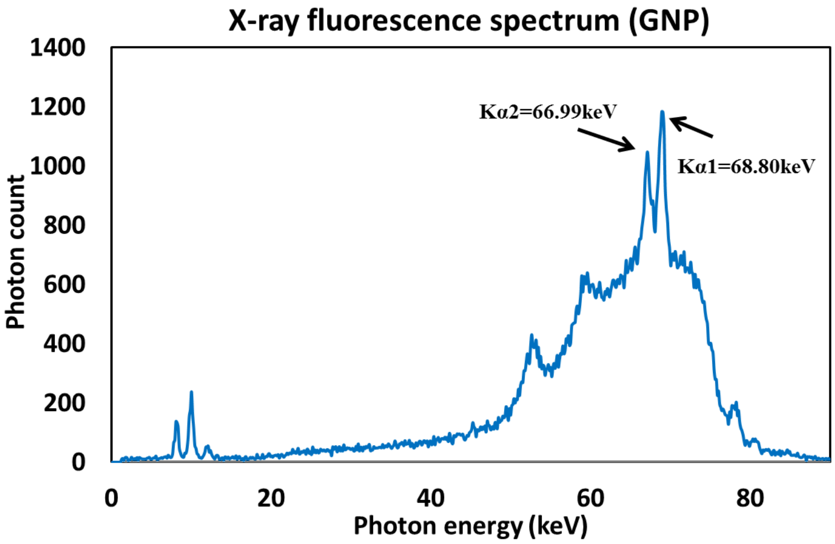

Figure 19. X-ray fluorescence spectrum from 1% mass percentage GNP solution; two typically used characteristic peaks from gold for energy calibration are indicated; the original spectral data are collected into 1024 channels.

As mentioned earlier in this Chapter, both spectra in Fig. 18 and 19 can be regarded as several characteristic peaks atop a continuous background which is formed by either bremsstrahlung process from the anode or Compton scattering of the primary X-ray beam from water/phantom. In order to determine the energy resolution using these characteristic peaks, the continuous background needs to be estimated and removed.

In the X-ray spectrum acquired from the primary X-ray, the continuous background of bremsstrahlung can be acquired through performing a linear fitting using the X-ray photons located at both sides of the characteristic peaks under investigation. In contrast, the background from X-ray scattering of water in the fluorescence spectrum can be determined by the excitation of a water solution under an identical condition as of the high concentration GNP solution. Several numerical methods are also under investigation, as compared to the experimental method, to reduce the second exposure, and will be discussed in Chapter 4. After fitting the separated characteristic peak with a Gaussian function, the corresponding energy resolution can be calculated according to Fig. 20 and Eq. (12), where R is the energy resolution of the characteristic peak, ΔE_{FWHM} is the full width in energy unit at half-maximum (FWHM), and E_C is the central energy of the characteristic peak [22, 64].

$$R = \frac{\Delta E_{FWHM}}{E_C} \times 100\% \tag{12}$$

Fig. 20 depicts the characteristic peaks separated from the X-ray spectrum shown in Fig. 18. After fitting with different Gaussian functions, the FWHMs are calculated as 0.75keV and 1.18keV in this example. Accordingly, the energy resolutions are determined as 1.26% and 1.75% for K_α of 59.32keV and K_β of 67.24keV. Similar background estimation and removal approach can be also applied to the XRF spectrum of GNPs, and the energy resolutions can be determined accordingly. In addition, the fluorescence peak separation in XRF spectrum is vital for the quantitative analysis in XRF imaging because only the X-ray photons under the fluorescence peaks correspond to the stimulated GNPs.

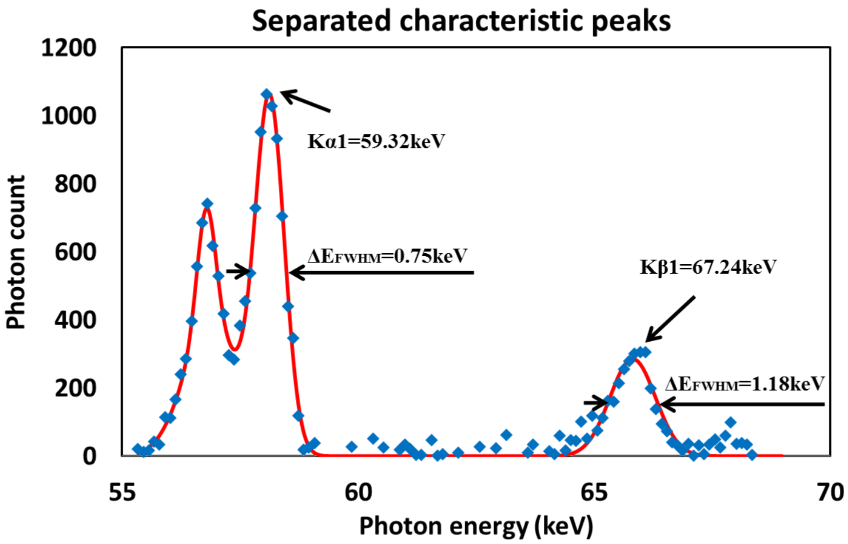

Figure 20. Characteristic peaks after background (bremsstrahlung) removal; the energy resolutions are 1.26% at around 60keV and 1.75% at around 67keV.

The net number of fluorescence X-ray counts (S_k) is calculated through subtracting the background (B_k) from the total counts (G_k), as shown in Eq. (13), where k indicates the fluorescence peak of interest (e.g. $K_{\alpha 2}$ and $K_{\alpha 1}$ of gold fluorescence utilized in this dissertation). Also, measuring uncertainty (U_k) and signal-to-background ratio (SBR_k) of these fluorescence peaks within defined energy window for each fluorescence peak k can be computed using Eq. (14) and (15) [65]. The determination of the optimal energy window will be discussed in details in Chapter 4.

$$S_k = G_k - B_k \tag{13}$$

$$U_k = \sqrt{G_k + B_k} \tag{14}$$

$$SBR_k = S_k / B_k \tag{15}$$

Another important evaluation factor of the acquired spectrum is the mean energy, which along with the half value layer (HVL) evaluates the beam quality generally defined as the overall ability of an X-ray beam to penetrate an object [66].

The mean energy can be directly calculated from the measured spectra using Eq. (16), where ME is the mean energy, E is the energy for each channel, and $N(E)$ is the photon count number in the channel with energy E.

$$ME = \frac{\sum_{E=0keV}^{max\,keV} E \cdot N(E)}{\sum_{E=0keV}^{max\,keV} N(E)} \tag{16}$$

The X-ray spectrum (quality and quantity) can be changed and optimized through applying appropriate internal and additional filtrations. Common materials utilized for X-ray beam filtration include molybdenum (Mo, Z=42), rhodium (Rh, Z=45), silver (Ag, Z=47), aluminum (Al, Z=13), copper (Cu, Z=29), lead (Pb, Z=82) and tin (Sn, Z=50), depending on the specific spectral requirements of imaging modalities. Mo, Rh and Ag, whose K-shell binding energies are between 20 and 27keV, are typically selected in mammography to remove lowest and highest energy X-rays and to keep desired X-ray energies. The X-rays with too low or too high energies have less contributions to imaging performance, but either delivers more radiation dose or reduce the imaging contrast [22]. In CT or micro-CT imaging, on the other hand, Al and Cu are preferred to be employed as either inherent or additional filters. Specifically, the influence of additional spectral filtrations on micro-CT imaging will be comprehensively investigated in Chapter 9.

The selection of spectral filtrations in XRF imaging is essentially dependent on the imaged NPs [67-70]. As described earlier in this chapter, only the portion in the output X-ray spectrum with energy above the electron binding energy is useful to stimulate the fluorescence X-rays. In this dissertation, since the K-shell fluorescence X-rays from GNPs are preferably acquired considering their stronger penetrability at around 70keV, the excitation X-rays with energies below gold's K-edge binding energy (80.729keV) should be removed as much as possible. A piece of Pb or Sn or their combination with Al or Cu is generally adopted for this purpose, an example of using 1mm Pb being shown in Fig. 21 where the X-rays with lower energy and higher energy above the K-edge energy of Pb (~87keV) are notably eliminated and the percentage of useful portion in the whole excitation spectrum is significantly increased [21]. More details regarding the impact of using additional filtration on shaping the excitation spectrum will be shown in Chapter 3 - 7.

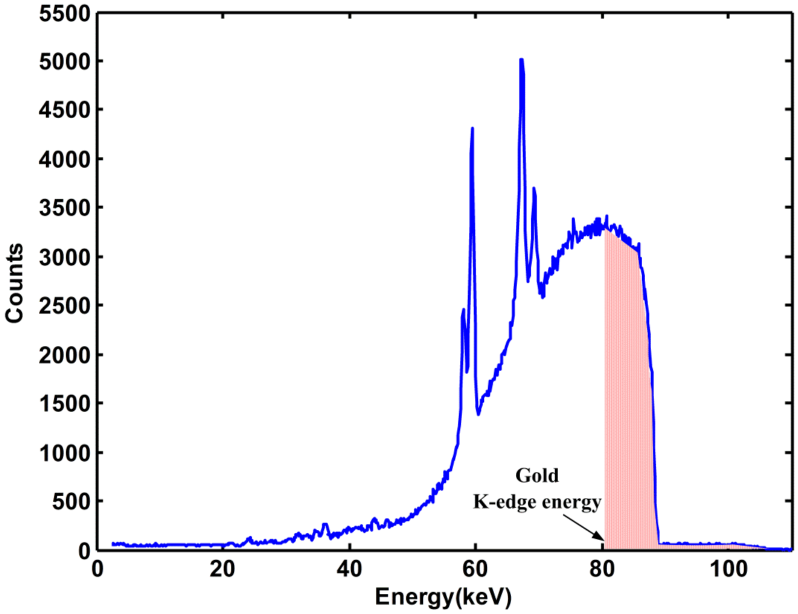

Figure 21. Excitation X-ray spectrum after filtering by a 1mm Pb filter; the useful portion for exciting GNPs to emit K-shell fluorescence photons are increased and highlighted (image from [21]).

2.3 X-ray fluorescence (XRF) and XRF imaging for cancer detection

2.3.1 X-ray fluorescence (XRF)

As discussed in photoelectric absorption, once the energy of the incident X-ray photon exceeds the atomic binding energy in the sample, a vacancy is created after the ejection of the electron in the inner shell and is then filled by a second electron from one of the outer shells. The energy difference between these two shells is released as either fluorescent X-rays or Auger electron emission. Particularly, the emission of fluorescent X-rays are characteristics for different materials (atoms) and the emission intensity is associated with the concentration of the elements under analysis. This process, termed as XRF, has formed the basis for quantitatively spectroscopic analysis [71].

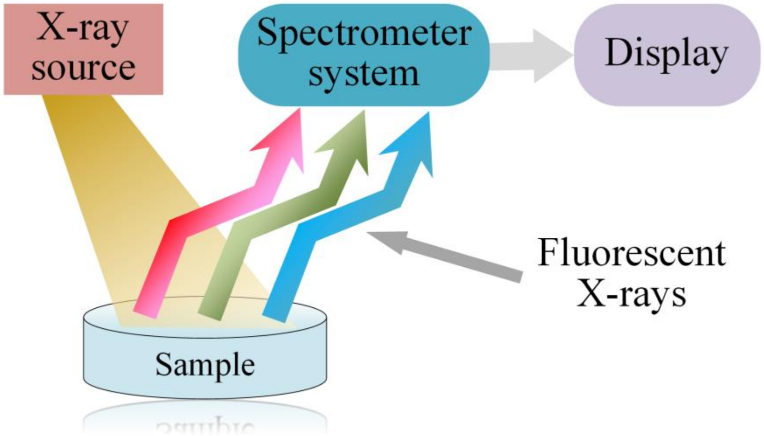

Figure 22. Simplified XRF detection configuration including X-ray source, sample, spectrometer system, and display device.

A simplified XRF detection configuration is shown in Fig. 22, where the X-ray source can be conventional X-ray tubes, synchrotron facilities, or radioactive isotopes, the spectrometer system is to acquire and process the emitted fluorescence X-ray photons, and a computer is used for spectrum display and analysis.

An example of XRF spectra from pure lead, zinc and copper is presented in Fig. 23, where the XRF peaks which are characteristics for different materials are distinguishable [72].

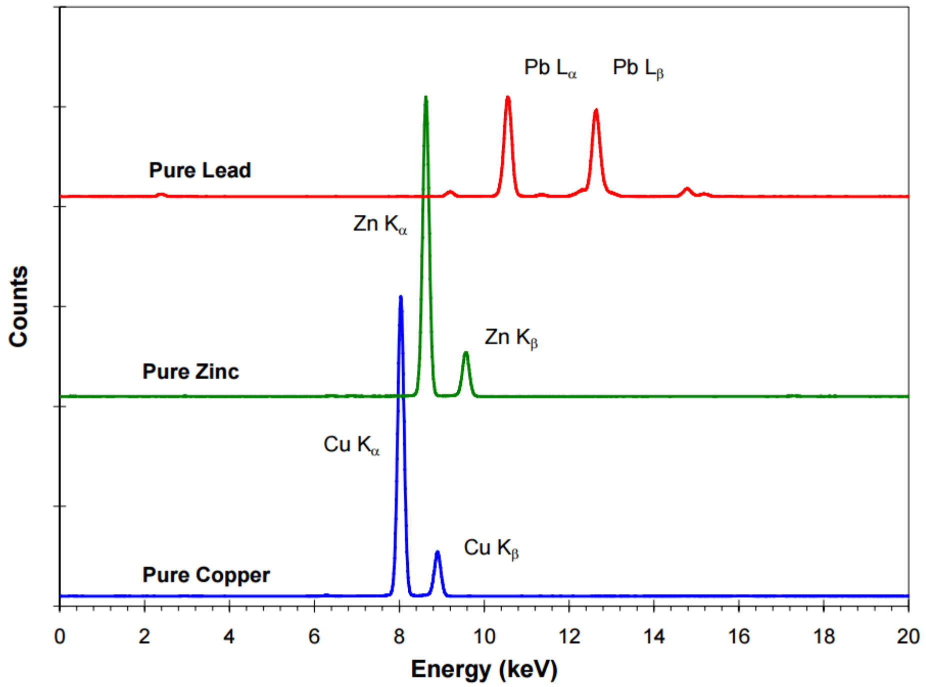

Figure 23. An example of XRF spectra from pure lead, zinc and copper.

A primary competing process of XRF is called Auger electron emission, which usually predominates in low Z elements. In this situation, the released energy from the electron transition process from an outer shell to the inner shell is transferred to another orbital electron rather than being emanated in the form of fluorescent X-ray.

2.3.2 Photoelectric emission analysis

As described in the interactions of X-ray photons with matter, the incident X-rays can be either scattered by Rayleigh scattering and Compton scattering or absorbed by photoelectric effect. Photoelectric absorption results in emission of either fluorescent X-rays or Auger electrons. In order to perform XRF spectroscopic analysis and optimize the XRF detection system, it is important to analyze and quantify the probabilities of generating fluorescent X-rays. For this purpose, K_α fluorescence emission is used as an example and three related probabilities are analyzed.

K-shell electron ejection rather than other shell electrons: the probability of ejecting an electron on K-shell rather than other shells is described by *K-shell absorption jump factor* (J_K) determined in Eq. (17), where R_K is the *K-shell absorption jump ratio* equal to the ratio between the maximum (μ_{max}) and minimum (μ_{min}) mass absorption coefficients at the K absorption edge [73-76].

$$J_K = \frac{R_K - 1}{R_K} = \frac{(\mu_{max} / \mu_{min}) - 1}{(\mu_{max} / \mu_{min})} = \frac{\mu_{max} - \mu_{min}}{\mu_{max}} \tag{17}$$

Both of J_K and R_K are provided in [35] for K shell fluorescence Z=5~101, while L shell fluorescence Z=12~101. Selected J_K and R_K values form Z=5, 10…, 90 are demonstrated in Fig. 24.

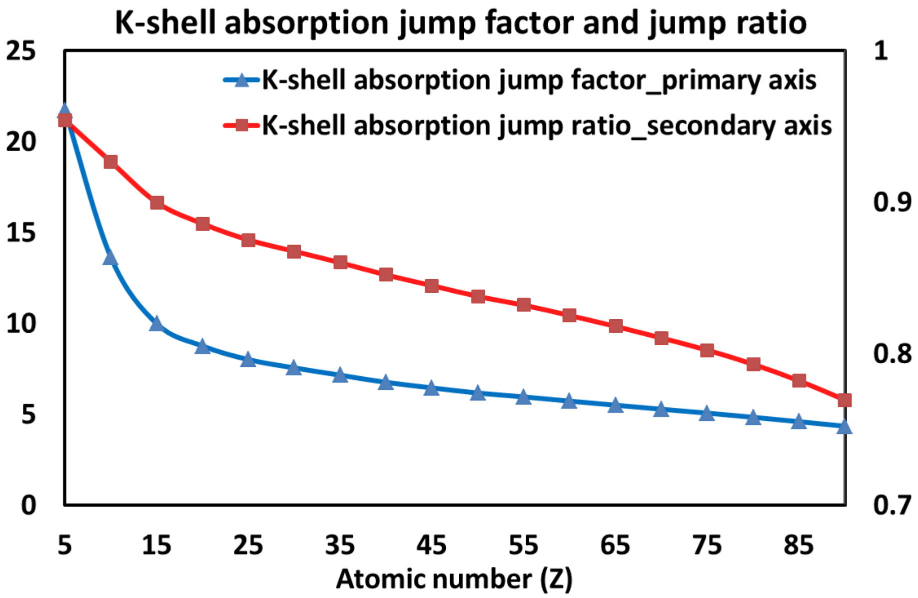

Figure 24. Selected K-shell absorption jump factor and jump ratio for Z=5~90.

A great deal of theoretical and experimental studies have also been conducted to determine J_K and R_K. Poehn et al. developed a method summarized in Eq. (18) to calculate R_K for Z=11~83, where *a*, *b*, *c* and *d* are the fitting parameters [77]. Another equation was proposed by Broll to determine J_K directly for Z=11~70 by the simple linear relationship in Eq. (19) [78].

$$R_K = a + bZ + cZ^2 + dZ^3 \tag{18}$$

$$J_K = 0.915 - 0.0014Z \tag{19}$$

A few of experimental measurements are also used to determine J_K and R_K. Typical methods include gamma ray attenuation method, Compton attenuation method, energy dispersive X-ray fluorescence method, and bremsstrahlung method [74].

Fluorescence emission from K_α compared to from other K lines (K_β): this probability is generally represented by the intensity ratio between K_α and K_β, $I_{K\alpha}/I_{K\beta}$, which can be determined by Eq. (20) [74, 76].

$$\frac{I_{K\alpha}}{I_{K\beta}} = \frac{N_{K\alpha}}{N_{K\beta}} \frac{\beta_{K\alpha}}{\beta_{K\beta}} \frac{\varepsilon_{K\alpha}}{\varepsilon_{K\beta}} \tag{20}$$

Where $N_{K\alpha}$ and $N_{K\beta}$ are the total photon numbers under the peaks, $\beta_{K\alpha}$ and $\beta_{K\beta}$ represent the object's self-absorption difference inside the object, and $\varepsilon_{K\alpha}$ and $\varepsilon_{K\beta}$ are detector efficiencies, for K_α and K_β fluorescence X-rays, respectively.

Fluorescence radiation of K_α rather than an Auger electron: Auger electron emission affects the fluorescent yield, which is defined as the probability that the transition energy is released as fluorescent X-rays. With the increase of the Z number, the fluorescent yields for both K-shell and L-shell XRF emissions are also increased, as shown in Fig. 25, where the L-curve represents the average of three L subshells [35, 73].

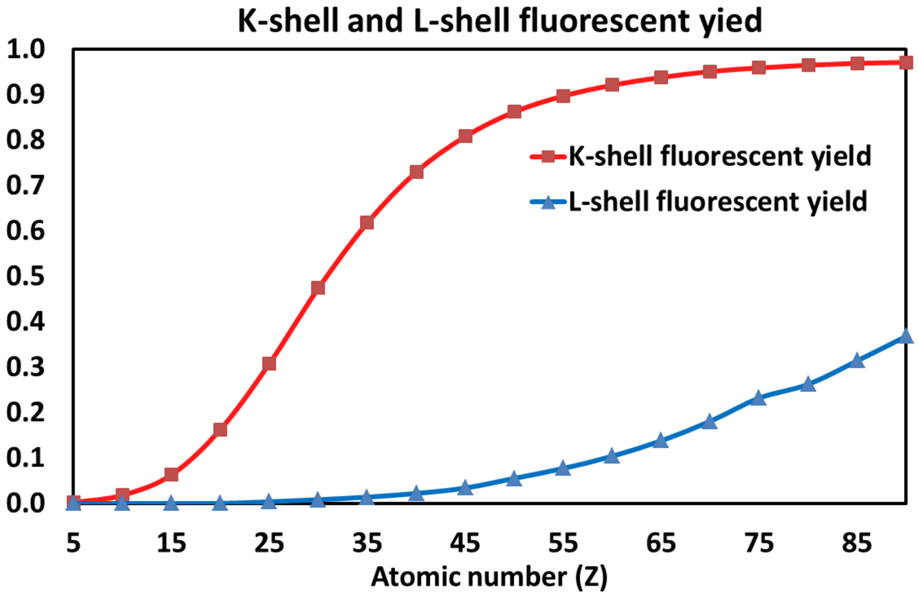

Figure 25. Fluorescent yields for K-shell and L-shell XRF emissions with Z.

2.3.3 EPR effect and XRF imaging for cancer detection

The phenomenon of enhanced permeability and retention (EPR) effect was firstly reported by Matsumura Y and Maeda H in 1986 [79]. During the process of rapid tumor growth, enhanced permeability is observed in the vasculature of tumor tissue than in normal tissue due to the deregulated angiogenesis and the increasingly expressed and activated vascular permeability factors/vascular endothelial cell growth factors (VPFs/VEGFs). As a result, the tumor vascular becomes irregular in microscopic anatomical architecture and consequently, discontinuous endothelial layer with fenestrations ranging in size from 300 nm to 4700 nm is formed [80]. Compared with healthy blood vessels with intact tight junctions between endothelial cells in normal tissue, the leaky tumor vasculature with large fenestrations allows the transvascular extravasation and accumulation of molecules such as liposomes, macromolecules and NPs within the tumor tissue, as shown in Fig. 26 [81]. Furthermore, the residence of molecules in the interstitial fluid among tumor cells could be prolonged as compared with normal tissue due to the ineffective lymphatic drainage mainly caused by lymphatic vessel compression and dysfunctional lymph angiogenesis [82].

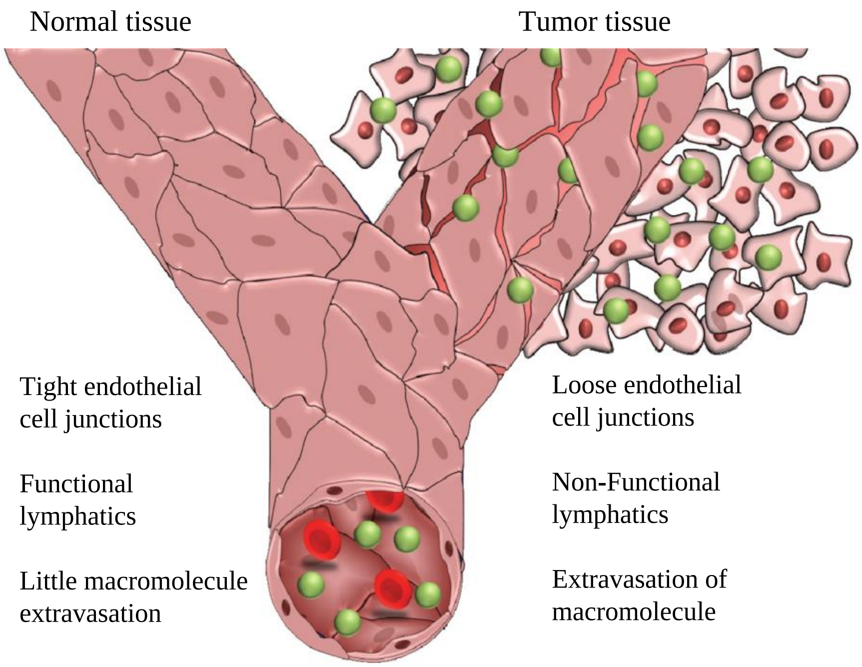

Figure 26. Enhanced permeability and retention (EPR) effect resulted from loose endothelial junctions and nonfunctional lymphatics, resulting in prolonged retention of molecules within the pathological tissue (Image modified from [81]).

Despite the ability of exploiting EPR effect to passively target the tumors with molecules, the targeting efficiency is relatively limited by the lack of tumor specificity [83]. Therefore, a growing research interest has been focusing on further improving the tumor targeting efficiency with increased tumor specificity through so-called active targeting, where the molecules, especially the NPs are conjugated to antibodies and other proteins directed against specific tumors or angiogenesis markers [81, 84, 85].

In recent years, NPs made of high Z element such as iodine (I, Z=53), gadolinium (Gd, Z=64), barium (Ba, Z=56), platinum (Pt, Z=78) and gold (Au, Z=79) in various shapes and forms have been playing an important role in cancer treatment (e.g. anticancer drug delivery and radiation dose enhancement) through either passive or active targeting strategies based on EPR effect [86-90]. Meanwhile it is noteworthy that these NPs can be also functioned as specific imaging probes of tumor tissues owing to their unique physical responses, including the light absorbance and surface plasmon resonance in near-infrared light and the interaction with ionizing radiation. To this end, a few approaches have been considered and investigated to simultaneously determine the bio-distribution and the amount of the NPs within tumor tissue, in an effort to acquire the information of tumors attached by the NPs. Among these approaches, XRF is a promising technique with sufficient specificity and sensitivity for identifying and quantifying these NPs, as discussed in the previous section.

The K- and L-edge absorption and emission energies of the most commonly used NPs (I, Ba, Gd, Pt and Au) are summarized in Table. 2. The emitted fluorescence X-rays with characteristic energies are used to distinguish these NPs, as discussed in last section. Also, the feasibility of performing a quantitative analysis has been demonstrated that the emitted XRF output is linearly proportional to the concentrations of NPs within the imaged objects after performing attenuation correction [68].

Based on the unique characteristic of XRF technique, a primary XRF-based imaging system, X-ray fluorescence computed tomography (XFCT), has been proposed and developed to simultaneously determine the spatial distribution and quantification of the accumulated NPs within the objects [21, 57, 68, 70]. XFCT imaging system combines XRF technique with tomographic imaging. It has been under investigation since the late 1980s when the synchrotron facilities were initially utilized [41]. XFCT imaging is commonly performed in a first-generation CT geometry, acquiring a single line integral at a time, as shown in Fig. 27 [69]. XRF photons are emitted from a selected line (NPs present) within the object when it is illuminated and excited by an incident X-ray pencil-beam, and then these XRF photons are collected by a spectrometer positioned at 90° with respect to the incident beam. A second line integral is acquired after the imaged object being rotated by a small angular increment (e.g. 6° or 12°). The acquisition process continues until a full scan covering 180° or 360° of the object is completed. Subsequently, the full scan is repeated after the translation of the incident pencil-beam or the object in a small step. Using this rotation/translation scanning method, the whole object could be covered, based on which the acquired data is used for post processing and image reconstruction [68, 70].

Table 2. K- and L-edge absorption and emission energies of NPs

Element (Symbol: Z)		**Iodine (I: 53)**	**Barium (Ba: 56)**	**Gadolinium (Gd: 64)**	**Platinum (Pt: 78)**	**Gold (Au: 79)**
K- and L-edge absorption energies (keV)	K_{ab}	33.164	37.410	50.229	78.379	80.713
	L_{Iab}	5.190	5.995	8.393	13.873	14.353
	L_{IIab}	4.856	5.623	7.940	13.268	13.733
	L_{IIIab}	4.559	5.247	7.252	11.559	11.919
Emission energies from XRF (keV)	$K_{\beta 2}$	33.016	37.255	49.961	77.866	80.165
	$K_{\beta 1}$	32.292	36.376	48.718	75.736	77.968
	$K_{\alpha 2}$	28.610	32.191	42.983	66.820	68.794
	$K_{\alpha 1}$	28.315	31.815	42.280	65.111	66.980
	$L_{\gamma 1}$	4.800	5.531	7.788	12.939	13.379
	$L_{\beta 2}$	4.507	5.156	7.102	11.249	11.582
	$L_{\beta 1}$	4.220	4.828	6.714	11.069	11.439
	$L_{\alpha 2}$	3.937	4.467	6.059	9.441	9.711
	$L_{\alpha 1}$	3.926	4.451	6.027	9.360	9.625

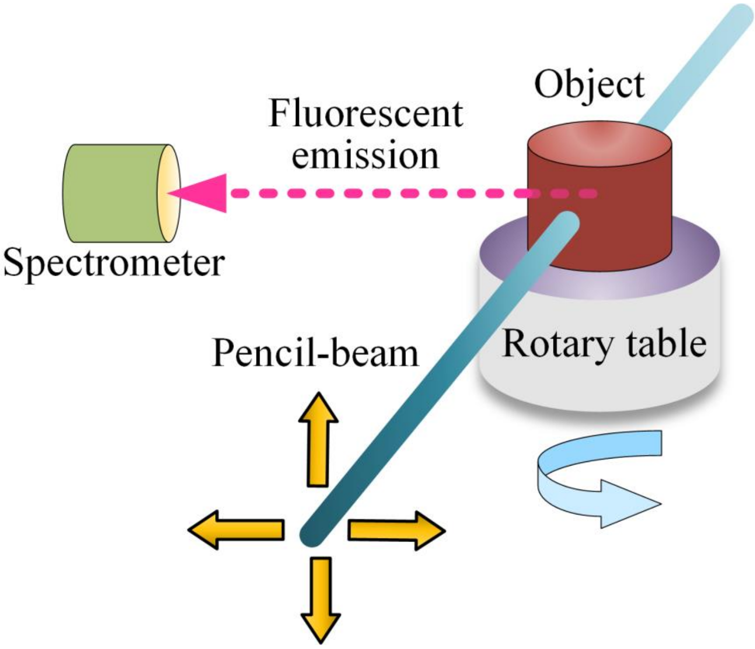

Figure 27. Schematic of the rotation/translation scanning method in the first-generation CT geometry. XRF photons that are stimulated by the incident X-ray pencil-beam are detected by a spectrometer.

Though the availability of monochromatic X-rays from synchrotron source maximizes the conversion efficiency from excitation X-ray to fluorescence X-ray, the limited accessibility to synchrotron facilities makes the application of XFCT imaging to clinical diagnosis impractical. Note that in recent years, the feasibility of developing a benchtop XFCT using a conventional X-ray source has been demonstrated, showing a promising potential to apply XFCT in biomedical imaging applications [68, 91, 92]. With a commonly available clinical X-ray source and a single spectrometer, as an example, the tomographic XFCT imaging of an GNP-loaded phantom can be obtained (Fig. 28) [68].

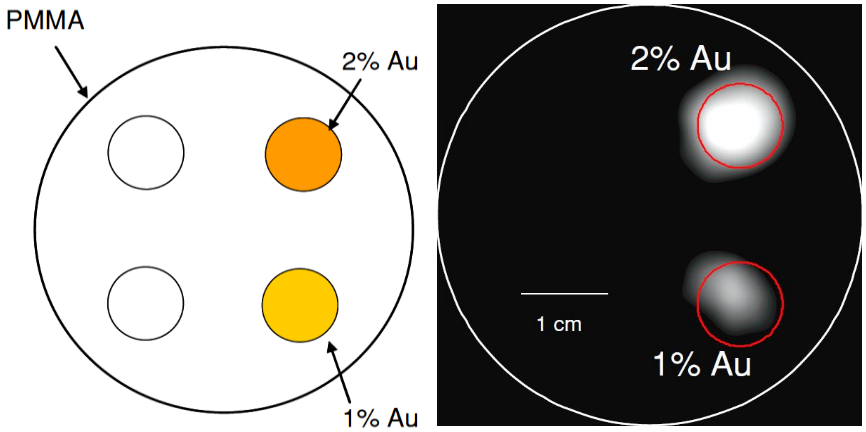

Figure 28. (a) Schematic of a GNP-loaded phantom with 5cm in diameter. Two slots were filled with GNPs at 1% and 2% mass percentage; (b) Reconstructed GNP distribution and location within the phantom (Image from [68]).

Selected studies from year 2010 to present regarding the development and optimization of XFCT imaging system using a conventional polychromatic X-ray source are summarized in Table. 3, presenting important system parameters.

Due to the relatively low fluorescence production efficiency from NPs using a conventional X-ray source, the diameters of the phantom under investigation is usually less than 50mm, as described in Table. 3. It is immediately noticed that the potential biomedical application of currently developed XFCT imaging system is for the imaging of NPs targeted tumor and critical organs within a small animal or *ex vivo* small-sized samples [68, 91, 92]. Also, attempts have been tried to apply XFCT imaging modality to human applications even with quasi-monochromatic X-rays, computational and experimental results showing a limited success in terms of lower achievable spatial resolution, insufficient detectable concentrations and longer scanning time [93].

Table 3. Summary of selected investigations on XFCT imaging system using conventional polychromatic X-ray source (2010 - present).

Type	NP and XRF energy (keV)	Lowest concentration (by weight)	Phantom size (D: mm)	Beam geometry	Detector number	Radiation dose	Total scan time
Experimental study [68]	Au: ~70	0.5%	50	Pencil-beam	Single	2Gy	30 h
Experimental study [92]	Au:~70	0.5%	30	Cone-beam	Double	0.2Gy	~1h
Experimental study [70]	Pt: ~65 Gd: ~45 I: ~30	0.5%	35	Pencil-beam	Single	0.77Gy	~5h
Experimental study [94]	Au: ~70 Gd: ~45 Ba: ~35	2%	35	Pencil-beam	Single	0.77Gy	~5h
Simulation study [91]	Au: ~70	0.1%	50	Cone-beam	Multiple	0.3Gy	~1h
Simulation study [95]	Au: ~70	0.2%	20	Fan- beam	Multiple	90Gy	~5min
Simulation study [96]	Au: ~80	0.005%	22.5	Pencil-beam	Single	0.02Gy	N/A

This dissertation investigates another important XRF based imaging modality, XFM using a conventional X-ray tube. Compared to XFCT utilizing a rotational imaging geometry, XFM employs directly translational imaging geometry to detect and acquire the fluorescence signals, so that it has some specific imaging applications such as breast cancer detection with carefully considered imaging trajectory. Though other detection angles with respect to the primary excitation beam have been studied for different XRF peaks, 90 degree is still the most regularly applied angle in XRF imaging in both XFCT and XFM, and will be employed in this dissertation [96, 97].

2.4 Micro-CT imaging

X-ray CT is one of the most valuable imaging modalities providing non-invasive and 3D imaging capabilities. Nowadays, CT imaging has been heavily performed in clinical applications for both diagnostics and treatment planning, industrial applications and other applications such as in luggage inspection system. As a scaled-down CT imaging modality, micro-CT was initially developed for industrial imaging applications and then for small animal imaging, but it recently has proven to be a useful tool in various clinical medical applications such as the assessments of the 3D bone microstructure and bone mineral density (BMD) performed on human legs or on bone biopsy specimens, the study of microvasculature anatomy, and the imaging of tumor perfusion and angiogenesis [98]. Micro-CT is capable of providing 3D imaging at high resolution on the order up to 10 μm, enhancing the way of non-invasively and precisely visualizing the microarchitecture inside the object [99-104].

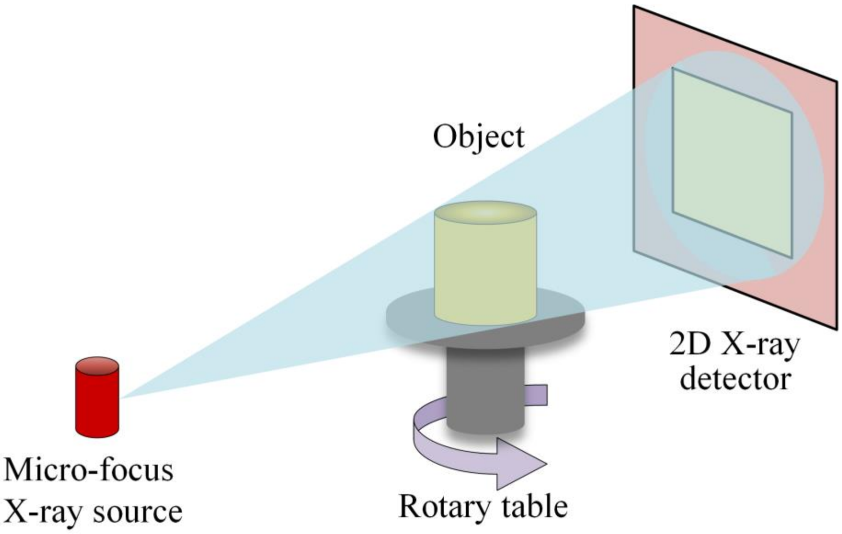

Figure 29. Schematic for a micro-CT including a micro-focus X-ray tube, a rotary table with object, and a 2D X-ray detector.

The working principle of a micro-CT is the same as in a regular CT, as shown in Fig. 29. A typical micro-CT consists of a conventional X-ray tube with a micro-focus spot, a 2D X-ray imaging detector, and a stage for imaged objects placement. During the imaging, either the combination of X-ray tube and detector, or the object is rotated for 180 or 360 degree. During this process, the cone-beam X-ray continuously irradiates the object, and hundreds of 2D projection data are acquired by the 2D X-ray detector. Then, a 3D representation of the object can be acquired from those projection data through applying a reconstruction algorithm.

Characterizing and optimizing the imaging performance of micro-CT have been widely investigated in the past decades with simulation and experimental methods. Primary studies include the determination of the radiation dose levels using Monte Carlo procedure or ion-chamber dosimeter, the assessment of system resolution in slanted edge and plane spread function methods, the investigation of noise propagation and reduction, and other evaluations for imaging quality assurance such as geometric accuracy, linearity, CT number variation, as well as uniformity [10, 105-107]. Inherent and additional filtrations are generally applied in micro-CT to eliminate low-energy photons that make less contribution to image quality but tend to increase the absorbed radiation dose [10, 105, 106]. However, their effectiveness and influence on CT number variation, noise level and image quality have not been fully characterized to date. Though the influence of spectral filtration on patient dose as well as image quality has been studied on a conventional CT scanner, the imaging parameters and scenario are different as in a micro-CT system [12]. Therefore, it is necessary and meaningful to perform a comprehensive investigation of the impact of spectral filtrations on image quality in a micro-CT system, the prerequisite of which is an accurate measurement of X-ray spectrum.

However, as stated in Section 2.2.4, regular alignment methods proposed for X-ray spectral measurement in general X-ray imaging systems being operated in open space cannot be directly applicable or transferrable to a rotating gantry based micro-CT system. This type of micro-CT system doesn’t provide the possibility to change the scanner geometry easily, meaning that normally the source-to-detector distance (SDD) is completely fixed and extremely limited when compared to a prototyped micro-CT system [108]. In addition, the X-rays backscattered inside the gantry are not negligible due to the short SDD. Therefore, it is necessary to develop a specific alignment method for the X-ray spectral measurement in rotating gantry based micro-CT systems without introducing additional backscatters.

2.5 Chapter summary

This chapter first introduces X-rays and their properties, applications, and generation methods. Then, several methods for X-ray spectral measurement and analysis are discussed, followed by the theory of XRF technique and the innovation of exploring XRF based imaging modalities (e.g. XFCT) for biomedical applications. Last, this chapter analyzes the significance of spectral impact on micro-CT imaging and the necessity of overcoming the difficulties of spectral measurement and analysis in a rotating gantry based micro-CT imaging system.

Chapter 3: General theoretical model of K-shell XRF of GNPs

3.1 Selection of gold XRF peaks

The basic principle of XRF of NPs has been presented in Chapter 2. As newly approved by food and drug administration (FDA), GNPs can be potential drug carriers, contrast agents, radio-sensitizers and photothermic agents, and have attracted great clinical and research interests [109]. Extensive worldwide research has been conducted due to both of the physical/chemical properties of gold and the specific active/passive targeting strategies according to the tumor specificity of nanoparticles [86, 88].

The XRF mechanism of gold is depicted as below in Fig. 30 (a) and (b) using an electron on the K-shell as an example. There are totally 79 electrons surrounding the nuclear of gold, 2 on the K-shell, 8 on the L-shell, 18 on the M-shell, and so on, and under normal condition, the gold atom consisting of the nuclear and the surrounding electrons is at a stable state. However, when the gold atom is excited by incoming radiation from X-ray or gamma ray with energy higher than the K-edge energy, which is 80.725keV for gold, the electron on the K-shell is ejected out to become a photoelectron, leaving a vacancy on the K-shell and making the atom at an unstable state.

The vacancy is then rapidly filled by a second electron from one of the outer shells, as shown in Fig. 30 (b). During this process, fluorescent X-ray photons with characteristic energies of gold are emitted.

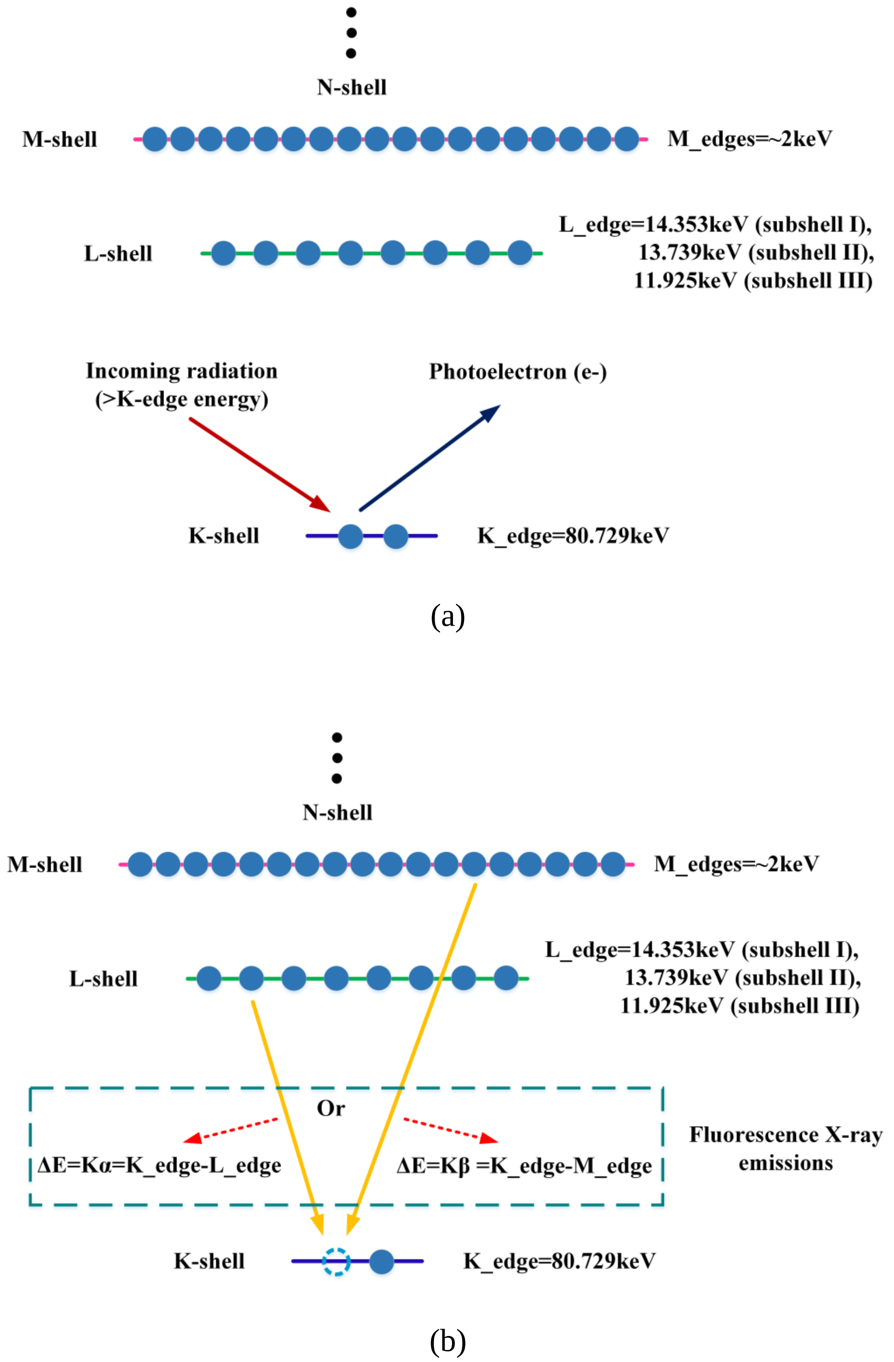

Figure 30. An electron on the K-shell is used to explain the XRF process of a gold atom: (a) the electron on the K-shell is ejected out to become a photoelectron, leaving a vacancy on the K-shell and making the atom at an unstable state, when the gold atom is excited by incoming radiation from X-ray or gamma ray with energy higher than the K-edge energy, which is 80.725keV for gold; (b) the vacancy is rapidly filled by a second electron from one of the outer shells.

In order to select the proper fluorescence peaks of GNPs for imaging, a 1% mass percentage GNP solution (the preparation of GNP solutions will be introduced in Chapter 4) is excited under 110kVp voltage setting of a polychromatic X-ray tube (W) without any blockages except two air gaps on both excitation and emission paths (the imaging configuration of XRF will be introduced in Section 3.3). The XRF spectrum detected at a 90° with respect to the excitation path, as shown in Fig. 31, indicates that nine available peaks are clearly observed at various energies, of which seven peaks come from the fluorescence X-rays of GNPs: L_α at 9.71keV, L_β at 11.44keV, L_γ at 13.38keV, $K_{\alpha 2}$ at 66.99keV, $K_{\alpha 1}$ at 68.80keV, $K_{\beta 1}$ at 77.97keV and $K_{\beta 2}$ at 80.17keV, while the other two from water scattering of the characteristic peaks of W in the incident X-ray spectrum [21].

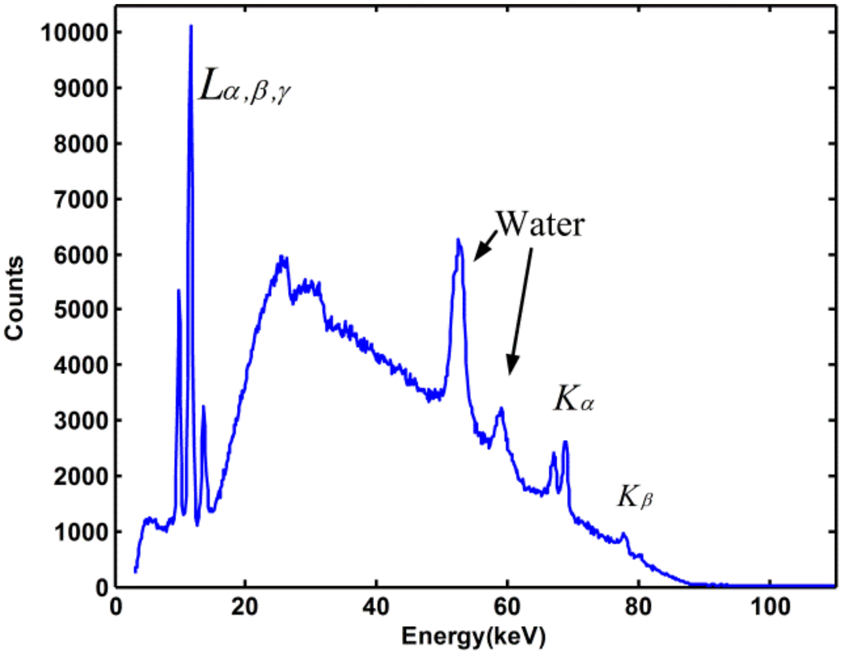

Figure 31. XRF spectrum from a 1% mass percentage GNP solution with no blockages on both paths.

In order to measure the penetrability of fluorescence X-rays from GNPs, a combination of BR12 of 70mm thickness on the excitation path and of 50mm thickness on the emission path is selected. This specific selection will be explained in details when introducing the XFM imaging modality for breast imaging in Chapter 5.

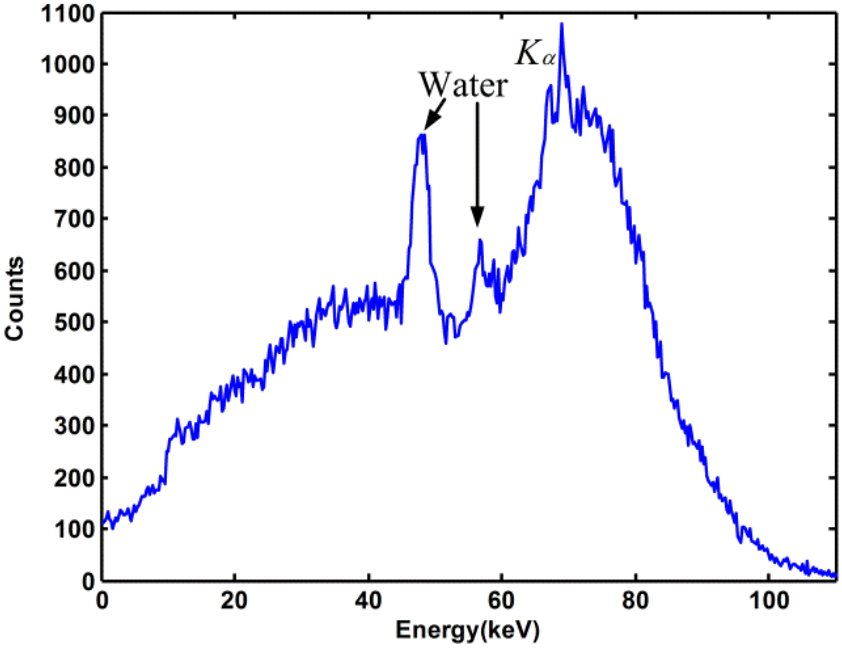

Figure 32. XRF spectra with BR12 blocks on the excitation (70mm)/emission (50mm) path when using 1.0% gold solution.

The comparison of spectra acquired without/with the BR12 (Fig. 31 and 32) demonstrates that the penetrability of fluorescence X-rays from the L-shell peaked at 9.7keV, 11.4keV and 13.38keV are limited due to their very low energy levels and thus high attenuations inside the BR12. Although K_β at 77.97keV and 80.17keV have higher energy levels and therefore low attenuation effects, their fluorescence intensities are quite low. Consequently, all of these fluorescence peaks mentioned above are totally annihilated when passing through certain thickness of the BR12, such as 50mm mentioned above. However, the left $K_{\alpha 2}$ and $K_{\alpha 1}$ at 66.99keV and 68.80keV are still palpable and dominant after travelling such a deep penetration through the 50mm thick BR12. This is because, compared to fluorescence X-rays emitted from L-shell of GNPs, the energy and the penetrability represented by mean free path are about 70keV and 5cm in water for K-shell fluorescence X-rays while are about 11keV and 0.2cm in water for L-shell fluorescence X-rays [22, 68, 88, 110]. Therefore, the fluorescence X-rays acquired from K-shell emission, specifically two K_{α} fluorescence peaks have attracted more and more attentions for XRF imaging and will be preferably utilized and studied in this dissertation.

3.2 A general theoretical model of K-shell XRF imaging using GNPs

In order to establish a theoretical model of K-shell XRF imaging, a standard imaging setup using a pencil-beam of excitation X-rays and a collimated spectrometer detector is described in Fig. 33 [21, 68, 94, 97, 111-113]. The detector is located at $90°$ with respect to the illumination axis, and the excitation volumetric element with a geometric center coordinate of $p(x, \mathrm{y})$ is defined as the intersection of the illumination beam and the field-of-view of the detector collimator [21]. Without loss of generality, the object (BR12 or other tissue mimicking phantom) is selected with arbitrary shape and property, and $p(x, \mathrm{y})$ can be any excitation element within the object. The overall imaging process mainly consists of three parts: (1) the collimation, filtration and attenuation of the incident X-ray beam from intensity of (I_0) to (I_1), (2) the interaction including X-ray fluorescence (if NPs exist) and Compton scattering at $p(x, \mathrm{y})$, and (3) the attenuation, collimation and detection of the emitted fluorescence X-rays (F) as well as the Compton scattered X-rays (CS). This process is discussed and formulated in the following subsections.

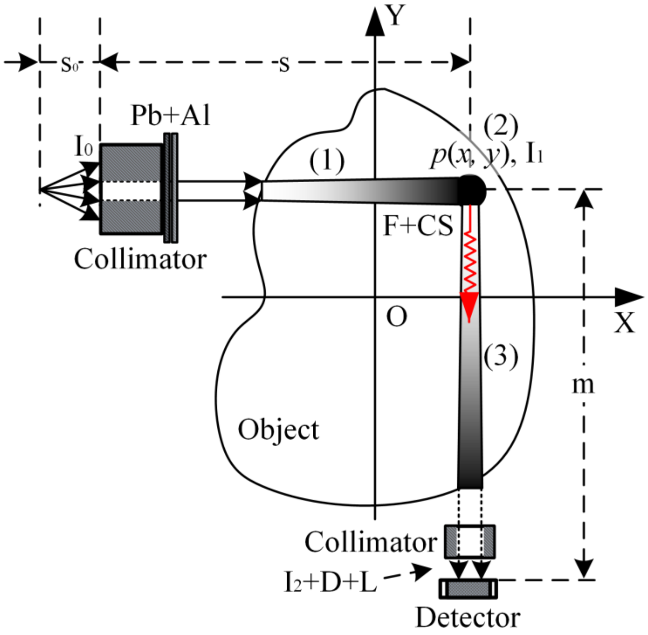

Figure 33. Schematic diagram of a standard XRF imaging setup using a pencil-beam of excitation X-rays and a collimated spectrometer detector.

3.2.1 Modulation of the incident X-ray beam

Before reaching $p(x, \mathrm{y})$, the collimated X-ray pencil-beam I_0 right before the collimator is attenuated by a filter combination of Pb and Al, an air gap, and a part of the object on the excitation path. Taking into consideration of the distance (s) between the collimator and $p(x, \mathrm{y})$ as well as (s_0) from the X-ray focal spot to the collimator, the X-ray intensity (I_1) just arriving at $p(x, \mathrm{y})$ is expressed as in Eq. (21) according to the Beer Lambert law and the inverse square law [114-118]:

$$I_1(E) = I_0(E)\,exp\{-[\mu_{Pb}(E)l_{Pb} + \mu_{Al}(E)l_{Al} + \mu_{air}(E)l_{air} + \int_{-\infty}^{x} \mu_{ex}(E,x')dx')]\}s_0^2 / s^2 \quad (21)$$

Where E is the photon energy, μ_{Pb} , μ_{Al} , μ_{air} and μ_{ex} are the linear attenuation coefficients (LACs) of Pb, Al, air and object, respectively, while l_{Pb} , l_{Al} , l_{air} and $(-\infty, x)$ indicate their corresponding penetration distances. Note that the attenuation effect inside the object is an integral due to its unknown heterogeneity.

3.2.2 X-ray fluorescence excitation

Assuming that there exists GNPs around $p(x, y)$, K-shell fluorescence X-rays are emitted isotropically upon the excitation by impinging X-ray photons with energy higher than the K-edge binding energy of GNPs. The production of F is described in Eq. (22) [114-118]:

$$F = \eta\mu_{ph}[\int_{Ek-edge}^{Emax} I_1(E)dE]MV_e \quad (22)$$

Where η , μ_{ph} , and M are the integrated K_α emission probability considering the K-shell absorption jump factor, the intensity radio of K_α and K_β emission, and the fluorescent yield competing with Auger emission, the photoelectric mass absorption coefficient, and the concentration of NPs; V_e is the excitation element volume.

3.2.3 Compton scattering interaction

Due to the trace amounts of the NPs inside the object, the majority part of I_1 is involved in scattering interaction, specifically Compton scattering which predominates in the diagnostic energy range above 26keV [22]. The differential cross section ($\frac{d\delta_{KN}}{d\Omega}$)

of a photon with energy of E scattering into a given angle (θ) has been described in Eq. (9).

The Compton scattering intensity (CS) is then computed as the product of I_1, n_e and $\frac{d\delta_{KN}}{d\Omega}$, as in Eq. (23), in which n_e is the electron density, N_A is the Avogadro number, and ρ, A, and Z are the density, the atomic weight, and the atomic number of the object within V_e around $p(x, \mathrm{y})$. Eq. (23) could be approximately simplified since the ratio $\frac{Z}{A}$ is close to $\frac{1}{2}$ for most elements [57, 117].

$$\begin{aligned} CS(E_c,\theta)\big|_{E_c=P(E,\theta)E} &= I_1(E)n_e\frac{d\delta_{KN}}{d\Omega}(E,\theta) \\ &= I_1(E)N_A\rho\frac{Z}{A}\frac{d\delta_{KN}}{d\Omega}(E,\theta) \\ &\approx \frac{1}{2}I_1(E)N_A\rho\frac{d\delta_{KN}}{d\Omega}(E,\theta) \end{aligned} \tag{23}$$

3.2.4 Detection of fluorescence and scattered X-rays

Both fluorescence (F) and Compton scattered (CS) X-rays produced by I_1 need to traverse part of the object before they can be detected by the collimated spectrometer. During this process, the detection angle is limited by the detector collimator diameter (A_d) and the distance (m) between the collimator surface and $p(x, \mathrm{y})$. The received intensity (I_2) of fluorescence X-rays is derived in Eq. (24), where $\varepsilon_d(E)$ is the detector efficiency and $s(E)$ is the attenuation term in the emission path considering the attenuation effects of air and heterogeneous object (μ_{em}). E_F indicates the central energy of the emitted K-shell fluorescence X-rays from GNPs [114-118].

$$I_2(x,y;E_F)=F(x,y)\frac{A_d}{4\pi m^2}\frac{1}{m^2}\varepsilon_d(E_F)s(E_F) \tag{24}$$

$$s(E_F)=exp\{-[\mu_{air}(E_F)l'_{air}+\int_{-\infty}^{y}\mu_{em}(E_F,y')dy')]\} \tag{25}$$

Compared to the intensity of K-shell fluorescence X-rays that has characteristic energies, the received intensity (D) of Compton scattered X-rays derived in Eq. (26) covers a wide spectrum, because all the X-ray photons represented by I_1 contribute to Compton scattering process.

$$D(x,y;E_c,\theta)=CS(E_c,\theta)\frac{A_d}{4\pi m^2}\frac{1}{m^2}\varepsilon_d(E_c)s(E_c) \tag{26}$$

$$s(E_c)=exp\{-[\mu_{air}(E_c)l'_{air}+\int_{-\infty}^{y}\mu_{em}(E_c,y')dy')]\} \tag{27}$$

In addition to I_2 and D, another portion (L) that contributes to the final spectrum acquisition (T) mostly consists of the X-ray photons leaking into the spectrometer from other ways such as environmental scattering, as shown in Eq. (28).

$$T=I_2+D+L \tag{28}$$

Though the L portion may be suppressed by wrapping the spectrometer in shielding material like Pb, it may not be completely eliminated. In order to acquire an accurate D, L must be subtracted from the total spectrum. Experimentally, L can be estimated by performing another spectrum acquisition without the object as well as the GNPs under identical exposure conditions.

An example of measured spectrum of 0.5% GNP solution is displayed in Fig. 34, showing the presence of four K-shell fluorescence peaks, especially $K_{\alpha 2}$ and $K_{\alpha 1}$ peaks of interest, which are overlapped with the Compton scattering X-rays. The isolation of the XRF signals requires the knowledge of the background spectrum (scattered X-ray photons) under each of the fluorescence peaks. In this example, the background spectrum is acquired through exciting a water solution contained in the same container as GNP solutions. After subtracting the scattering background ($D+L$) from the total X-ray photons ($T = I_2 + D + L$), the XRF signals (I_2) are obtained. A measurement of L is also displayed in Fig. 34, but note that both of the measured total spectrum and water background are elevated relative to L.

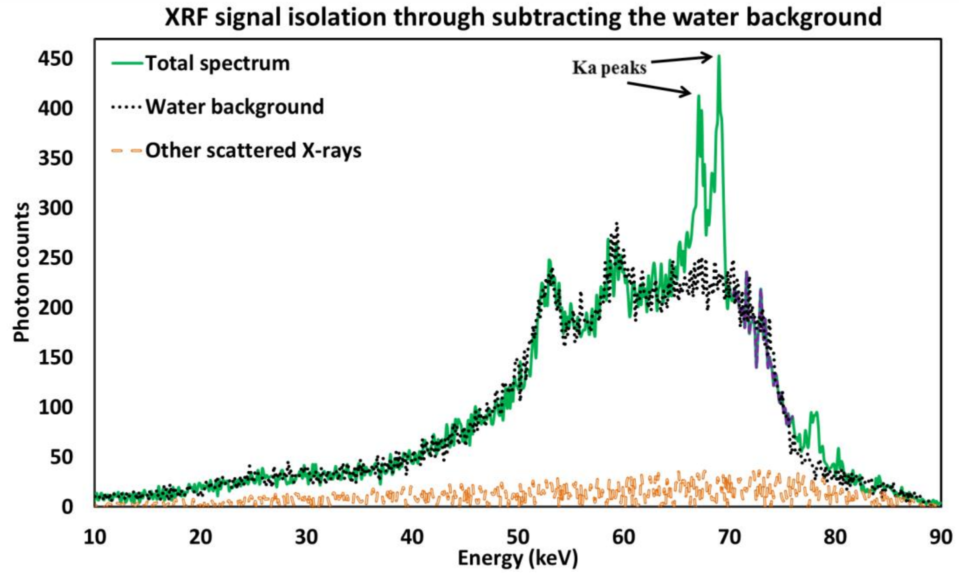

Figure 34. An example of measured spectrum from 0.5% GNP solution.

3.3 Challenges of quantitative analysis of K-shell XRF signals

Substituting Eq. (21), (22) and (25) into Eq. (24), the received intensity of K-shell fluorescence X-ray (I_2) can be written as in Eq. (29), where term A includes all the constants that are known from the literature or can be measured in the imaging modality, and the attenuation effects from the excitation filtrations, term B represents the attenuations in the excitation path inside the object, and term C is regarding the attenuations in the detection path inside the object. It is noted that I_2 is not only related to M , the concentration of the determined GNPs, but also is associated with the position of the excitation volumetric element and the attenuation property of the object, as indicated in terms B and C . The influences from terms B and C need to be eliminated or calibrated before finding a linear relationship between the detected fluorescence X-ray photons and M .

$$\begin{aligned} I_2(x,y;E_F) = & \underbrace{\frac{\eta\mu_{ph}V_e\nu_\alpha A_d\varepsilon_d(E_F)s_0^2}{4\pi m^4 s^2}\int_{E_{k-edge}}^{E_{max}} I_0(E)\,exp\{-[\mu_{Pb}(E)l_{Pb}+\mu_{Al}(E)l_{Al}]\}dE']}_{A} \\ & \underbrace{\times\int_{E_{k-edge}}^{E_{max}} I_0(E')\,exp[-\int_{-\infty}^{x}\mu_{ex}(E',x')dx']dE'}_{B} \\ & \times\underbrace{exp\{-[\int_{-\infty}^{y}\mu_{em}(E_F,y')dy']}_{C} \\ & \times M \end{aligned} \tag{29}$$

If the object’s property is known, μ_{ex} for the energy from $E_{k\text{-}edge}$ to E_{max} and μ_{em} for energy of E_F can be available as *a priori* knowledge, and thus, $I_2(x,y;E_F)$ can be calibrated by multiplying two inverse terms of B and C .

$$\begin{aligned} I_2(x,y;E_F)\,|_{\text{calibrated}} = & \; I_2(x,y;E_F) \\ & \times\int_{E_{k-edge}}^{E_{max}} I_0(E')\,exp[\int_{-\infty}^{x}\mu_{ex}(E',x')dx']dE' \\ & \times exp\{[\int_{-\infty}^{y}\mu_{em}(E_F,y')dy'] \end{aligned} \tag{30}$$

This *a priori* knowledge based method works well especially if the object is homogeneous. For other imaging conditions in K-shell XRF imaging with unknown or heterogeneous property of the imaged object, it can only provide a rough estimate.

3.4 Chapter summary

This chapter first introduces the XRF mechanism of gold atom and why K-shell fluorescence peaks, especially $K_{\alpha 2}$ and $K_{\alpha 1}$, are selected for the investigation in this dissertation. Second, a theoretical model of gold K-shell XRF imaging is established using a generalized imaging geometry including a pencil-beam X-ray of excitation and a single spectrometer. Last, the challenges of finding the linear relationship between the fluorescence signal intensity and the GNP concentration are discussed in the conditions with known/unknown object's property.

Chapter 4: Energy window and background estimation

4.1 Chapter introduction

As described in Chapter 3, though excitation filtrations (Pb and Al), optimal geometry (90 ° between the excitation path and emission path) and pinhole collimators (x-ray pencil beam collimator and spectrometer collimators) are adopted, the acquired XRF signals (fluorescence peaks) are still overlapped with the background mainly caused by Compton and elastically scattered X-rays and fluorescence X-rays from other elements in the object. Accurate extraction of fluorescence signals from the background, therefore, is a critical step for quantitative XRF analysis of GNPs and precise interpretation of physiological and pathological activities in living subjects. Over-estimation or under-estimation of the background would introduce significant errors in quantitative analysis, especially for weak fluorescence signals from low concentration GNPs, thus limiting the precision and detectability [119].

Though the background can be estimated in an experimental way of imaging a water solution under identical imaging conditions, the method itself is not suitable for clinical purpose since it may involve a second exposure (i.e. double radiation dose) to the patient and some practically operational issues (e.g. precise positioning of the patient before and after the injection of GNPs). To this end, lots of mathematical and numerical methods such as trapezoidal shape estimation, polynomial interpolation, and iterative method have been proposed. However, to the best of our knowledge, there is currently no evaluation standard regarding the performance of these methods compared to the experimental data, especially for the quantitative K-shell XRF analysis of GNPs.

Through directly subtracting the background data obtained in the experimental way, this chapter first acquires the fluorescence-only spectra, based on which the optimal energy windows and corresponding neighboring energy bins for $K_{\alpha 1}$ and $K_{\alpha 2}$ gold fluorescence peaks are determined. Then, using the neighboring energy bins for each K-shell fluorescence peak, three types of typically used numerical methods are performed on the original spectra acquired from GNP solutions. Finally, the backgrounds determined using the experimental and the numerical methods are analyzed and compared within the optimal energy windows for K-shell gold fluorescence peaks.

4.2 GNP/water solutions preparation and XRF imaging configuration

4.2.1 Preparation of GNP/water solutions

In order to resemble the possible tumor gold concentrations *in vivo*, commercially available GNPs with 15nm diameter (Aurovist^{TM}, Nanoprobes Inc., NY, US) are used to prepare a series of saline GNP solutions with mass percentage of 2%, 1%, 0.5%, 0.25%, 0.2%, 0.1%, 0.05% and 0.01%, corresponding to 20mg, 10mg, 5mg, 2.5mg, 2mg, 1mg, 0.5mg and 0.1mg GNPs per 1000mg water. During the preparation and dilution processes, GNPs and water are completely mixed through spinning the mixture by a laboratory agitator for several minutes. An additional water solution is also made for acquiring the background data without the fluorescence information of GNPs. Each prepared GNP/water solution is poured into an identical cylindrical container 10mm in diameter and 45mm in height (Aurovist^{TM}, Nanoprobes Inc., NY, US). In this chapter, only the GNP solution with mass percentage of 1%, 0.5% and 0.2% and the water solution are utilized for the determination of the optimal energy windows and the comparison of background estimation methods.

4.2.2 Typical experimental setup for K-shell XRF detection

As shown in Fig. 35, a typical experimental setup for K-shell XRF detection consists of a polychromatic X-ray source (L8121-03, Hamamatsu Photonics, Hamamatsu, JPN), a pencil beam collimator, a compact integrated spectrometer system (X-123CdTe, Amptek Inc., Bedford, US), and four saline solutions. The primary X-ray beam (110kVp and 500 μA) generated by a polychromatic X-ray source is shaped to produce an X-ray pencil beam after the collimation by a cylindrical hole of 4mm in diameter through a lead block with a dimension of 130mm×100mm×50mm.

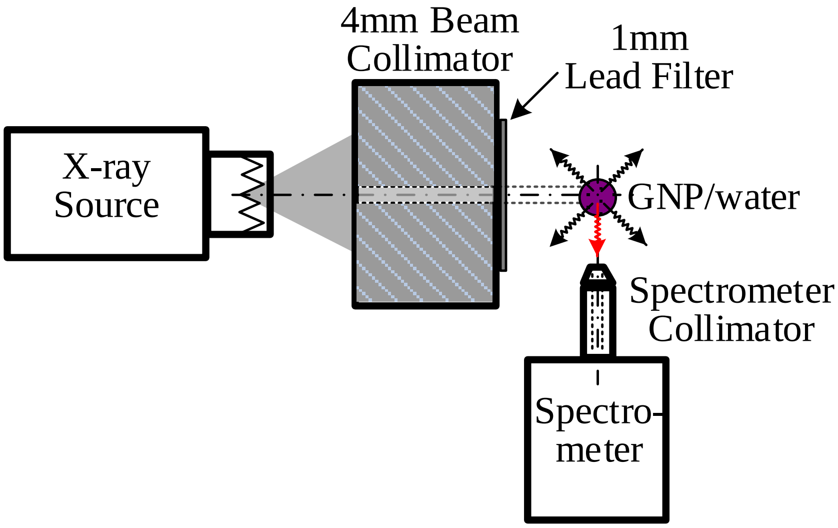

Figure 35. Schematic diagram of the experimental setup for measuring the fluorescence X-rays from GNPs, including a polychromatic X-ray source, a pencil beam collimator, a 1mm thick lead excitation filter, saline gold solutions (1.0%/0.5%/0.2% by mass percentage), and a compact integrated spectrometer system.

In this experimental setup, three common strategies are applied to effectively minimize the unwanted background such as Compton and elastically scattered X-rays and fluorescence X-rays from other elements in the phantom [21, 68]. First, a 1mm thick lead filter is placed at the exit of the pencil beam collimator to reduce the unnecessary X-rays with energies below gold K-edge binding energy. Second, the spectrometer is positioned at a 90 ° to the incident X-ray pencil beam. Last, a conically shaped lead shield with an opening end of 5mm diameter, two 2mm thick pinhole collimators with 2mm in diameter and made of alloy HD17 (90% W, 6% Ni, and 4% Cu), and a brass collimator spacer in hollow cylinder shape with 15.87mm in outside diameter, 4.98mm in inside diameter and 36.02mm in length, are used to cover the sensitive element of the spectrometer, aimed to receive the directional beam while improve the spatial resolution.

For the sake of maximizing fluorescence intensity for precise quantitative analysis, each solution is exposed at the identical position, i.e. the intersection of the incident beam and the projected area as seen by the sensitive element of the spectrometer, for as long as 500s. In order to reduce the statistical uncertainty during the data acquisition, the average of the ten acquired spectra for each GNP/water solution is utilized for further analysis.

4.3 Energy window determination of K-shell fluorescence peaks

The first goal in this chapter is to determine the optimal energy windows and corresponding neighboring energy bins for $K_{\alpha 1}$ and $K_{\alpha 2}$ gold fluorescence peaks, using the fluorescence-only spectra acquired in the experimental way. An example including the total spectrum, the water background and the subtracted fluorescence-only spectrum is shown in Fig. 36. The determination of the energy window for each fluorescence peak is of great importance to establish the linear relationship between the number of photon counts under the fluorescence peaks and the GNP concentrations. Therefore, the criterion for optimal energy window is defined as to realize the best linear relationship (e.g. largest linear coefficient of determination).

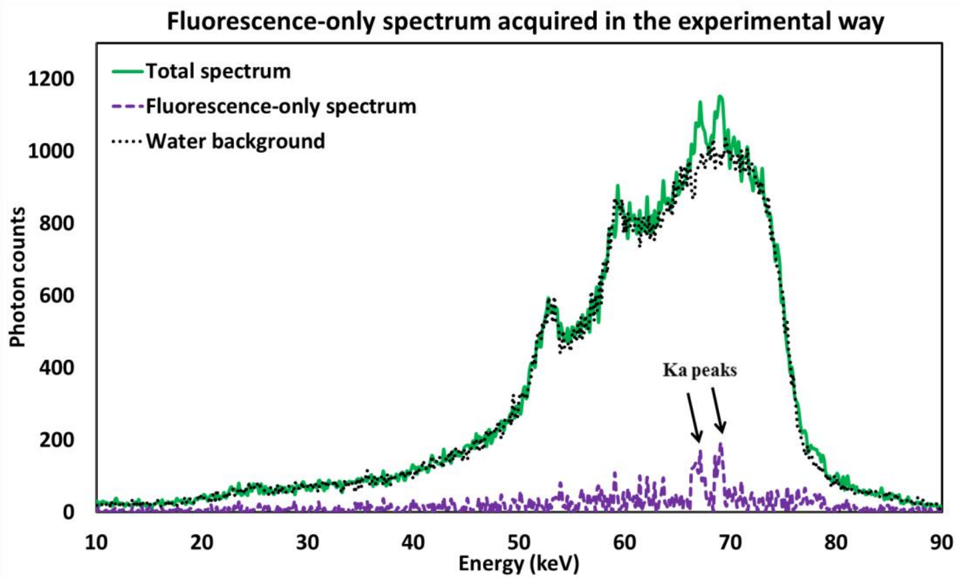

Figure 36. An example of acquired total spectrum, water background, and fluorescence-only spectrum.

The determination of optimal energy window for $K_{\alpha 2}$ and $K_{\alpha 1}$ gold fluorescence peaks with central energy at $E_{2max} = 66.99\text{keV}$ and $E_{1max} = 68.80\text{keV}$ is performed in two steps. Without loss of generality, the $K_{\alpha 2}$ peak is used as an example to demonstrate the process, as shown in the schematic diagram of two fluorescence peaks in Fig. 37 [120].

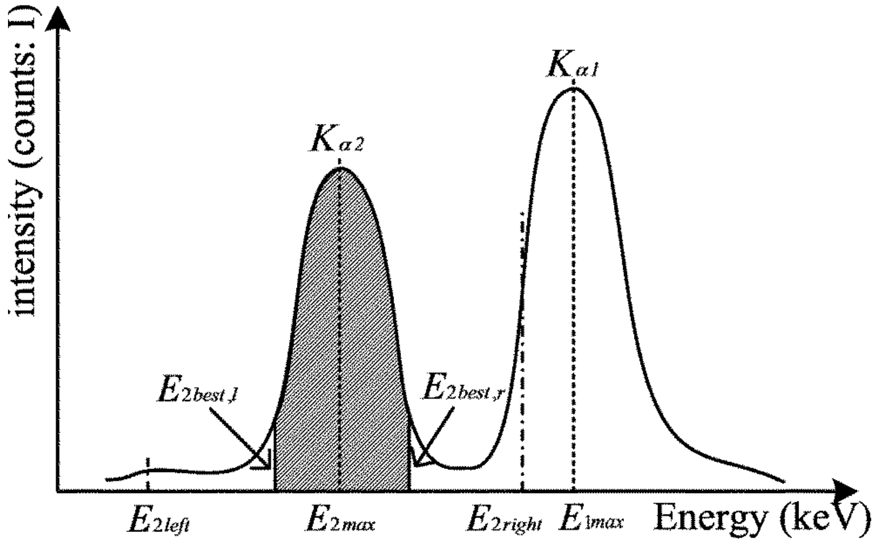

Figure 37. Schematic diagram of how to determine the optimal energy window after experimental background subtraction ($K_{\alpha 2}$ peak as an example).

The first step is to choose an extended range for $K_{\alpha 2}$ peak. The right edge (E_{2right}) is determined as the energy channel at which the count is just less than a half of that at E_{1max} on the left side of $K_{\alpha 1}$ peak. The left edge (E_{2left}) can be determined as the symmetry of E_{2right} around E_{2max}, since the gold fluorescence peaks approximately obey a Gaussian distribution.

The second step is to try all the possible symmetrical pairs around E_{2max} within the extended range and to use the photon counts within each symmetrical pair to establish the linear relationship with corresponding GNP concentrations. Then, the linear coefficient of determination (R^2) of linear fitting acquired using each symmetrical pair is calculated and compared. The pair ($E_{2best,l}$ and $E_{2best,r}$) that makes R^2 become largest is defined as the optimal energy window for $K_{\alpha 2}$ peak. Similarly, the optimal energy window for $K_{\alpha 1}$ peak can be determined as $E_{1best,l}$ and $E_{1best,r}$.

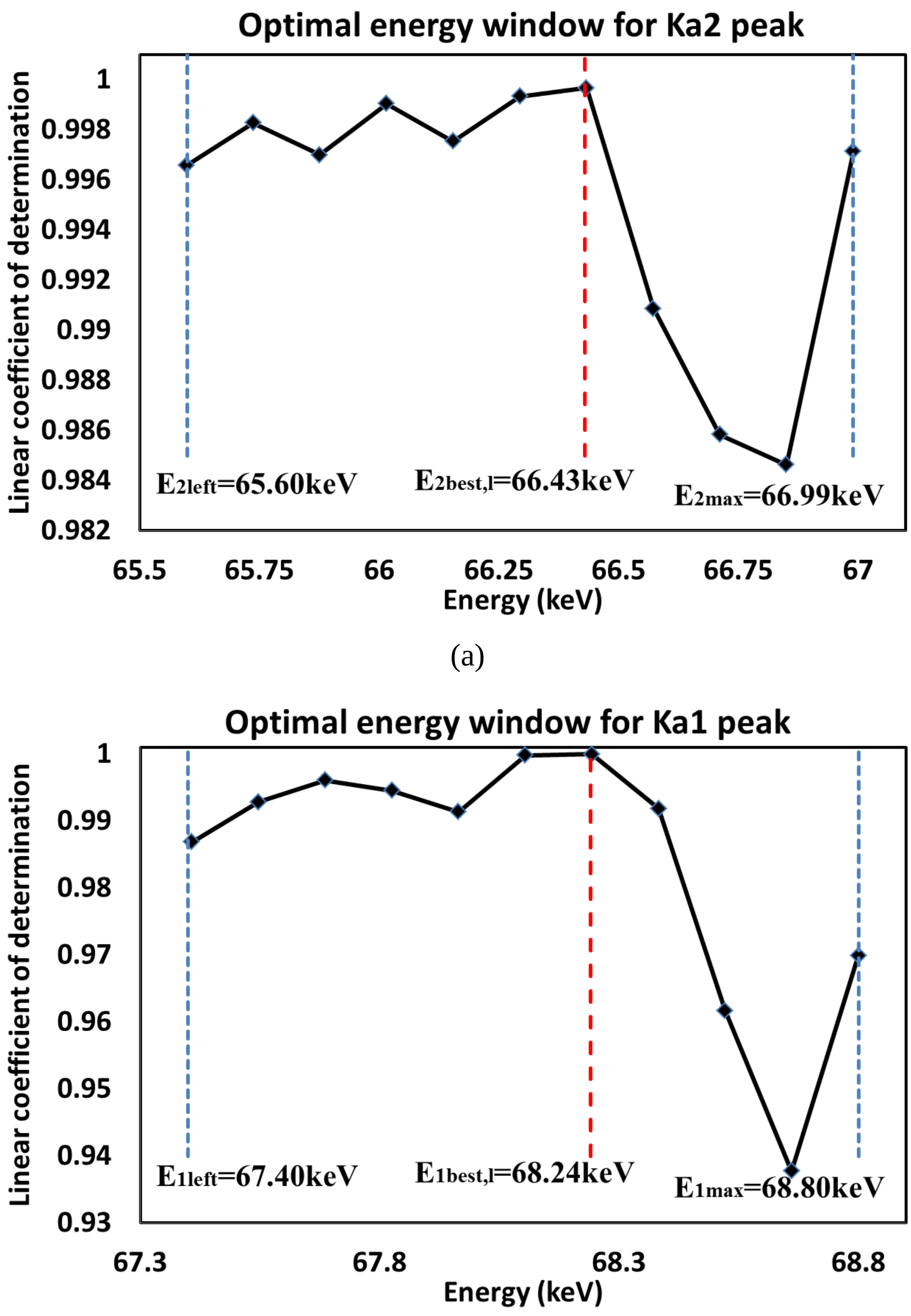

(a)

(b)

Figure 38. Optimal energy window for two K-shell fluorescence peaks: (a) 66.99±0.56keV, (b) 68.80±0.56keV.

Based on the fluorescence-only spectrum, the extended ranges are chosen as E_{2left} =65.60keV and E_{2right}=68.38keV for gold $K_{\alpha 2}$ peak, while E_{1left} =67.40keV and

E_{1right}=70.20keV for gold $K_{\alpha 1}$ peak. For each K_{α} peak of three gold solutions, the R^2 is calculated with respect to each symmetrical energy window around the maximum value within the extended range. The calculating results are shown in Fig. 38 (a) and (b), and the optimal energy windows are determined as 66.99±0.56keV (66.43~67.55keV) and 68.80±0.56keV (68.24~69.36keV) for gold $K_{\alpha 2}$ and $K_{\alpha 1}$ peaks, respectively.

4.4 Numerical methods for background estimation

Utilizing the determined neighboring energy bins, specifically (65.60~66.43keV) and (67.55~68.38keV) for $K_{\alpha 2}$, and (67.40~68.24keV) and (69.36~70.20keV) for $K_{\alpha 1}$ peak, respectively, three numerical methods are performed to estimate the background under the each fluorescence peak. Again, the $K_{\alpha 2}$ peak is used to perform these methods.

4.4.1 Trapezoidal shape estimation

In this method, the background within the optimal energy window is estimated by a trapezoidal shape. The bases can be acquired in the following two ways [120, 121]. In Fig. 39 (a), the bases are chosen as the count number at $E_{2best,l}$ and $E_{2best,r}$, the edges of the optimal energy window. In Fig. 39 (b), they are determined as the average count numbers during the energy range from E_{2left} to $E_{2best,l}$ and from $E_{2best,r}$ to E_{2right}. Then, the fluorescence-only spectra within the optimal energy window can be calculated by subtracting the background area estimated by the trapezoidal shape.

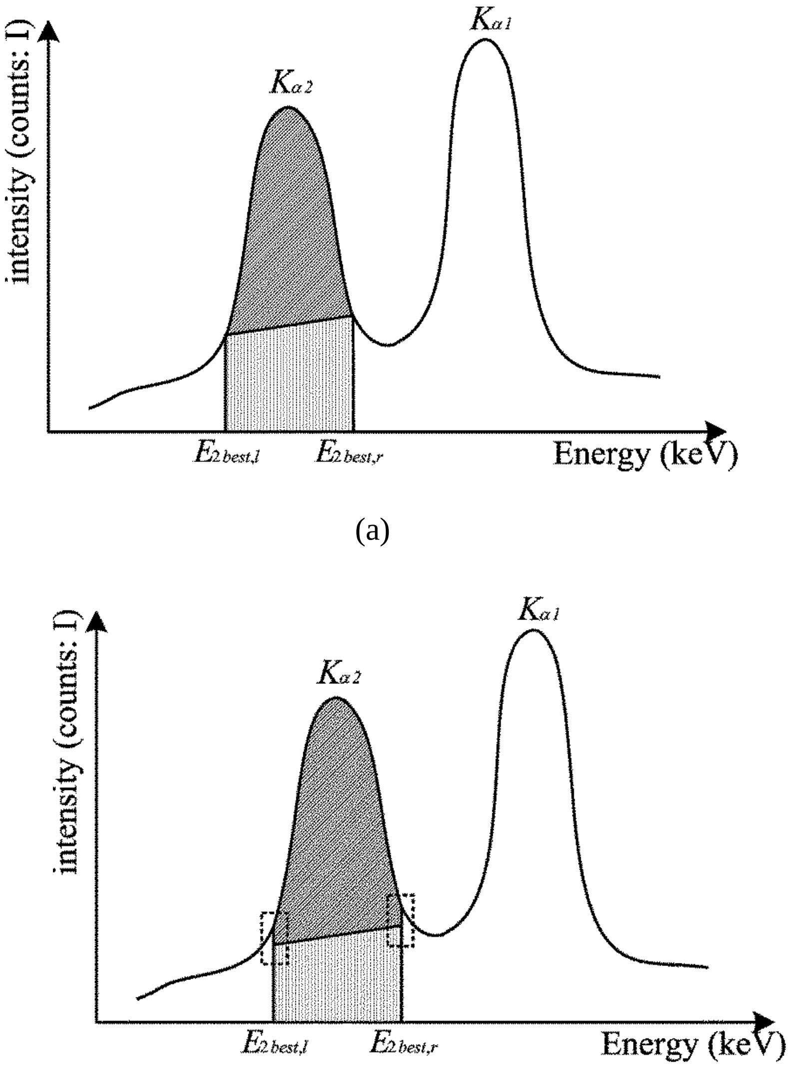

(a)

(b)

Figure 39. Schematic diagram of how to determine the background represented by a trapezoidal shape: the bases are chosen as (a) the intensities at the edges of the optimal energy window; (b) the average intensities during the ranges of neighboring energy bins.

4.4.2 Interpolation by polynomial fitting

The background within the optimal energy window is estimated by interpolation using the neighboring energy bins in this method [68, 94, 122]. Specifically, the neighboring energy bins are determined as the range from E_{2left} to $E_{2best,l}$ and from

$E_{2best,r}$ to E_{2right}. Based on these pre-known data, polynomial fittings from 1st to a 6th degree polynomial are applied and the fluorescence-only data within the optimal energy window can be calculated.

4.4.3 SNIP algorithm

Three phases are included in the SNIP (Statistics sensitive Nonlinear Iterative Peak-Clipping) algorithm [123, 124]. The log square root operator (LLS) is applied to the fluorescence spectrum $I(E)$ within the extended range in the first phase in order to compress the range of counts and enhance small peaks, as indicated in Eq. (31), where E is the energy channel and $L(E)$ is the spectrum after the LLS operation.

$$L(E) = \log\{\log[\sqrt{I(E)+1}+1]+1\}, \qquad E_{2left} \leq E \leq E_{2right} \tag{31}$$

In the second phase, $L_1(E)$, $L_2(E)$ up to $L_m(E)$ are calculated step by step, where m is determined as the channel number within either neighboring energy bins (e.g. $E_{2left} \sim E_{2best,l}$). The new value at the energy channel E in the p^{th} iteration step is obtained by the following question, where ΔE represents the energy interval between two energy channels.

$$L_p(E) = \min[L_{p-1}(E), \frac{L_{p-1}(E+p\Delta E)+L_{p-1}(E-p\Delta E)}{2}] \tag{32}$$

The background is calculated through applying an inverse LLS operator to $L_m(E)$ in the third phase.

4.5 Comparison results

Three types of typically used numerical background estimation methods are applied on the average spectra of gold solutions. Then, the average difference between the estimated background and the reference background acquired experimentally within the optimal energy window are calculated and compared in Fig. 40.

The second trapezoidal shape estimation method is superior to the first one since it involves more neighboring bins around the optimal energy window and reduces the statistical fluctuation [Fig. 40 (a)]. Lower degrees (1^{st}, 2^{nd} and 3^{rd}) of polynomial provide better performance in term of the average relative error and standard deviation [Fig. 40 (b)]. For the results of SNIP method, *m* is selected as 6 based on the consideration of making fullest use of the neighboring energy bins on each side of the optimal energy window. The performance and robustness can be greatly improved with the increase of *m* up to 6 [Fig. 40 (c)].

The combination of the average difference between estimated and true value and the corresponding variance, called as mean squared error (MSE), is applied to the second trapezoidal shape estimation method, interpolation of polynomial fitting with 1^{st} to 3^{rd} degree and SNIP algorithm when *m* is equal 6 [124], as shown in Table 4. For the sake of considering the simplicity, 1^{st} degree (linear fitting) is selected as the optimal fitting method in this dissertation to estimate the background under gold K-shell fluorescence peaks.

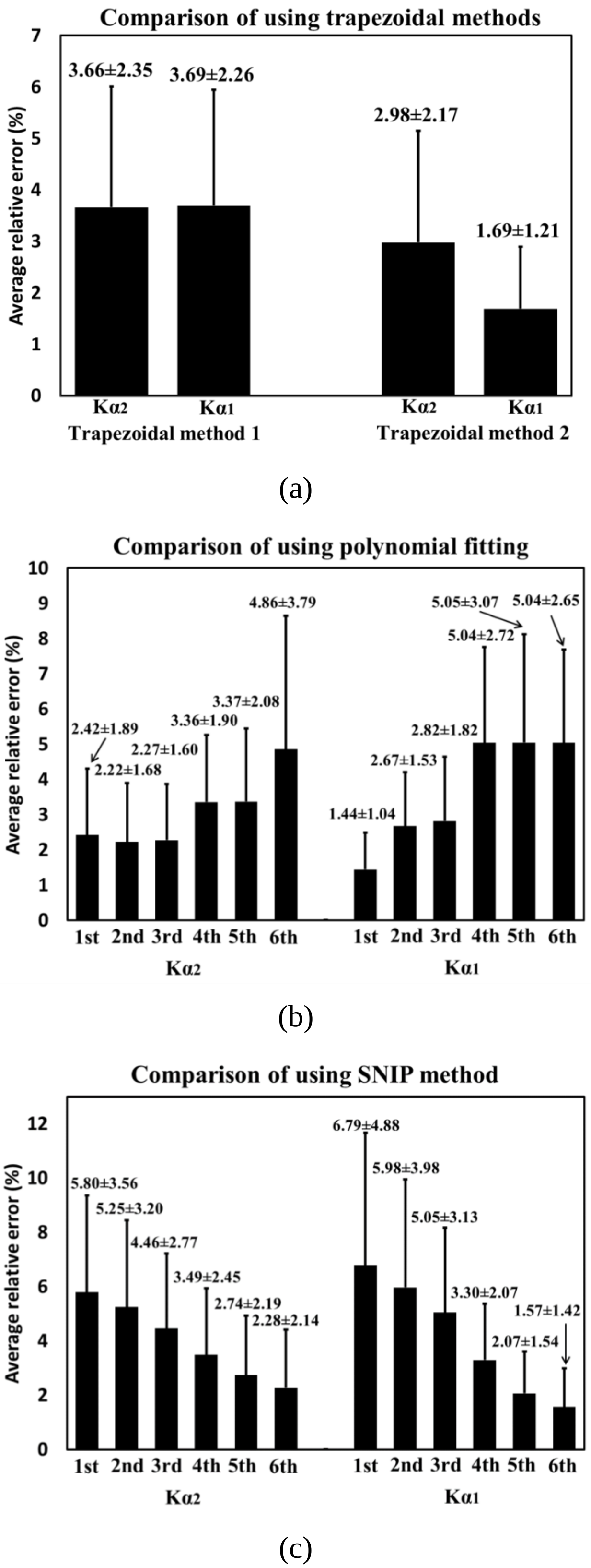
Comparison of using trapezoidal methods

(a)

Comparison of using polynomial fitting

(b)

Comparison of using SNIP method

(c)

Figure 40. Comparison of background estimation results using (a) trapezoidal shape; (b) interpolation by polynomial fitting; (c) SNIP.

$$MSE = difference^{2} + variance \tag{33}$$

Table 4. Comparison of MSE among selected methods.

MSE (%)	Second trapezoidal	Polynomial fitting 1st degree	Polynomial fitting 2nd degree	Polynomial fitting 3rd degree	SNIP (m=6)
$K_{\alpha 2}$ peak	0.136	0.094	0.078	0.077	0.098
$K_{\alpha 1}$ peak	0.043	0.032	0.095	0.112	0.045
Total	0.179	0.126	0.173	0.189	0.143

4.6 Chapter summary

Accurate background estimation is important for quantitative XRF analysis of GNPs in biomedical applications. This chapter first determines the optimal energy windows for gold K_{α} peaks using experimental data. Then, three numerical background estimation methods are performed on the fluorescence spectra of GNP solutions with mass percentages of 1.0%, 0.5% and 0.2%. Linear interpolation is suggested in this chapter based on the calculation and comparison of *MSE* values.

Chapter 5: 3D XFM of a GNP-loaded phantom

5.1 Chapter introduction

Based on the investigations performed in Chapters 3 and 4 mainly including the determination of two K-shell gold fluorescence peaks and the corresponding optimal window and background estimation methods, this chapter aims to propose and analyze a novel 3D XFM imaging modality for elemental analysis of GNPs-loaded objects in a nonliving phantom. As opposed to XFCT, this newly developed XFM imaging modality employs a directly translational imaging geometry without rotating the object. Thus, it could be potentially applied to breast cancer detection.

Breast cancer is one of the top 10 causes of death for women over age of 40 years, but the five-year survival rate can be greatly improved when it is found early [125-128]. Molecular imaging has proven beneficial in the areas of early diagnosis and treatment of cancer. It is, therefore, indispensable to enhance the way that clinicians and researchers visualize and detect complex biochemical activities at an early stage. The data generated from molecular imaging can be effectively used to identify and quantify the regions of pathology at the molecular level [68, 129]. Over the past decade nanoparticles have shown a great deal of promise as molecular imaging probes. It offers substantial improvement regarding non-invasive detection for quantitative assessment of physiological and pathological activities in living subjects [67, 70, 94].

With the aim of applying molecular imaging, specifically gold K-shell fluorescence imaging to breast cancer detection, this chapter first proposes an imaging geometry for imaging a breast with an average thickness of 44mm. then, under the condition of X-ray pencil beam and single X-ray spectrometer, as introduced in

Chapters 3 and 4, XFM imaging is performed to analyze the GNPs loaded in a nonliving phantom. The experimental method of background subtraction is employed to eliminate the background from the acquired spectrum without time-consuming processing compared with utilizing numerical methods, since the study in this chapter is performed on a phantom. All the fluorescence X-ray data obtained after the background removal can be applied to realize the reconstructed mapping directly without complex inverse processing [57, 110].

5.2 Imaging geometry for XRF imaging of breast

As a matter of fact, the penetrability of K-shell fluorescence peaks has been investigated in Chapter 3. This section is to demonstrate the imaging geometry for XRF imaging of a breast with an average thickness and explain why the penetrability implied in Chapter 3 is sufficient.

The schematic diagram with quantified parameters of the geometrical setup is shown in Fig. 41. This setup is considered in a standard Craniocaudal (CC) view in mammography, and the breast thickness is determined as an average value of 44mm (including 5 mm adipose surface layer on both sides) accordingly [130]. Without loss of generality, the excitation volumetric element (*P*) on line *A'B'* (34mm) is taken into consideration. The ranges of penetration distance for excitation (*PA*) and emission (*PB*) beams can be easily derived as below using Eq. (34) and (35) when *P* moves from *A'* to *B'*. The incident angle is defined as $\alpha = 35^\circ$, which has not been optimized in this chapter.

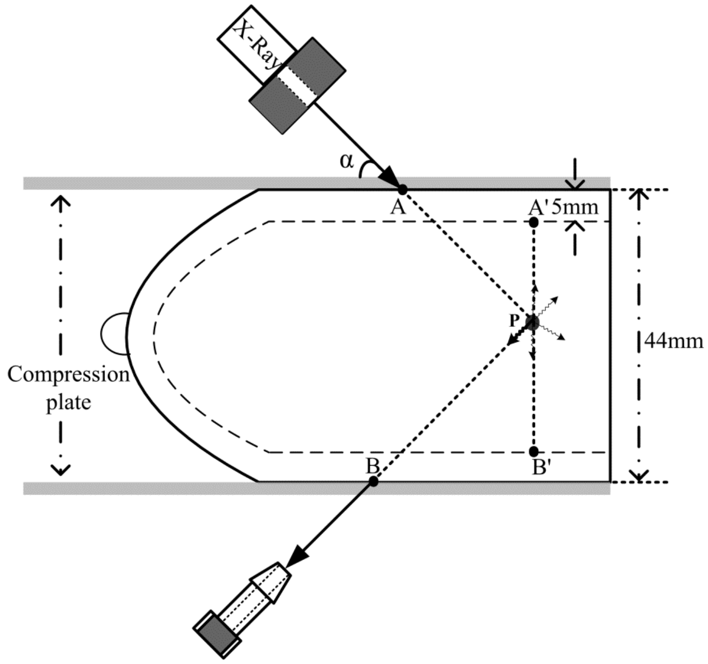

Figure 41. Schematic diagram of the geometrical setup in a standard Craniocaudal (CC) view; the distances from the focal spot of the X-ray source and the sensitive element of the spectrometer to point P of interest are determined based on engineering consideration, which are set to 147mm and 107mm, respectively in this study.

$$PA = \frac{5mm + PA'}{sin(\alpha)} = 8.72mm \sim 67.99mm \tag{34}$$

$$PB = \frac{5mm + PB'}{cos(\alpha)} = 6.10mm \sim 47.61mm \tag{35}$$

Thus, a combination of BR12 at 70mm on the excitation path and 50mm on the emission path is sufficient to measure the penetrability of fluorescence X-rays. Actually, these thicknesses can be much thicker under the condition of higher applied current intensity (mA level) and X-ray tube voltage.

5.3 XFM of a designed phantom containing GNPs

5.3.1 Preparation of phantom containing GNPs and its scanning process

The preparation of GNP and water solutions has been introduced in Chapter 4, and three GNP solutions with mass percentage of 0.2%, 0.5%, 1.0% are utilized in this chapter. However, the heights of these solutions in the sample container are 5mm, 10mm, 15mm and 15mm for 0.2%, 0.5%, 1.0% and water solution, respectively, to represent various tumor sizes. A specific cuboid phantom made of BR12 is carefully designed with three GNP-loaded regions for gold solutions and one water region for water solution. These regions are cylindrical in shape and 10.5mm in diameter, but are 5mm, 10mm, 15mm and 15mm in depth from the top of the phantom for 0.2%, 0.5%, 1.0% gold solutions and water, respectively, in an effort to fit the prepared gold and water solutions (Fig. 42). The dimensions of the BR12 phantom are 35mm in both length and width and 20mm in height. The centers of four GNP-loaded/water regions (90 ° apart) are located at 10.6mm away from the center of the phantom.

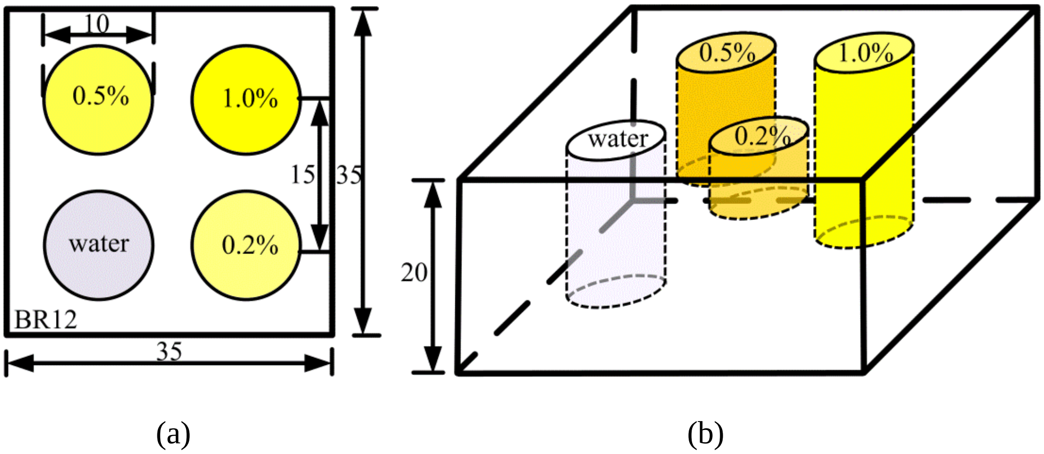

(a) (b)

Figure 42. Schematic diagram of the cuboid BR12 phantom with four cylindrical regions for 0.2%, 0.5%, 1.0% gold solutions and water: (a) Plan view; (b) 3D view (Unit: mm).

Similarly, the experimental setup for quantitatively mapping the designed phantom is shown in Fig. 43. It is noted that, in this setup, the object is replaced by the designed phantom containing GNPs, while all the other components and common strategies used to minimize the unwanted background are unchanged compared with the schematic in Chapters 3 and 4. The distances from the focal spot of the X-ray source and the sensitive element of the detector to the excitation volumetric element within the phantom are as short as 107mm and 87mm, respectively, in an effort to reduce the divergence of the pencil beam and increase the intensity of the fluorescence X-rays coming from the GNPs. The cuboid BR12 phantom is designed to translate along three mutually perpendicular directions (X, Y and Z) with the combination of three high precise linear translational stages (423, Newport, Irvine, US), while the X-ray source and the spectrometer are stationary. The collimated X-ray pencil beam is normally incident on the phantom (Y-Z plane), and therefore, the excitation volumetric element is determined as the intersection of the X-ray pencil beam and the projected area as seen by the sensitive element of the spectrometer.

During the experiment (Fig. 44), data acquisition is started from the volumetric element at the left corner on the top plane [center coordinate (2.5 2.5 17.5)] of the phantom. Data acquisition is paused during the movement of the phantom to next translational position after the data collection for 500s at each position. The phantom is then translated to next position by $\Delta y = 5mm$ along the Y direction after the data collection of previous position until completing the volume scan. The scanning process resumes again after the phantom being translated to next volume by $\Delta x = 5mm$ and this process is repeated until the data acquisition of the full plane is completed. Finally, the data acquisition over the whole phantom can be finished by scanning each plane of the phantom with $\Delta z = -5mm$.

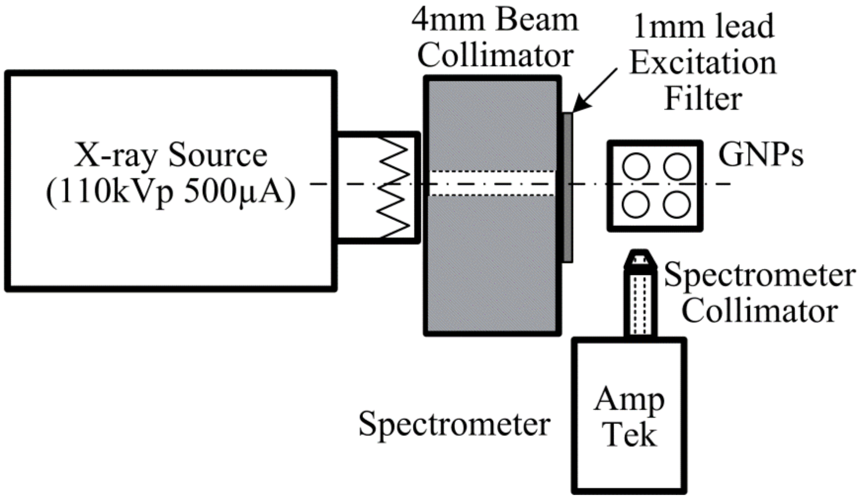

Figure 43. Schematic diagram of the experimental setup for quantitative mapping the designed phantom.

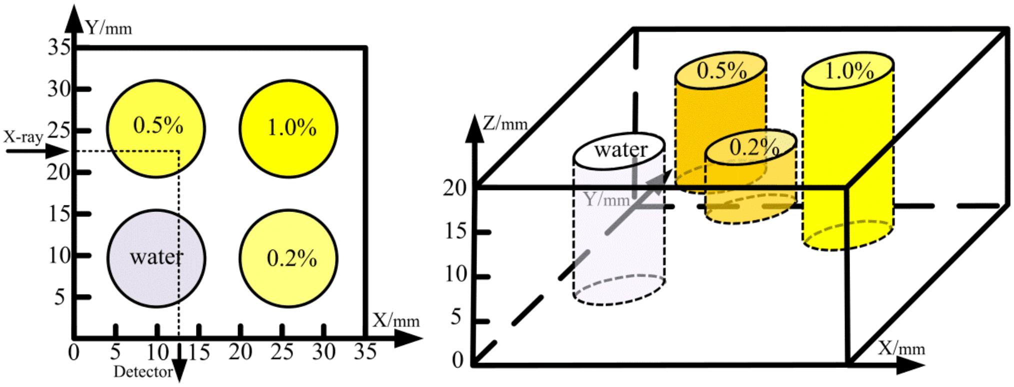

(a) (b)

Figure 44. Schematic diagram of the XFM scanning process with moving steps of 5mm in X, Y, Z directions: (a) Example of scanning at position (12.5, 22.5, 17.5); (b) Four planes in the scanning in Z direction.

5.3.2 Background subtraction and fluorescence data acquisition

The deficiency of estimating the background in the experimental way has been discussed in Chapter 4. However, since the study in this chapter is performed on a nonliving and homogeneous phantom, the experimental method is still employed to estimate and remove the background. The scan for obtaining the background spectra can be performed either before or after the scan for acquiring the fluorescence spectra in this phantom study. The GNP solutions within the phantom are substituted by equivalent water solutions while keeping the identical positions. Then, a second scanning process as described in 5.3.1 is followed to get exact background spectra for each correspondingly volumetric element.

According to the results in Chapters 3 and 4, the fluorescence counts under gold $K_{\alpha 1}$ and $K_{\alpha 2}$ peaks at 68.80keV and 66.99keV are collected for subsequent processing and their energy windows are 66.99±0.56keV (66.43~67.55keV) and 68.80±0.56keV (68.24~69.36keV), respectively. The summation ($K_{\alpha 1}+K_{\alpha 2}$) is used to realize the 3D reconstruction and to analyze the linear relationship between fluorescence signal intensity and GNP concentration.

As presented in Chapter 3 concerning the challenges for a precisely quantitative imaging analysis, the fluorescence counts obtained after the background subtraction and data acquisition cannot be directly applied to map the phantom because of the attenuation effects. The attenuation difference for each volumetric element within the phantom must be carefully considered and calibrated, the details of which will be discussed in the following section.

5.3.3 Attenuation analysis and determination of calibration factor (CF)

As discussed in Section 3.3 in Chapter 3, the detected and extracted fluorescence counts encounter the attenuation effects in both of the excitation path and the detection path inside the object. The attenuation terms (At) represented as terms B and C in Eq. (29) are rewritten as below in Eq. (36), and the calibration factor (CF) is defined as in Eq. (37). Through multiplying the *CF*, the detected fluorescence counts could be calibrated.

$$At = \underbrace{\int_{E_{k-edge}}^{E_{max}} I_0(E')\,exp[-\int_{-\infty}^{x} \mu_{ex}(E', x')dx']dE'}_{B} \times \underbrace{exp\{-[\int_{-\infty}^{y} \mu_{em}(E_F, y')dy']}_{C} \tag{36}$$

$$CF = \underbrace{\int_{E_{k-edge}}^{E_{max}} I_0(E')\,exp[\int_{-\infty}^{x} \mu_{ex}(E', x')dx']dE'}_{B} \times \underbrace{exp\{[\int_{-\infty}^{y} \mu_{em}(E_F, y')dy']}_{C} \tag{37}$$

Several aspects are considered to simplify the expression of the *CF* in Eq. (37). When a piece of Pb filter (1mm in this chapter) is applied, the majority of X-ray photons capable of exciting K-shell X-ray fluorescence photon are located within a narrow energy range from 80.7keV to 88keV, as indicated in Fig. 21 in Chapter 2. The attenuation coefficients for the incident excitation beam, μ_{ex} , can be considered as a constant value for each material under mean energy ($\overline{E}$) during 80.7~88keV, which is determined using Eq. (38), where $N(E)$ represents the X-ray counts at energy E in the excitation spectrum.

$$\overline{E} = \frac{\int_{E_{k\text{-}edge}=80.725keV}^{E_{max}=88keV} EN(E)dE}{\int_{E_{k\text{-}edge}=80.725keV}^{E_{max}=88keV} N(E)dE} \tag{38}$$

Also, considering that the highest concentration of the gold solutions within the BR12 phantom is as low as 1.0% mass percentage and the comparison of LACs between water and BR12 in Fig. 45, the *CF* can be further simplified. In Fig. 45, though the LACs between water and BR12 are quite different when the X-ray energy is lower than 40keV, they are quite close during the high X-ray energy range from 60keV to 100keV (and above 100keV without showing in Fig. 45). The relative average deviations calculated under the energy of 60keV, 80keV and 100keV are 3.23%, 2.71% and 2.31%, respectively. Thus, the *CF* can be simplified as in Eq. (39) because both of the interesting energies for excitation (80.725~110keV) and emission (65.99~69.80keV) beam for calibration are above 60keV.

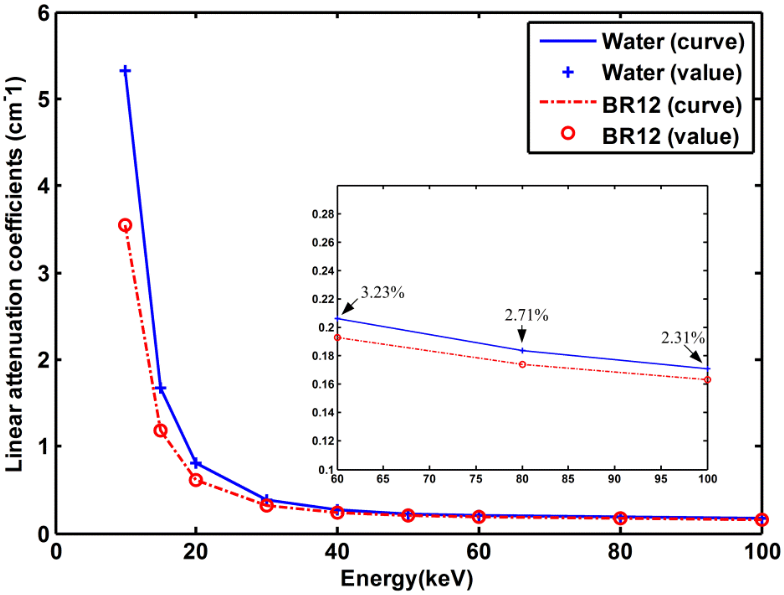

Figure 45. Comparison of LACs between water and BR12, with amplification of the energy range from 60keV to 100keV, where the data of the LACs for BR12 and water are acquired from the specifications of BR12 and the National Institute of Standards and Technology (NIST, US), respectively [131, 132].

$$simplified\ \ CF = \int_{E_{k-edge}}^{E_{max}} I_0(E')dE' \times exp[\mu_{ex}|_{E=\bar{E}}\ x] \times exp\{[\mu_{em}|_{E=70keV}\ y] \qquad (39)$$

Where $\mu_{ex}|_{E=\bar{E}}$ and $\mu_{em}|_{E=70keV}$ indicate the LACs under the mean energy calculated using Eq. (38) and 70keV, respectively, for BR12. Thus, the collected fluorescence counts of gold K_{α} peaks can be effectively calibrated by multiplying the simplified *CF*, and the calibrated XRF signal is linearly proportional to the GNP concentration.

$$I_2(x,y)|_{\text{calibrated}} = I_2(x,y) \times simplified\ \ CF \tag{40}$$

Finally, the unattenuated/calibrated fluorescence counts of gold K_{α} peaks for each excitation volumetric element within the phantom can be obtained after attenuation calibration. The real counts are used to investigate the linearity between fluorescence counts and gold concentration and to realize the 3D reconstructed mapping of the phantom.

5.4 Results

5.4.1 Typical spectra and spatial resolution validation

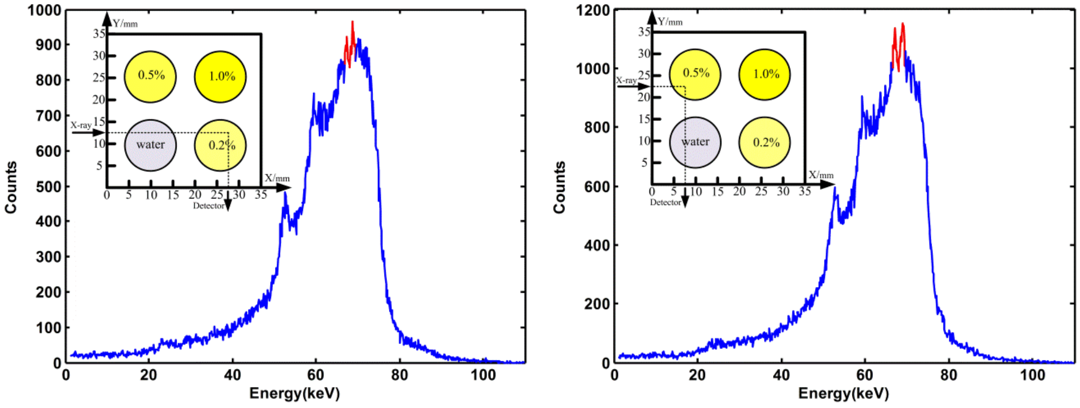

(a)

(b)

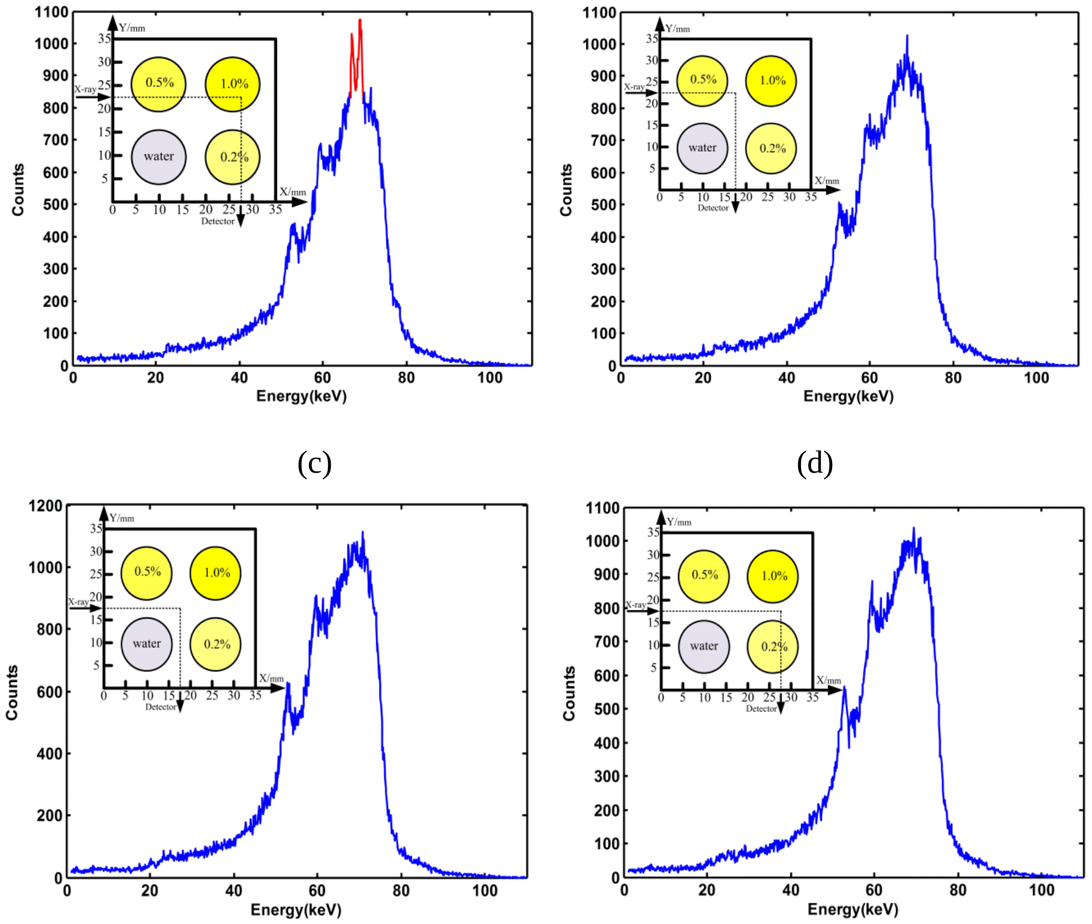

(c) (d)

(e) (f)

Figure 46. Six typical spectra obtained at representative positions within the phantom; two obvious peaks can be observed when gold solution is excited while its fluorescence X-rays is detected by the spectrometer: (a) 0.2% gold solution; (b) 0.5% gold solution; (c) 1.0% gold solution; while there is no fluorescence X-rays from GNPs can be detected: (d) 0.5% and 1.0% gold solution on the excitation path but no solution on the emission (receiving) path; (e) no gold solution on both excitation and emission (receiving) paths; (f) no gold solution on the excitation path but 1.0% and 0.2% gold solution on the emission (receiving) path.

Spatial resolution is of great importance for the implementation of XFM. The lateral resolution (X-axis direction), vertical resolution (Y-axis direction) and depth resolution (Z-axis direction) in this XFM system are determined by both spectrometer collimator and pencil beam collimator, which are 2mm and 4mm in diameters as mentioned in the preceding discussion. Six typical spectra obtained at representative positions within the phantom are shown in Fig. 46. In Fig. 46 (a), (b), and (c), two obvious gold K_α peaks from gold solutions with 0.2%, 0.5% and 1.0% mass percentage can be observed when gold solution is excited by the incident X-ray while the fluorescence X-rays is detected by the spectrometer. In contrast, no fluorescence X-rays from GNPs can be detected when there is no gold solution present at the intersection of the excitation path and the emission path. Thus, the spatial resolution can be validated in this way.

5.4.2 Background subtraction

It is assumed that the interactions among different GNPs during the spectrum detection are negligible because of the low concentration of GNPs. The assumption can be verified by the result shown in Fig. 47, in which the relative average deviation during the energy range from 65keV to 70keV between the two spectra is less than 1.28% and the Pearson correlation coefficients under energy ranges of 0keV~110keV, 40keV~85keV and 65keV~70keV are 0.999, 0.998 and 0.985, respectively.

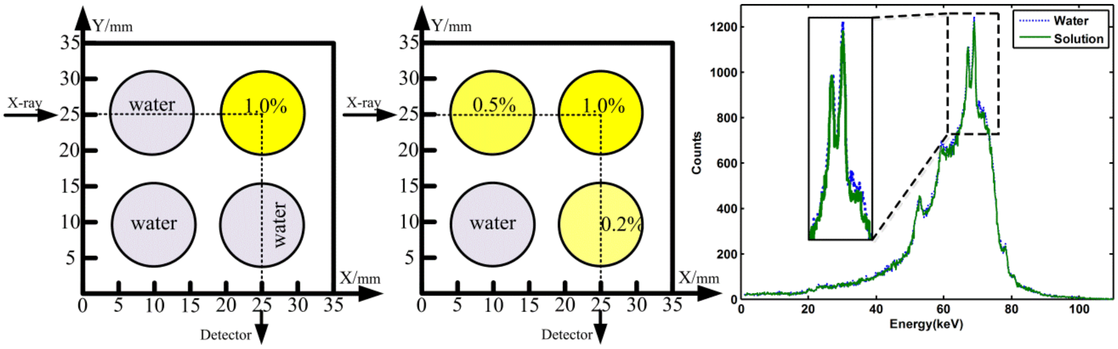

(a) (b) (c)

Figure 47. Comparison of spectra when the excitation and emission paths are blocked by (a) water or (b) solution; (c) spectra comparison with relative average

deviation (65keV~70keV) as low as 2.55% while Pearson correlation coefficients 0.999 (0keV~110keV), 0.99 (0keV~110keV), 0.998 (40keV~85keV) and 0.985 (65keV~70keV)

Thus, the method of background subtraction can be implemented to extract the fluorescence X-rays based on the diagram indicated in Fig. 48 (a). The results of typical spectra for GNP solutions with different concentrations from 0.2% to 1.0% are also shown in Fig. 48 (b) - (d). All the fluorescence counts during the energy windows of 66.99±0.56keV and 68.80±0.56keV for gold $K_{\alpha 2}$ and $K_{\alpha 1}$ fluorescence peaks are collected for subsequent processing.

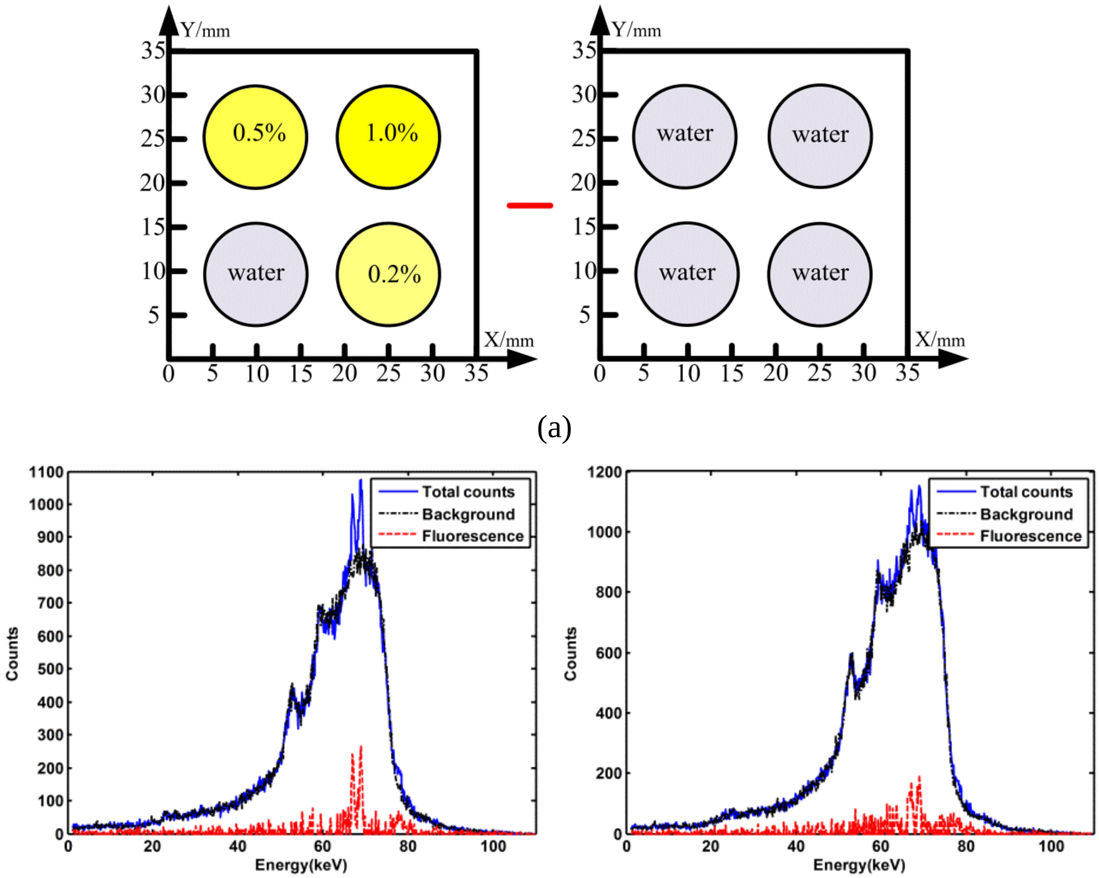

(a)

(b)

(c)

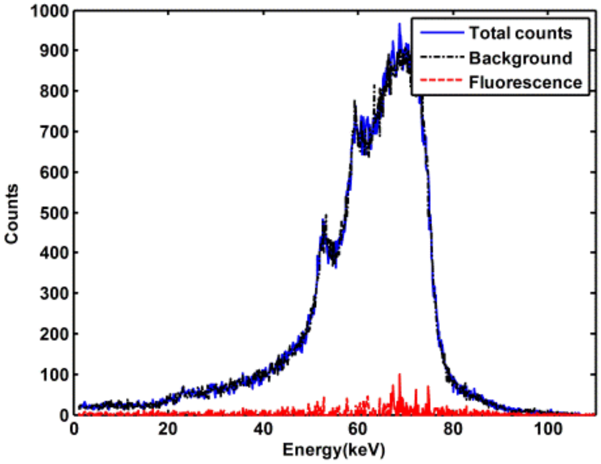

(d)

Figure 48. (a) Diagram for background subtraction; Background subtraction results for (b) 1.0% gold solution; (c) 0.5% gold solution; (d) 0.2% gold solution.

5.4.3 Attenuation calibration and 3D mapping

After the background subtraction and data collection, all the attenuated fluorescence counts collected within the energy windows are obtained. In order to map the phantom accurately, it is necessary to make the attenuation calibration by multiplying the simplified CF derived in 5.3.3. The calibration map computed by Eq. (39) is shown in Fig. 49.

All the real fluorescence counts can be derived from the attenuated counts by multiplying corresponding simplified *CF* and then used for 3D mapping. Through converting to 256 gray-level images, the reconstructed mapping results for four planes from top to bottom with distance interval of 5mm are demonstrated in Fig. 50.

The average fluorescence counts value for GNP solutions with concentrations of 0.2%, 0.5% and 1.0% mass percentage are used to analyze the linear relationship between fluorescence counts and concentrations. The good linearity ($R^2 = 0.9996$) and discrete average fluorescence counts with their standard deviations are shown in Fig. 51.

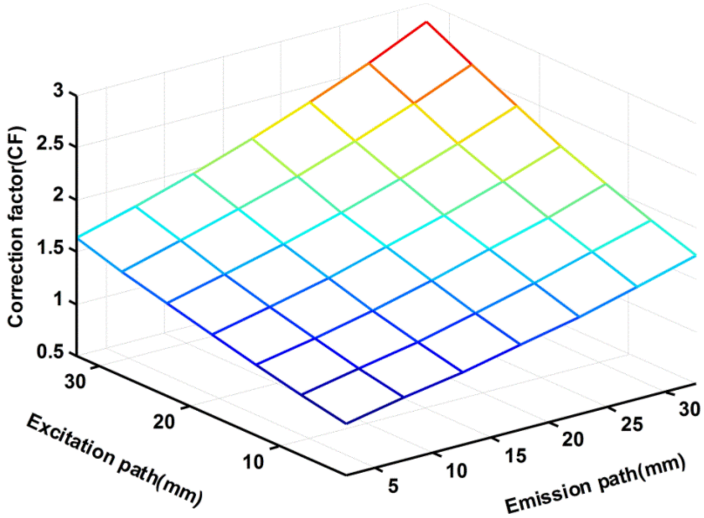

Figure 49. Calibration map for each imaging plane within the BR12 phantom.

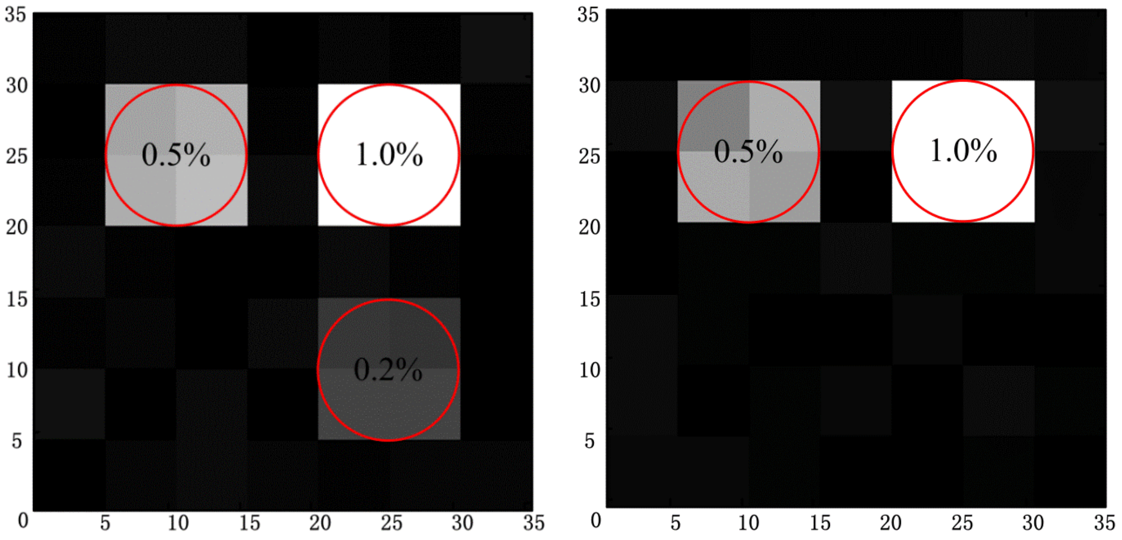

(a)

(b)

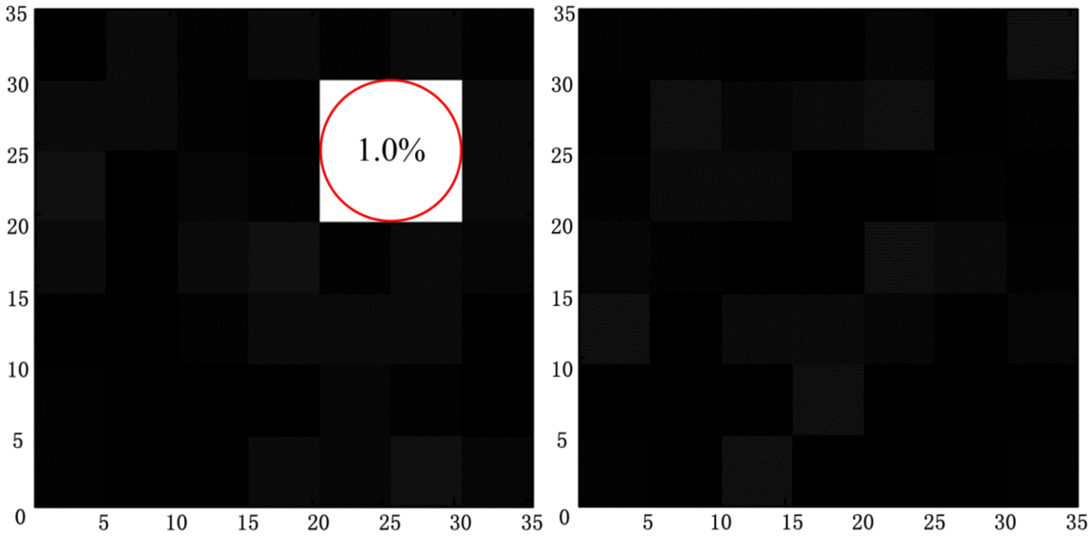

(c) (d)

Figure 50. Reconstructed mapping results for four planes from top to bottom of the phantom with distance interval of 5mm: (a) z=17.5mm; (b) z=12.5mm; (c) z=7.5mm; (c) z=2.5mm.

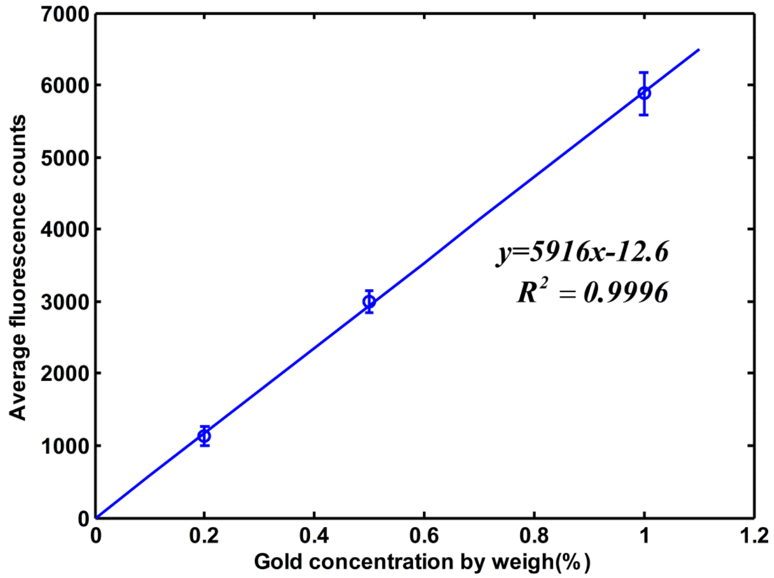

Figure 51. Linear relationship between the average fluorescence counts and the concentrations of GNP solutions.

5.5 Discussion

This chapter investigates the feasibility of the current XFM modality for identifying the bio-distribution and quantifying the amount of GNPs simultaneously in the designed BR12 phantom. Although the results of the feasibility study are encouraging, it is not yet practical for routine *in vivo* applications. Several limitations and improvements are discussed as follows.

5.5.1 X-ray beam geometry and detector arrays

As a proof-of-concept, the investigation is performed under the condition of X-ray pencil beam and single X-ray spectrometer. Also, the scanning time of 500s for each position is quite long due to low current level (500 μA in this chapter). Therefore, without considering the time used for a background scan, 27.2h is needed for the entire data collection process using the current XFM modality with moving steps of 5mm in three dimensions. If the moving step remains unchanged while the pencil beam and 1D spectrometer array with 7 detectors are employed, the data acquisition can be completed in 3.89h. Furthermore, only 0.56h are necessary for overall phantom scanning when an X-ray fan beam produced using a slit collimator and a 2D detector array is applied. In the meantime, the scanning time can be further reduced by utilizing new X-ray source with high current level (mA level). While it offers the potential to shorten the scanning time for XFM data acquisition, the employment of fan beam, 1D/2D spectrometer array and new X-ray source might dramatically increase cost and hardware complexity. Also, much more complicated photon scatter profile (i.e., the significant increase of the interference between fluorescence photons and scatter photons) poses a challenging issue compared with the current XFM modality, which may set higher requirements of collimation. However, these approaches still provide a critical step and direction toward the preclinical and clinical applications of the XFM system [57, 91, 92].

5.5.2 X-ray scanning resolution

In this investigation, the theoretically highest resolutions of 2mm, 4mm and 2mm in X, Y, and Z scanning directions are determined by the diameter of the excitation and emission collimators. Since each gold solution is scanned in the same way in this feasibility study, the partial volume effect is not yet a big issue to influence the estimation of average fluorescence X-ray counts. However, attention must be paid when the proposed XFM technique is used for clinical applications especially with unknown tumor size and distribution, since the partial volume effect can be a big problem due to the limited resolution as in this study. In order to restrain this effect, the mapping resolution must be greatly improved through reducing the collimator diameters and matching the scanning steps with these diameters in each direction. With higher resolution, the partial volume effect could be effectively decreased. Due to the smaller collimator diameters, the average count rate received by the spectrometer and consequently the quality of the reconstructed mapping image are also decreased, and the scanning time needed is increased. A tradeoff between enough average count rate, sufficient mapping resolution and reasonable scanning time, therefore, should be comprehensively considered and balanced in further studies, with a purpose to make this XFM modality possible and feasible in clinical practice [91, 92].

5.5.3 Attenuation calibration

The attenuation coefficients of BR12 and water/solution are taken as *a priori* knowledge due to their homogeneous property as we discussed in the parts of phantom preparation and attenuation calibration. However, this *a priori* knowledge based method can only provide a rough estimate when the XFM technique is applied for breast cancer detection, since the LAC varies with different components (adipose, glandular, and tumor) in a realistic breast even under the condition of high diagnostic X-rays energies (65keV and above) and low GNP concentrations [133]. It is also difficult to determine a weighted average LAC of adipose, glandular and tumor due to their varied distribution in the breast for each patient. An accurate attenuation map of the imaged object therefore is necessary. The Compton scattering technique may provide the possibility to achieve this goal during the acquisition and processing of gold fluorescence data [134]. Also, other attenuation calibration methods such as absorption- and geometry-correction can be adopted and improved to avoid the necessity of an accurate attenuation map [122]. The above discussion indicates the research direction of an accurate 3D mapping in the future.

5.6 Chapter summary

The XFM modality is investigated in this chapter to realize mapping of a specific phantom containing GNPs-loaded objects with low concentration using X-ray pencil beam and single spectrometer. The 3D reconstructed mapping results show the capability of this modality to identify the positions and quantify the concentrations of GNPs-loaded objects. In next chapter, the XFM imaging modality will be applied to image a breast phantom, especially focusing on the detection and evaluation of tumors located in the posterior aspect of the breast and adjacent to the chest wall musculature.

Chapter 6: XFM detection of posteriorly located breast tumors

6.1 Chapter introduction

According to the latest cancer statistical data from the American Cancer Society in 2015, breast cancer is ranked first in cancer incidence and third in cancer mortality rates in women of the United States. Since the implementation of mammography-based breast cancer screening in 1989 and the continuous improvements in cancer surgery and therapeutic treatment methods over the last 20 years, the morbidity and mortality rates of breast cancer have steadily decreased [135]. Although mammography is the current "gold" standard in the population-based breast cancer screening [136], its detection sensitivity varies widely due to many factors including the breast density and tumor location. For example, the detection and evaluation of tumors located in the posterior aspect of the breast and adjacent to the chest wall musculature is limited by the geometry of mammography. The inadequate breast positioning and compression of posterior tissues in certain patients result in the tumors located in the posterior region totally or partially invisible in the mammograms, in particular in CC view mammograms [137]. Although in Mediolateral oblique (MLO) projection more top posterior region can be imaged, imaging breast parenchyma near or overlying the chest wall musculature remains a challenging task because the posterior tissues are generally thicker and the pectoralis muscle may obscure breast lesions due to its higher density on mammogram [138, 139]. Hence, in order to improve detection sensitivity of breast tumors located in the posterior regions, a different imaging geometry and/or signal acquisition method is required.

XRF based techniques capable of identifying and quantifying molecular imaging probes have been proposed [110, 122]. Conjugated to antibodies or other proteins, GNPs can be functionalized to act as markers for different tumor characteristics, such as the breast tumors located posteriorly [86, 140]. This is the reason why the tumor information could be acquired through detecting the bio-distribution and concentration of the GNPs targeted to the breast tumors. XFCT technique has proved capable of simultaneously providing spatial distribution and quantification of bio-conjugated GNPs [68, 70]. However, a known limitation of current approaches to breast CT is inadequate to image the posterior breast, chest wall and axilla; thus, accurate quantification of GNP uptake into tumors may not be feasible or reproducible using XFCT.

Because XFM uses directly translational imaging geometry to acquire the detection signals emitted from the deep posterior breast tissues that are excluded by the conventional mammographic or CT imaging geometry, XFM may be another useful tool suited for imaging the breast to provide supplementary information to mammography [21]. In this chapter, several clinically relevant issues such as breast compression, breast positioning and scanning trajectory are reviewed and a phantom study using tissue-equivalent gel and BR12 is conducted to investigate the feasibility of applying the XFM technique to breast cancer detection, especially to the breast tumors located posteriorly.

6.2 Materials and methods

6.2.1 Compression, view selection and scanning trajectory

Breast compression is essential in clinical mammography to reduce both breast thickness and absorbed dose and improve image quality through better separating tissue components [141-143]. Compression is also important for the application of XFM technique for breast cancer detection, because it reduces the travelling paths of both excitation and emission X-rays, enhancing the fluorescence output. In this chapter, we employ the standard MLO projection to evaluate the scanning trajectory for XFM.

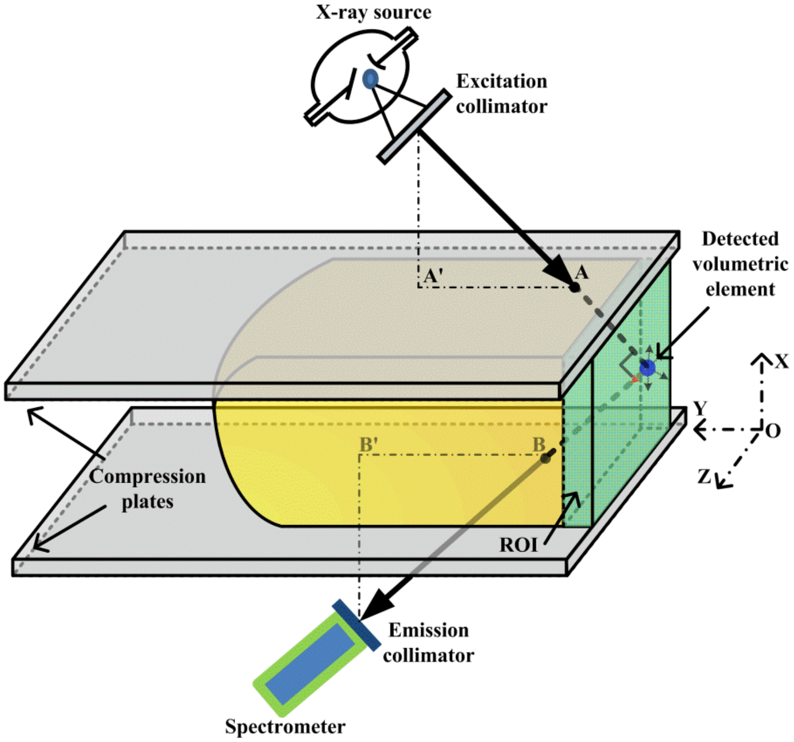

Figure 52. Schematic diagram of the clinical setup in the MLO view, showing the scanning trajectory using pencil-beam X-ray and single spectrometer; the ROI highlighted in green represents the posterior aspect of the breast and the adjacent pectoralis major muscle.

A schematic diagram of the clinical setup in the MLO view is shown in Fig. 52, where the ROI representing the posterior aspect of the breast as well as the adjacent pectoralis major muscle is highlighted in green. The X-ray pencil-beam and the single spectrometer are used to present the scanning trajectory when the XFM technique is applied to image the ROI area. The plane (A'ABB') containing the incident X-ray and the detected X-ray (fluorescence X-ray and scatter X-ray) is parallel to the X-Y coordinates. The specific system geometry of 90 ° between incident and detected X-ray makes it feasible to scan each element in the ROI through synchronized translation between X-ray source and spectrometer [21].

6.2.2 Phantom preparation and scanning process

A specific tissue-equivalent gel phantom with cuboid shape is designed to represent the central part of a compressed breast in the MLO view [Fig. 53 (a)]. The dimensions of the gel phantom are 70mm in both length and width and 48mm in thickness to mimic the average thickness of a compressed breast in the MLO view [144]. A piece of 10-mm-thickness BR12 is attached to the back of the gel phantom, representing the ROI of the posterior aspect of the breast as well as the adjacent pectoralis muscle. Two GNP solutions of 0.5% and 1.0% mass percentage are embedded in the ROI (BR12) to resemble possible gold bio-distribution and concentration attached and absorbed by tumors [86]. More detailed parameters of the phantom are shown in Fig. 53 (b).

Similar experimental setup is used in this chapter except the imaged object, as shown in Fig. 54. Without loss of generality, one line MN (X=0-h, Y=5mm, Z=43mm) in the ROI is selected to illustrate the scanning process (Fig. 55). During the experiment, data acquisition is started from the top volumetric element (X=0) with data collection of 300s. Data acquisition is paused during the translation of the phantom to next position by $\Delta x = 1mm$ along the X direction. The collection resumes after each translation until completing the line scan. The whole size of the ROI can be covered by repeating the line scan process with moving steps of $\Delta y = \pm 1mm$ and $\Delta z = \pm 1mm$ in Y and Z directions.

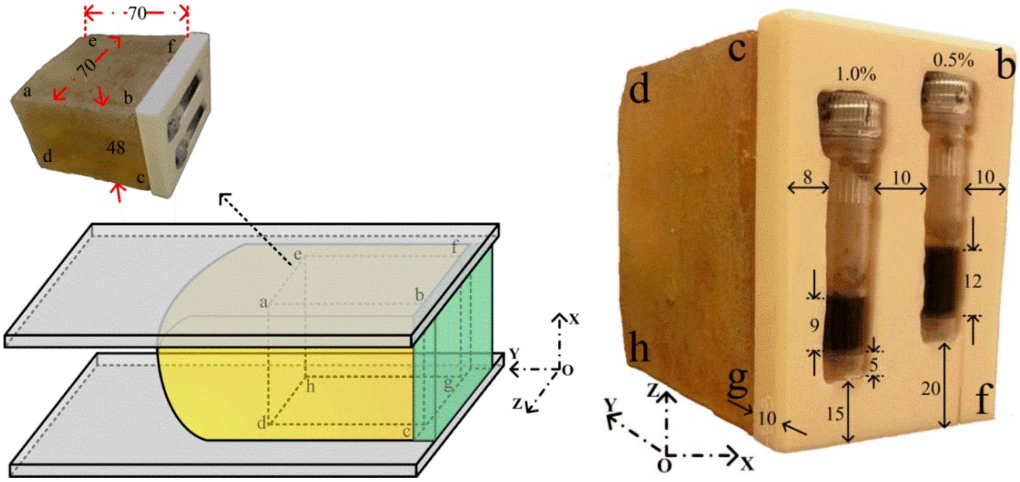

(a) (b)

Figure 53. (a) Tissue-equivalent gel phantom representing the central part of a compressed breast in the MLO view; (b) a piece of 10-mm-thickness BR12 embedded with 2 gold solutions representing the ROI with possible tumor/GNP foci (Unit: mm).

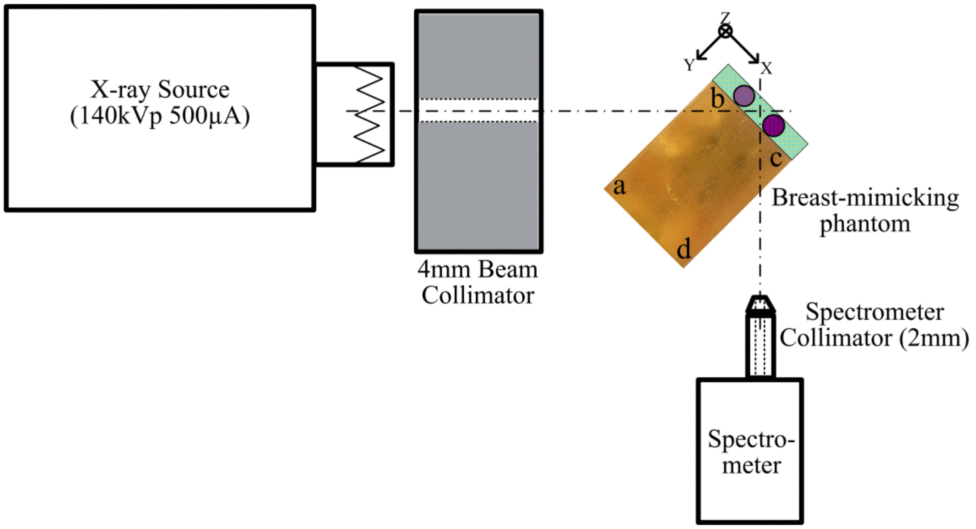

Figure 54. Top-down schematic diagram of the experimental setup.

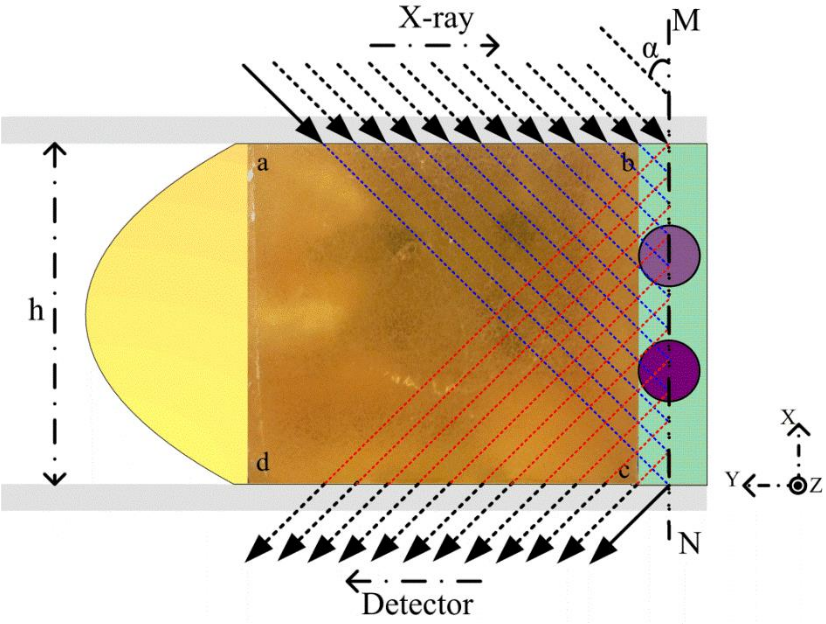

Figure 55. Schematic diagram for scanning process of the typical line MN. The whole scanning process is considered as an integration of many repeated line scans.

6.2.3 Determination of optimal incident angle

Though the angle between the incident X-ray and the detected fluorescent light ray is fixed at 90° to minimize the unwanted background, the incident angle (shown as α in Fig. 56) of the collimated X-ray pencil-beam, in theory, can be adjusted from 0° to 90°. We hypothesize that an optimal incident angle exists in this range, leading to the least attenuations of both incident and detected X-rays and achieving maximum fluorescence intensity. To test this hypothesis, the following derivation is performed.

Considering the homogeneity of gel and BR12 and the similar attenuation effects between gel and BR12 under high energies, the attenuation factor (AF) in Fig. 56 can be derived as below in Eq. (41), based on the analysis in 5.3.3 in Chapter 5.

$$AF = exp(-\mu_p s - \mu_p' t) \tag{41}$$

Where μ_p is the LAC of the gel phantom/BR12 at the mean energy in the range of 80.725keV to 140keV; μ_p' is LAC of the gel phantom/BR12 at gold K_α energy of around 70keV; s and t are the distances from incident point A to $p(x, \mathrm{y}, \mathrm{z})$ and from $p(x, \mathrm{y}, \mathrm{z})$ to emitted point B, respectively.

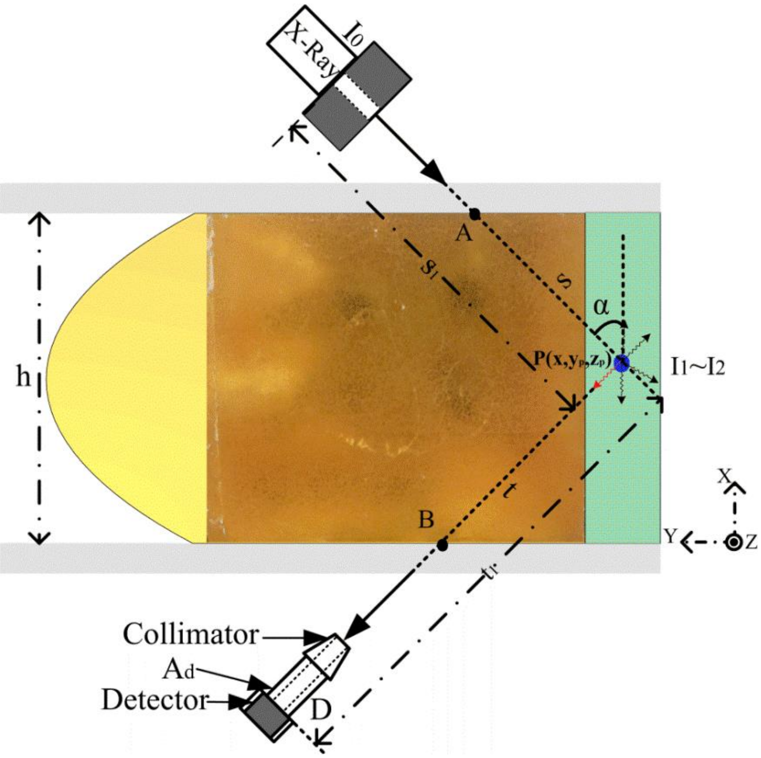

Figure 56. Schematic diagram of the attenuation analysis of both incident and isolated fluorescence X-ray.

Based on the geometrical relationship in Fig. 56, the AF can be defined and presented as

$$AF = exp[-\frac{\mu_p (h - x)}{cos\alpha} - \frac{\mu_p' x}{sin\alpha}] \tag{42}$$

Since AF is always smaller than 1 for this scenario, it is maximized so as to obtain maximum fluorescence intensity under the same excitation condition. Let the derivative ${dAF}/{d\alpha}$ be equal to 0; then the optimal incident angle for each excitation volumetric element is calculated as:

$$\alpha = arctan(\sqrt[3]{\frac{\mu_p' x}{\mu_p (h - x)}}), \quad 0 < x < h \tag{43}$$

It is impossible to achieve maximum fluorescence intensity for each excitation volumetric element because the optimal incident angle calculated by Eq. (43) varies with spatial coordinates. The line integral of AF (T_{AF}) is therefore computed to represent the total attenuations for each scanning line.

$$T_{AF} = \int_0^h exp[-\frac{\mu_p (h - x)}{cos\alpha} - \frac{\mu_p' x}{sin\alpha}]dx \tag{44}$$

The optimal incident angle can be roughly estimated by using the first two terms in Taylor series expansion of the exponential function to solve the integral problem:

$$\alpha_{optimal} = arctan(\sqrt[3]{\frac{\mu_p'}{\mu_p}}), \quad 0° < \alpha_{optimal} < 90° \tag{45}$$

Since the scan for the entire ROI can be considered as a repetition of the line scan process, the $\alpha_{optimal}$ can be also regarded as an overall optimal value. However, the accuracy of the derived result needs to be validated through numerical calculations to justify the approximation calculations.

6.2.4 Background removal and attenuation calibration

Still, gold $K_{\alpha 1}$ and $K_{\alpha 2}$ peaks at 68.80keV and 66.99keV are collected for subsequent analysis. Rather than the experimental method, this chapter uses a built-in function/algorithm (a.k.a., Peak Calculation) of AmpTek software (DppMCA, Amptek

Inc., Bedford, US) based on the Eq. (46) to extract the fluorescence counts (S) within each defined energy window.

$$S = G - \frac{B_l + B_r}{2n} N \tag{46}$$

Where G represents the gross area as the sum of counts under the chosen energy window; B_l and B_r are the neighboring bins used to calculate the background counts on the left and right sides of the defined energy window; n is the width of both background fields ($n = 6$ in this chapter) and N is the number of channels under each energy window.

In view of the homogeneous property of the designed phantom, the *a priori* knowledge based method is taken to calibrate the attenuations when X-ray beams travel through the phantom [21]. Defining the $CF = AF^{-1}$, the extracted fluorescence counts of gold K_α peaks can be effectively calibrated by multiplying by *CF*. The corrected value of fluorescence counts can be finally used to make a direct mapping of the ROI.

6.3 Results

6.3.1 Numerical calculations of the optimal incident angle

The estimated $\alpha_{optimal}$ can be determined as below using Eq. (45).

$$\alpha_{optimal} = \arctan(\sqrt[3]{\frac{0.184cm^{-1}}{0.163cm^{-1}}}) = 46.16° \tag{47}$$

Where $0.163\,cm^{-1}$ is the LAC (μ_p) of the gel phantom/BR12 at the mean energy range of 80.725keV-140keV and $0.184\,cm^{-1}$ is LAC ($\mu_p{}'$) of the gel phantom/BR12 at gold K_α energy [21, 131].

Instead of a continuous integral as in Eq. (43), discrete calculations under the condition of various intervals are performed. Three intervals (i.e. translational moving step of the phantom in X direction) of 1mm, 0.5mm and 0.1mm are selected, where 1mm is the interval applied in this study, and 0.5mm and 0.1mm represent the possible smaller intervals that may be used in the future. For each interval, the normalized fluorescence intensity of the scanning line (MN in Fig. 55) with respect to the incident angle, changing from 0 ° to 90 °, is demonstrated in Fig. 57.

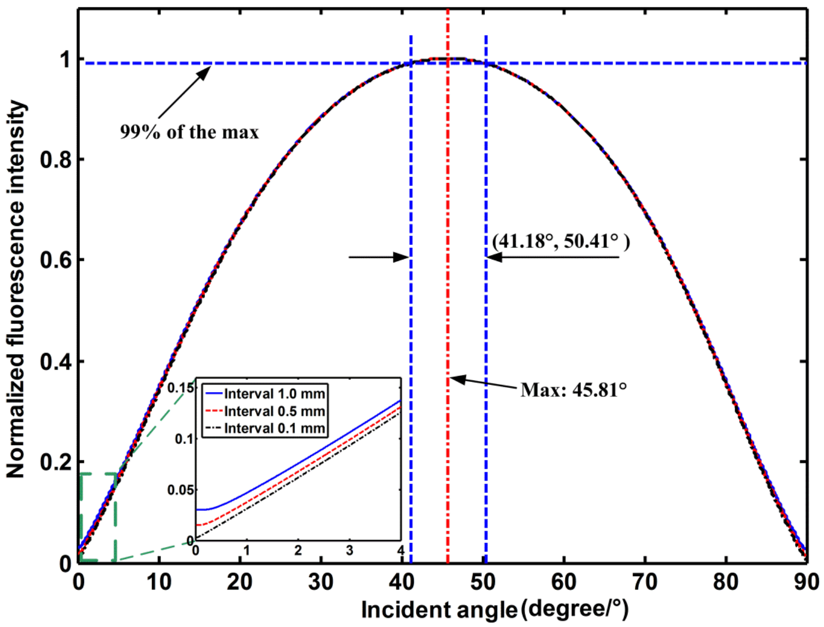

Figure 57. Normalized fluorescence intensity of the scanning line with respect to the incident angle changing from 0 ° to 90 °.

In Fig. 57, there is no obvious difference among three normalized curves with intervals varied from 0.1mm to 1mm except when the incident angle is close to 0 ° and 90 °. An optimal range from 41.18 ° to 50.41 ° of the incident angle is defined when the fluorescence intensity is decreased to 99% of its maximum (under 45.81 °). Since the estimated value (46.16 °) in Eq. (47) is well located within this optimal range and quite close to the calculated maximum (the relative error is around 0.76%), Eq. (45) can be regarded as a valid estimate.

6.3.2 Data analysis and mapping reconstruction

Based on the estimation and numerical calculation in Eq. (47) and Fig. 57, the optimal incident angle of 45.81° is adopted throughout the process of data acquisition. Three typical spectra acquired under this optimal angle are shown in Fig. 58. The two peaks at about 55 - 60keV are from water scattering and have similar amplitudes in position (2) and (3). Due to the slight divergence, the beam diameter at the detected area becomes expanded, compared to the diameter aperture of the beam collimator. Therefore, part of the scattered X-ray from water may be detected as well, as shown in the spectrum in position (1) [113]. No gold fluorescence peaks are obtained when there are no GNPs distributed at the excitation volumetric element. In contrast, quantifiable gold $K_{\alpha 1}$ and $K_{\alpha 2}$ peaks are observed when gold solutions are located and excited. It is also apparent that the gold fluorescence intensity is proportional to the concentration of the gold solution. The fluorescence peaks with lower energies (less than 20keV) are not used for quantitative analysis considering the limited penetrability through the breast-mimicking phantom.

For those spectra where gold $K_{\alpha 1}$ and $K_{\alpha 2}$ peaks exists, the function of peak calculation is utilized to automatically get the peak information. Five important parameters: centroid, FWHM, net area, uncertainty and net rate, can be determined simultaneously for each fluorescence peak. As an example, the calculated parameters for the typical spectra in Fig. 58 [position (2) and (3)] are listed in Table. 5.

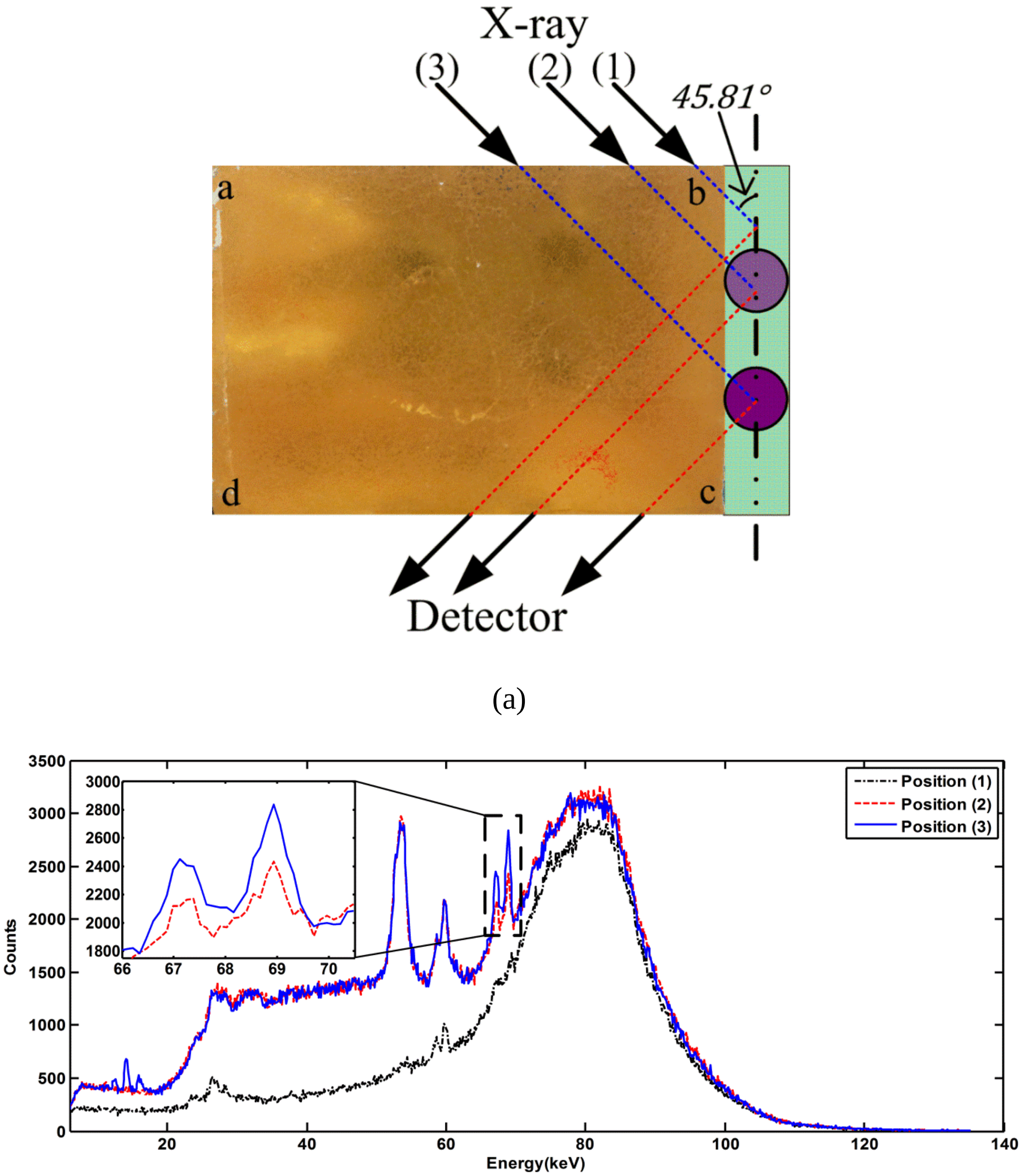

(a)

(b)

Figure 58. Three typical (a) excitation positions of (1) no gold solution, (2) 0.5% gold solution, (3) 1.0% gold solution (b) spectra with gold fluorescence peaks highlighted.

Table 5. The measured information of gold fluorescence peaks in typical spectra.

Peak information	Concentration 0.5%		Concentration 1.0%	
	$K_{\alpha 2}$	$K_{\alpha 1}$	$K_{\alpha 2}$	$K_{\alpha 1}$
Centroid (keV)	67.12	68.74	67.01	68.78
FWHM (keV)	0.601	0.678	0.742	0.705
Net Area (N)	1604	2277	3098	4327
Uncertainty (%)	12.96	8.61	7.20	5.11
Net Rate (%)	4.59	6.51	8.88	12.40

Among these parameters, net area is useful for reconstruction. Before calculating the reconstruction, the attenuation difference for each excitation volumetric element is calibrated. The calibration curve of each scanning line in the X direction is computed according to the definition of CF and is shown in Fig. 59. Then, through multiplying by the corresponding CF for each excitation volumetric element, all corrected fluorescence counts are available for mapping reconstruction. The scan results for line MN without/with the attenuation calibration are compared in Fig. 60. In order to reduce the stochastic error during the process of data acquisition, the ratio of total fluorescence counts representing 1.0% (X=5mm - 21mm) and 0.5% (X=26mm - 41mm) gold solution area, rather than only using the peak value at X=14mm and X=34mm, is calculated. The calculated ratio is 2.31 without and 2.05 with the calibration.

Through repeating the line scanning process with $\Delta z = \pm 1mm$ in Z direction, the reconstruction results for the middle plane (Y=5mm) in the ROI are shown in Fig. 61, matching well with the known spatial distribution and different GNP concentrations indicated in Fig. 53 (b) (the ratio of average counts for 1.0% and 0.5% gold solutions: 2.03). Similarly, the 3D reconstruction of the ROI can be achieved by repeating the 2D mapping process with $\Delta y = \pm 1mm$ in Y direction.

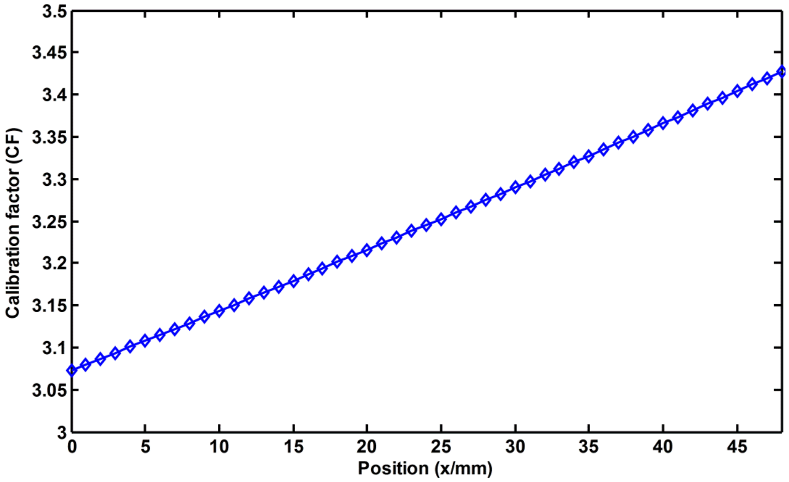

Figure 59. Calibration curve for each scanning line in X direction for X=0 to X=h (h=48mm).

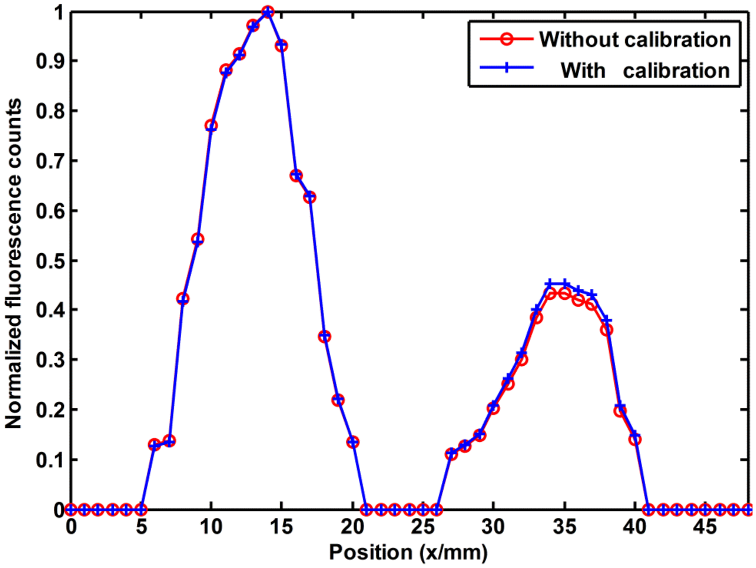

Figure 60. Scan results for line MN without/with attenuation calibration. The ratio of total fluorescence counts representing 1.0% and 0.5% gold solution area is 2.31 without and 2.05 with the calibration.

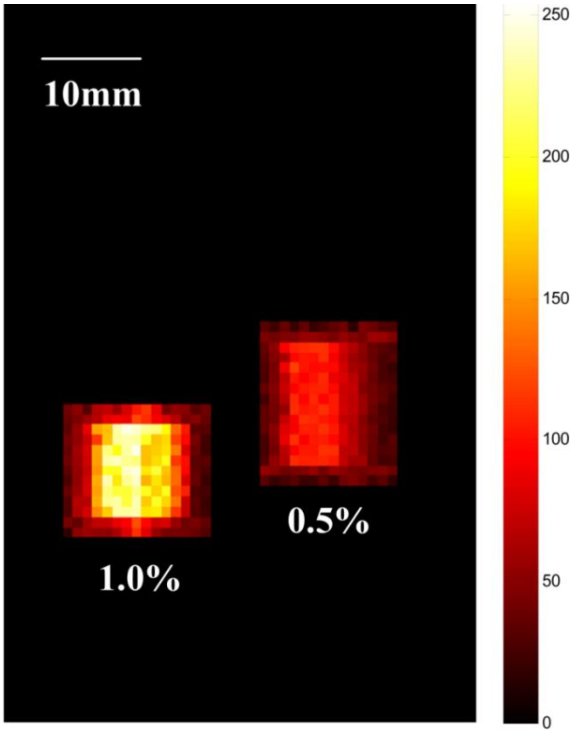

Figure 61. 2D mapping reconstruction of the middle plane (Y=5mm) in the ROI matches well the spatial distribution and different GNP concentrations shown in Fig. 33 (b).

6.4 Discussion

This chapter presents a unique physical model for applying the XFM technique to detect breast cancer located in the posterior aspect of the breast. Due to the different imaging geometry and signal acquisition method, this technology has potential to provide the effectively complementary or supplementary diagnostic information to conventional mammography. Though the results are encouraging, there still remain several aspects to be considered in how to evaluate and improve the implementation of XFM to breast cancer detection.

Considering clinical imaging requirements such as breast compression and positioning for standard mammography screening views, a feasible scanning trajectory was determined, upon which further experiments can be carried out. Though the scanning trajectory was tested under the condition of using pencil-beam X-ray and a single spectrometer, it is also suitable when fan-beam X-ray and a 1D/2D spectrometer array are employed. This would improve the beam geometry and drastically reduce the total scanning time. For example, the scanning time for the middle plane in the ROI could be immediately reduced by a factor of 70 (291.67h to 4.17h) when repeating the experiment with a fan-beam X-ray and 1D spectrometer array with 70 sensitive elements [91]. In addition, the mapping efficiency could be further improved by replacing the currently used low power (~70W) source with a high power X-ray source [145]. However, these modifications require considerations of potentially higher cost and hardware complexity, and increased influence of Compton scattering from water/background on detecting fluorescent signals. It is also worth noting that the translation approach performed on the phantom for the data acquisition could not be used on the human breast in clinical practice. Thus, synchronous control and translation of X-ray source and spectrometer need to be dedicatedly designed and justified.

Another important issue regarding the feasibility of applying the XFM technique to clinical use is whether the methods of determining the optimal incident angle and the CF are still valid, considering the inhomogeneous property of the LACs and distributions of different components in a realistic breast. In addition, though the detection sensitivity/specificity and the radiation dose of the current imaging modality are not studied and determined, these crucial issues need to be theoretically and experimentally studied in future investigations and then compared with current imaging modalities such as mammography and breast CT [146, 147]. Besides the optimal incident angle analyzed in this chapter, other strategies such as optimizing collimators and designing proper filtration should be carefully considered to achieve high detection sensitivity and acceptable radiation dose to satisfy the clinical requirements.

Although other imaging modalities, such as ultrasound (US), magnetic resonance imaging (MRI) and CT, have been studied to assess the presence of chest wall invasion by tumor with limited success [137, 139, 148], the XRF based technique, XFM, offers a different imaging approach with additional advantages including the functional imaging with the use of the molecular imaging probes based on GNPs and the specific scanning trajectory geometry to evaluate the breast tumors close to the chest wall musculature.

6.5 Chapter summary

This chapter successfully demonstrates, for the first time to our knowledge, the proof of concept of applying XFM to detect breast tumors located close to the chest wall musculature using a breast-mimicking phantom with embedded GNPs, as an effectively adjunctive tool to the screening mammography.

Chapter 7: MTF determination of XFM imaging system

7.1 Chapter introduction

Improving and optimizing the performance of the XRF based imaging techniques and systems have been investigated theoretically and experimentally. Significant research topics include, but not limited to, employing fan-beam or cone-beam excitation X-ray, using hypothetical 1D or 2D detectors, determining optimal system geometry, designing superior collimator systems, deciding proper filtration and selecting appropriate fluorescence peaks, and so on [68, 91, 92, 96, 110, 149]. A great deal of studies such as determining the detectability and analyzing the signal-to-noise ratio (SNR) have also been conducted to quantitatively and effectively evaluate the system optimization and improvement [96, 111]. Even so, the imaging performance of the XRF based imaging systems have not been fully characterized yet, e.g. the spatial resolution, a major evaluating index. In this chapter, therefore, the spatial resolution in XFM system is thoroughly analyzed and evaluated through measuring the MTF in two perpendicular directions.

The measurement of MTF has been widely accepted for characterizing and quantifying the imaging performance of various imaging modalities [22]. The calculation of MTF can be determined through normalizing the absolute value of the Fourier transform of the point spread function (PSF) or line spread function (LSF). Since the point-shape or line-shape objects are difficult to be prepared and fabricated using GNPs or other contrast media, an alternative is putting the contrast media into a standard container in cuboid shape to form sharp edges. With the sharp edges, the edge spread function (ESF) can be acquired and then differentiated to obtain the LSF.

7.2 Materials and methods

7.2.1 System configuration and principle

The configuration of a typical XFM system is demonstrated in Fig. 62. A saline solution containing GNP at 1.0% mass percentage poured into a standard container (10mm×10mm×45mm) in cuboid shape. By means of doing so, sharp edges in horizontal and vertical directions are easily formed. Other than that, the experimental configuration of XFM system is identical as introduced in previous chapters.

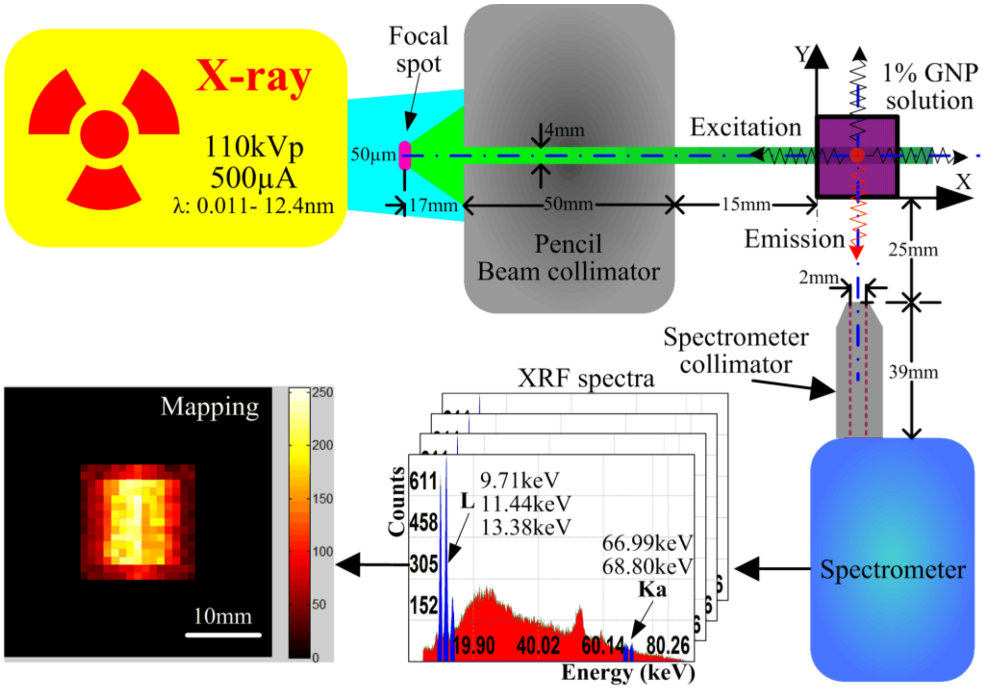

Figure 62. Schematic of the XFM system including the X-ray source, beam collimator, prepared GNP solution (1% mass percentage), spectrometer collimator and spectrometer (not drawn to scale).

The prepared GNP solution within the standard container is capable of translating along the perpendicular directions (X and Y) while the X-ray source and the spectrometer are stationary in this typical laboratory setting. For each scanned position, the fluorescence peaks are isolated from the background and the attenuation calibration is performed to acquire the accurate fluorescence counts under each fluorescence peak, so that a direct mapping reconstruction could be accomplished. The detailed description of a 3D XFM system can be found in Chapter 5.

7.2.2 Data acquisition and processing for ESF

The GNP solution is translated horizontally (X direction) and vertically (Y direction), in different steps of 0.1mm - 0.6mm, to acquire the ESF data (spectra) within the ranges of -5.0mm < X < 5.0mm and -5.0mm < Y < 5.0mm, respectively. The scanning ranges are determined to include not only the slightly gradual transition region, but also enough data for flat high and low levels. The subtle imaging steps of 0.1mm - 0.6mm resulting in sufficient oversampling data across the area to be detected are chosen to synthesize the presampled ESFs and avoid the aliasing phenomenon. As shown in Fig. 63, the data acquisition is performed in two directions, where Y is fixed as 4.0mm when acquiring the data for ESF in X-direction while X is 5.0mm for ESF acquisition in Y-direction. The data acquisition time for each position is 120s and it is completely paused during the translation of the GNP solution to next position by one imaging step along either direction.

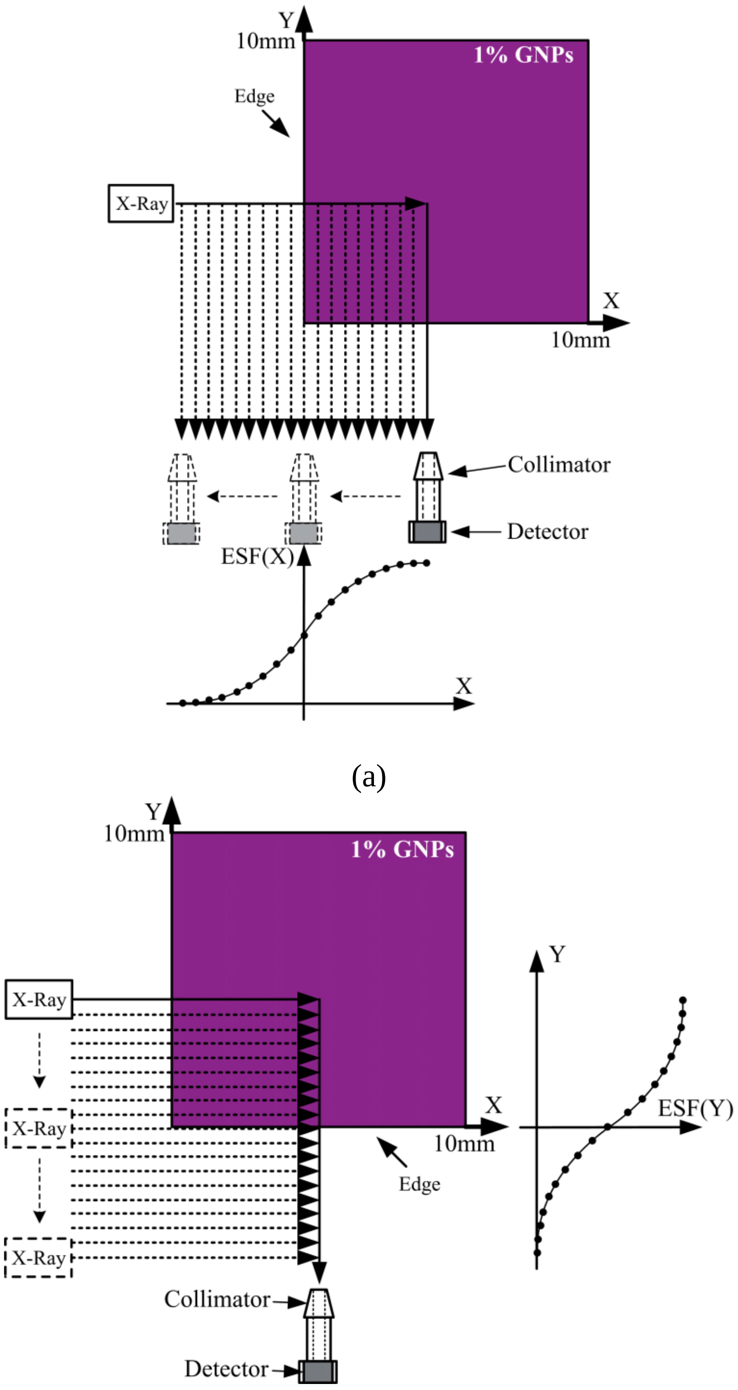

(a)

(b)

Figure 63. Data acquisition for ESF in horizontal (X) and vertical (Y) directions; the data acquisition time for each position is 120s. (a) -5.0mm < X < 5.0mm, Y=4.0mm; (b) X=5.0mm, -5.0mm < Y < 5.0mm.

For each scanned position, the data represented as a full spectrum is acquired, consisting of several fluorescence peaks emitted from GNPs and the background scattered by water. An example of spectrum acquired at the position of (X=2.0mm, Y=4.0mm) is shown in Fig. 64, with the purpose of demonstrating the process of background estimation (peak isolation) and fluorescence counts collection.

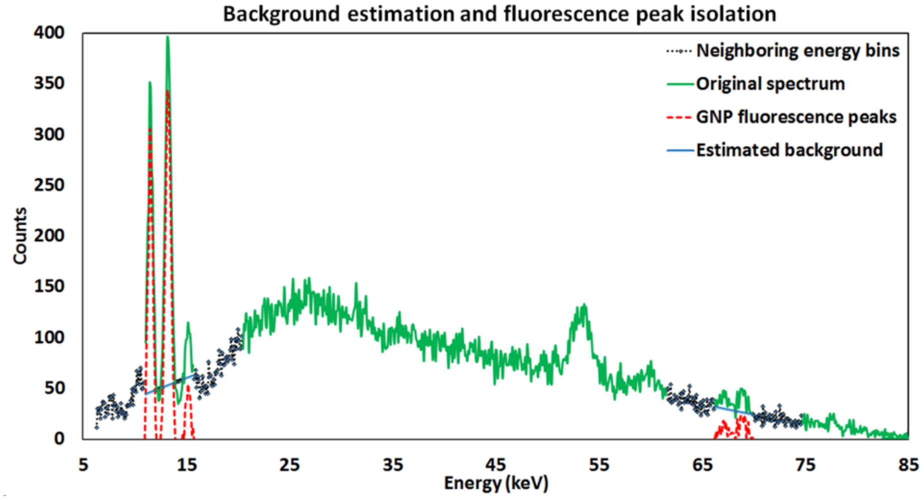

Figure 64. A typical spectrum (X=2.0mm, Y=4.0mm) demonstrates the process of background estimation and fluorescence counts collection.

In Fig. 64, five obvious fluorescence peaks from GNPs are observed: L_α at 9.71keV, L_β at 11.44keV, L_γ at 13.38keV, $K_{\alpha 2}$ at 66.99keV and $K_{\alpha 1}$ at 68.80keV. These fluorescence peaks are superimposed on the scattered photons from water and the net counts under these GNP fluorescence peaks must be extracted to construct the ESF. The linear interpolation method is applied for the background estimation [150]. The energy windows for the fluorescence peaks on the L-shell (L_α , L_β and L_γ) are defined as 9.15-10.27keV, 10.88-12.00keV, and 12.82-13.94keV while the correspondingly neighboring bins are chosen as 8.54-9.15keV, 10.27-10.88keV, 12.21-12.82, and 13.94-

14.55keV. The energy windows and neighboring bins for the K-shell fluorescence peaks ($K_{\alpha 2}$ and $K_{\alpha 1}$) are set based on the results in Chapter 4. The net number of counts (S_k), the measuring uncertainty (U_k) and signal-to-background ratio (SBR_k) of these fluorescence peaks within the optimal energy windows are calculated using Eq. (13)-(15).

Followed with the peak isolation, the data for constructing the ESFs from each fluorescence peak are acquired respectively, with respect to the scanning position in X- and Y- directions. To ensure the accuracy, two direct strategies are particularly employed. First, the fluorescence peak of L_α at 9.71keV is out of consideration because of the possible overlapping with the tungsten L_β at 9.67keV. Second, two fluorescence peaks on K-shell, $K_{\alpha 2}$ and $K_{\alpha 1}$ are combined as one peak K_α in an effort to reduce the measuring uncertainty. Using the data shown in Fig. 64, as the typical example, the measuring uncertainties are computed as 1.79, 6.46 and 10.69, and the SBR are calculated as 3.989, 0.476 and 0.342 for L_β, L_γ and K_α fluorescence peaks.

Then, *a priori* knowledge based method is utilized to calibrate the attenuations when the primary pencil-beam X-ray or detected fluorescence signals travel through the homogeneous GNP solution in X/Y directions, as described in previous chapter [21].

$$SC_{kX} = \begin{cases} S_{kX}, & -5 \le X \le 0mm \\ S_{kX} e^{X\mu_{kX}}, & 0 \le X \le 5mm \end{cases} \tag{48}$$

$$SC_{kY} = \begin{cases} S_{kY}, & -5 \le Y \le 0mm \\ S_{kY} e^{Y\mu_{kY}}, & 0 \le Y \le 5mm \end{cases} \tag{49}$$

Where S_{kX} / S_{kY} and SC_{kX} / SC_{kY} represent the net number of counts acquired before and after the attenuation corrections in X/Y direction, under each fluorescence peak k. The calibration factors are determined as $e^{\mu_{kX}}$ and $e^{\mu_{kY}}$, respectively. μ_{kX} is the integrated LAC of GNP solution at the energy range of 14.353keV - 110keV for the gold L_{β} and L_{γ}, and that at the energy range of 80.725keV - 110keV for gold K_{α}. μ_{kY} is the LAC of GNP solution at the fluorescence energies of gold L_{β}, L_{γ} and K_{α}. For simplicity, both of the attenuation corrections are only performed in the positive directions (0 - 5mm).

7.2.3 Calculation and derivation of the MTF

With regard to reducing the stochastic error resulting from the noise on MTF estimates, a straightforward way would be to calculate the average of the corrected ESF data acquired using the number of counts under L_{β}, L_{γ} and K_{α} fluorescence peaks [151]. However, the magnitudes of counts are generally different due to the SBR difference for each fluorescence peak, as shown in Fig. 64. Thus, the oversampled ESF data constructed from each fluorescence peak are first processed by normalization, in an effort to facilitate the remaining data processing. These normalized ESFs are designated as $ESF_{L_{\beta}}(X)$, $ESF_{L_{\gamma}}(X)$ and $ESF_{K_{\alpha}}(X)$ in X-direction while $ESF_{L_{\beta}}(Y)$, $ESF_{L_{\gamma}}(Y)$ and $ESF_{K_{\alpha}}(Y)$ in Y-direction. Then, $ESF(X)$ and $ESF(Y)$ are determined as the averages of these normalized ESFs using the following equations. Thereafter, only the computations in X-direction are illustrated.

$$ESF(X) = \frac{1}{3}[ESF_{L\beta}(X) + ESF_{L\gamma}(X) + ESF_{K\alpha}(X)] \tag{50}$$

In order to further minimize the possible noise, a rational function (F_r) is applied to obtain the fitted ESFs, $ESF_f(X)$ and $ESF_f(Y)$. The coefficients p_1, p_2, p_3, q_1, q_2, q_3 and q_4 are determined with 95% confidence bounds.

$$F_r(X) = \frac{p_1 X^2 + p_2 X + p_3}{X^4 + q_1 X^3 + q_2 X^2 + q_3 X + q_4} \tag{51}$$

Then, the LSFs, $LSF(X)$ and $LSF(Y)$, are computed by differentiating the fitted $ESF_f(X)$ and $ESF_f(Y)$ with respect to the distances in X- and Y-direction, using Eq. (52), where ΔX is the moving step of the GNP object.

$$LSF(X) = \frac{ESF_f(X + \Delta X) - ESF_f(X)}{\Delta X} \tag{52}$$

After cutting off the tail data below 1% of the peak value, $LSF(X)$ and $LSF(Y)$ are fitted by a Gaussian function (F_G) and the extrapolation are performed on both tails, which makes the overall MTF curve better behaved through forcing a smoothing transition of the LSFs to zero [152].

$$F_G(X) = a_1 e^{(-(X-b_1)/c_1)^2} \tag{53}$$

Where the parameters a_1, b_1 and c_1 are the amplitude, the position of the center of the peak, and the spread of the curve, respectively. The LSFs fitted by the Gaussian function are represented as $LSF_f(X)$ and $LSF_f(Y)$. Two important scalar figure-of-merits, the FWHM and full-width-at-one-tenth-maximum (FWTM) of the fitted LSFs are utilized to characterize and compare the imaging performance of XFM system in both scanning directions.

Finally, the MTFs, $MTF(f_X)$ and $MTF(f_Y)$, are obtained from the fast Fourier transform (FFT) of the $LSF_f(X)$ and $LSF_f(Y)$, and normalization to unity at zero spatial frequency.

$$MTF(f_X) = \frac{FFT\{LSF_f(X)\}}{FFT\{LSF_f(X)\}|\ f_X = 0} \tag{54}$$

7.2.4 Analysis of factors influencing the MTF determinations

Though the moving steps of Δx and Δy in horizontal (X-) and vertical (Y-) directions determine the pixel pitch in the resultant image of mapping, it is usually not the limiting factors in MTF determinations. Also, the influence of diffraction effect is minimal due to the very short wavelength (0.011 - 12.4nm corresponding to the energy of 0.1 - 110keV) of the X-ray we used in this chapter, compared with the diameters of the collimators in mm level. So the analysis of factors influencing the MTF determinations using the geometric optics becomes feasible. The influencing factors in XFM system can be discussed into two separate parts, the excitation path and the emission path. As described in the system configuration, it is the dimensions of the beam collimator and the spectrometer collimator that significantly influence the MTF measurements. Besides that, the relative positions among X-ray source, collimators, GNP object, spectrometer as well as the sensitive element of the detector also affect the MTF measurements, which is quite similar as the analysis of the Anger gamma scintillation camera in planar nuclear imaging. The details are interpreted below in Fig. 65 and 66.

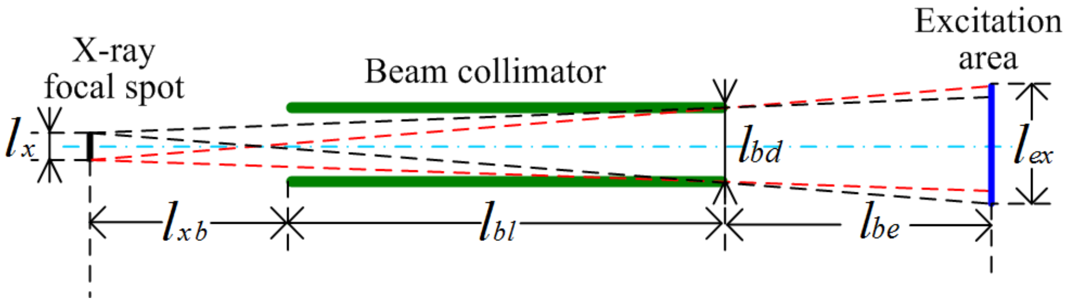

Figure 65. Influencing factors on the excitation path in XFM system.

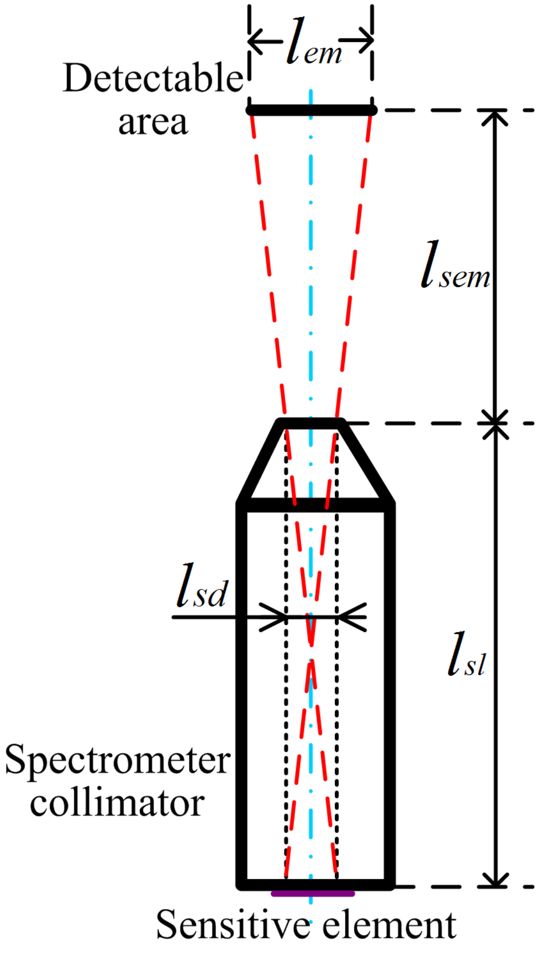

Figure 66. Influencing factors on the emission path in XFM system.

In Fig. 65, the primary X-ray generated from the focal spot is collimated through the beam collimator, producing the X-ray pencil-beam. Due to the slight divergence, the beam diameter at the location (excitation area) of the GNP solution becomes expanded, compared to the diameter aperture of the beam collimator. Similarly, the fluorescent/scattered X-rays emitted from the GNPs/water are restricted by the spectrometer collimator before reaching the sensitive element of the detector. The detectable area at the GNP solution for each position, however, is larger than the collimator aperture because of the detecting geometry as shown in Fig. 66.

According to the geometrical relationships, the beam diameter of excitation area and the detectable diameter of emission area can be expressed in Eq. (55) and (56). Using the system parameters specified in Table. 6, l_{ex} and l_{em} are calculated as 4.907mm and 4.564mm. Thus, the MTF curve would be expected with a better performance in the scanning along X-direction.

$$l_{ex} = l_{bd} + \frac{l_{be}(l_{bd} + l_{x})}{l_{xb} + l_{bl}} \tag{55}$$

$$l_{em} = l_{sd}(1 + \frac{2l_{sem}}{l_{sl}}) \tag{56}$$

As described in Eq. (55) and (56), the dimensions of the collimators (l_{bl}, l_{bd}, l_{sl} and l_{sd}) and the collimator-to-object distances (l_{be} and l_{sem}) play pivotal roles in determining the MTF in the XFM system. The imaging performance could be potentially improved through reducing the diameters and increasing the thicknesses of the collimators, and minimizing the collimator-to-object distances in both of the excitation and emission paths.

Table 6. System parameters specified in this XFM configuration.

Parameters	Definition	Value
l_x	X-ray focal spot size	50 μm
l_{xb}	Distance from X-ray focal spot to beam collimator	17mm
l_{bl}	Length of beam collimator	50mm
l_{bd}	Diameter of beam collimator	4mm
l_{be}	Distance from beam collimator to GNP solution	15mm
l_{ex}	Beam diameter of excitation area	Eq. (43)
l_{sl}	Length of spectrometer collimator	39mm
l_{sd}	Diameter of spectrometer collimator	2mm
l_{sem}	Distance from spectrometer collimator to GNP solution	25mm
l_{em}	Detectable diameter of emission area	Eq. (44)

7.3 Results

7.3.1 ESF and curve fitting

After attenuation corrections and normalizations, the averaged ESF data from three fluorescence peaks are fitted by a rational function, as shown in Fig. 67, in which the moving steps are selected as Δx =0.1mm and Δy =0.1mm. For each fluorescence peak from GNPs, L_β, L_γ and K_α, the relative deviation between the original ESF data and fitted ESF curve are interpreted in Fig. 68.

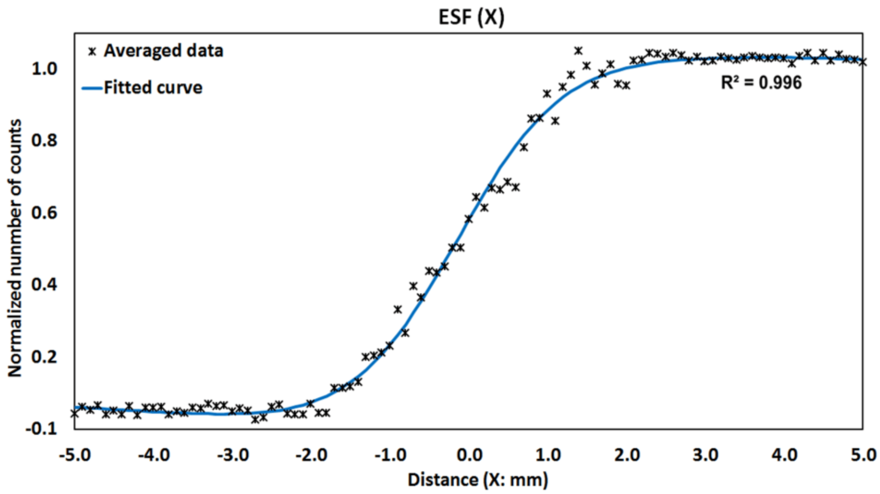

(a)

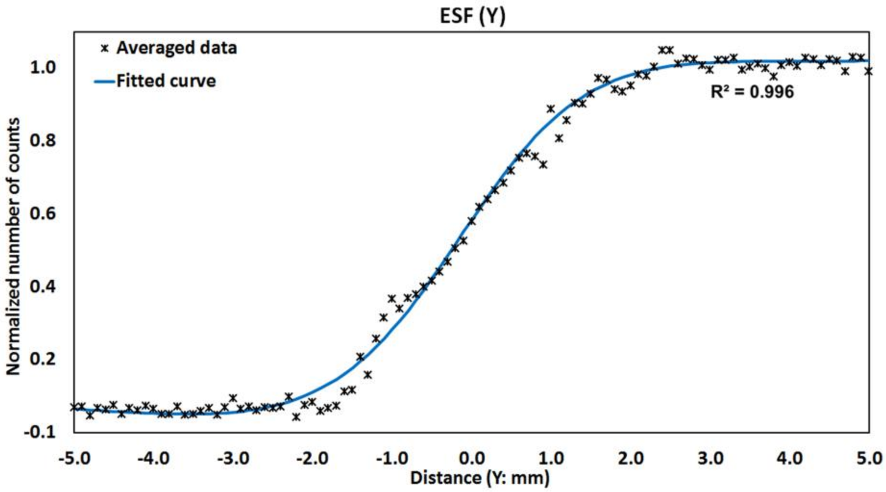

(b)

Figure 67. The averaged ESF data from three fluorescence peaks and the correspondingly fitted curve using the Gaussian function in (a) X- and (b) Y-direction.

It should be noted that the overall deviations are proportional to the measuring uncertainty and inversely proportional to the SBR, respectively. Also, the deviation values are significantly increased as the spectrometer or primary X-ray moves away from the GNP solution during the process of acquiring the ESF data.

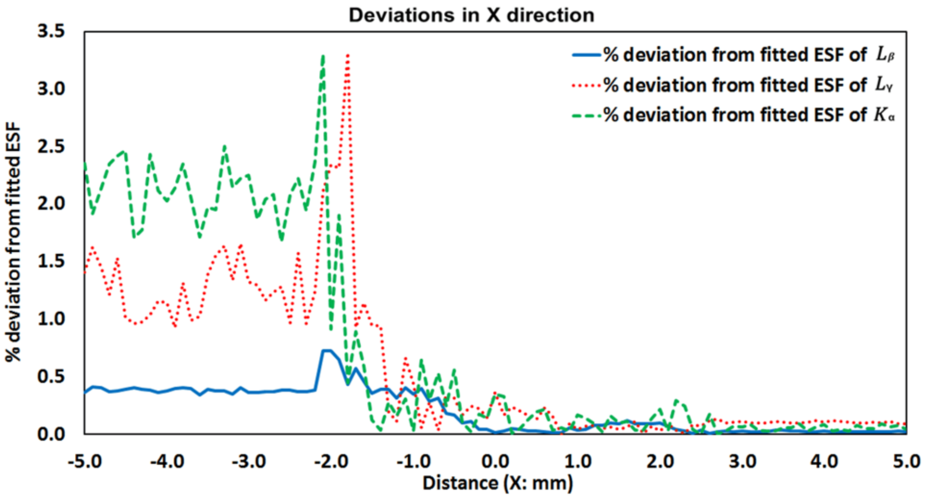

(a)

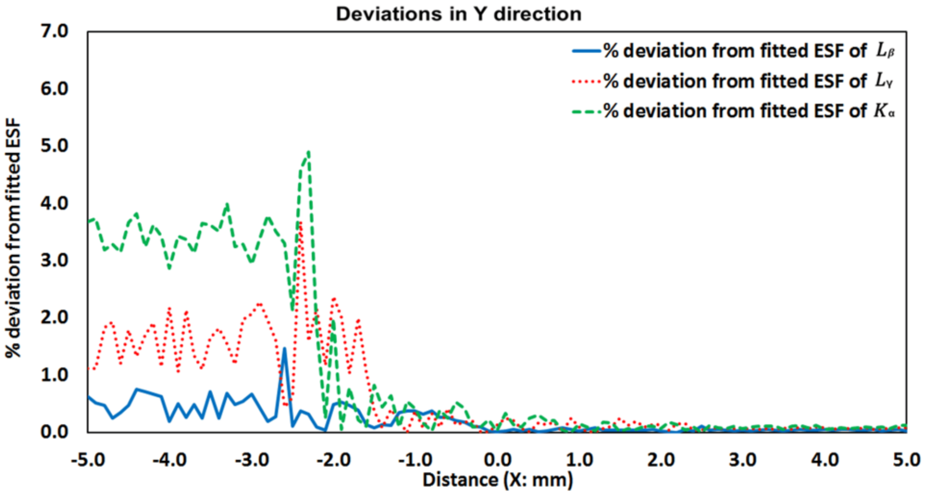

(b)

Figure 68. Relative deviations between each originally corrected ESF data and the fitted ESF curve in (a) X- and (b) Y- direction, showing an increasing tendency of deviation values as the primary X-ray or spectrometer moves away from the GNP solution.

7.3.2 MTF determinations

The LSFs, $LSF(X)$ and $LSF(Y)$, computed by differentiating the Gaussian-fitted ESFs in X- and Y-directions with Δx =0.1mm and Δy =0.1mm are shown in Fig. 69. The Gaussian function is applied to fit and expend the LSFs up to (-10mm, 10mm). The

FWHMs of LSFs are determined as 2.50mm and 2.60mm, while FWTMs are 4.60mm and 4.70mm for $LSF(X)$ and $LSF(Y)$.

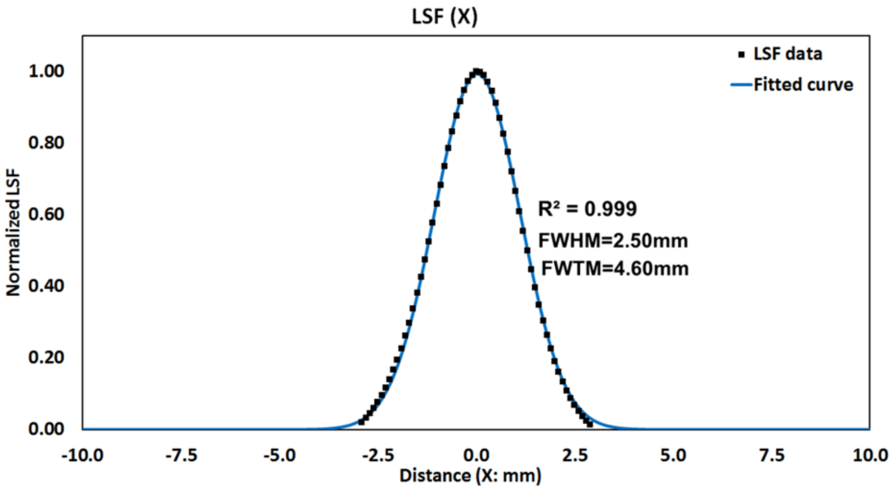

(a)

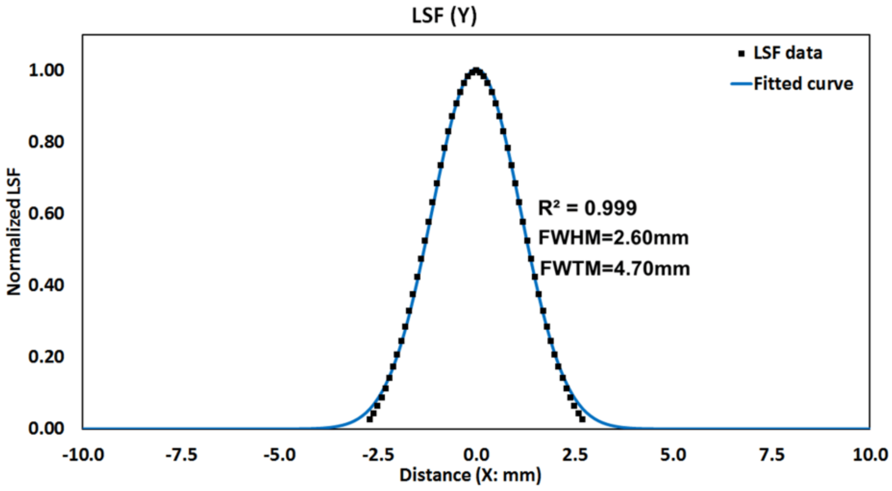

(b)

Figure 69. The LSFs computed by differentiating the fitted ESFs are fitted and extended up to (-10mm, 10mm) by Gaussian function in (a) X- and (b) Y-direction.

The MTFs calculated through normalizing the absolute value of the Fourier transform of the Gaussian-fitted LSFs are shown and compared in Fig. 70. Both of the

FWHMs and FWTMs of LSFs and the computed MTFs indicate a better imaging performance regarding the spatial resolution in X-direction due to less divergence of X-ray. The results qualitatively coincide with the theoretical analysis.

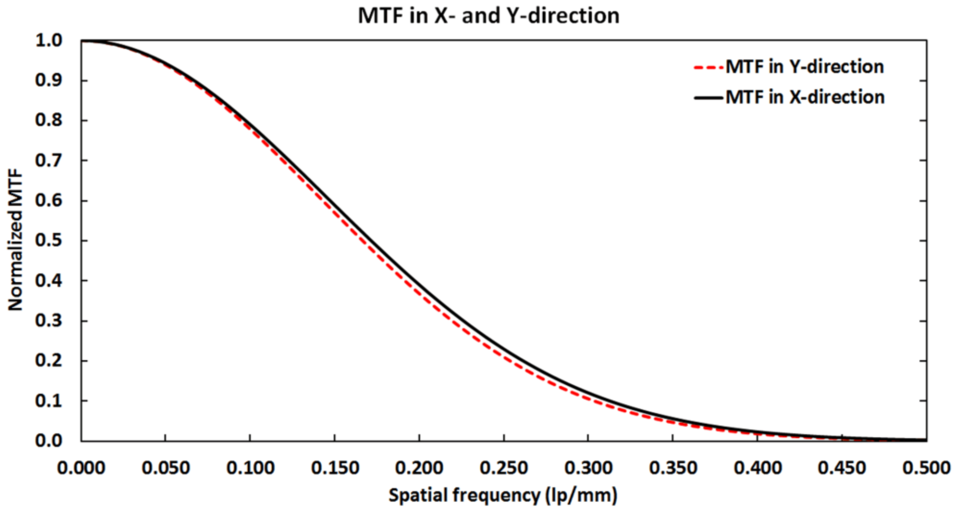

Figure 70. Measured MTFs in X- and Y- directions with moving step of 0.1mm.

In order to prove that the real resolving powers are limited by the dimensions of collimators and collimator-to-object distances in excitation and emission paths rather than the moving steps, the MTFs measured under the condition of different moving steps from 0.2mm to 0.6mm in both X- and Y- directions are demonstrated in Fig. 71. As expected from the theoretical analysis, it is shown that the measured MTFs are not noticeably affected by the moving steps of the GNP object (pixel pitches in reconstructed image).

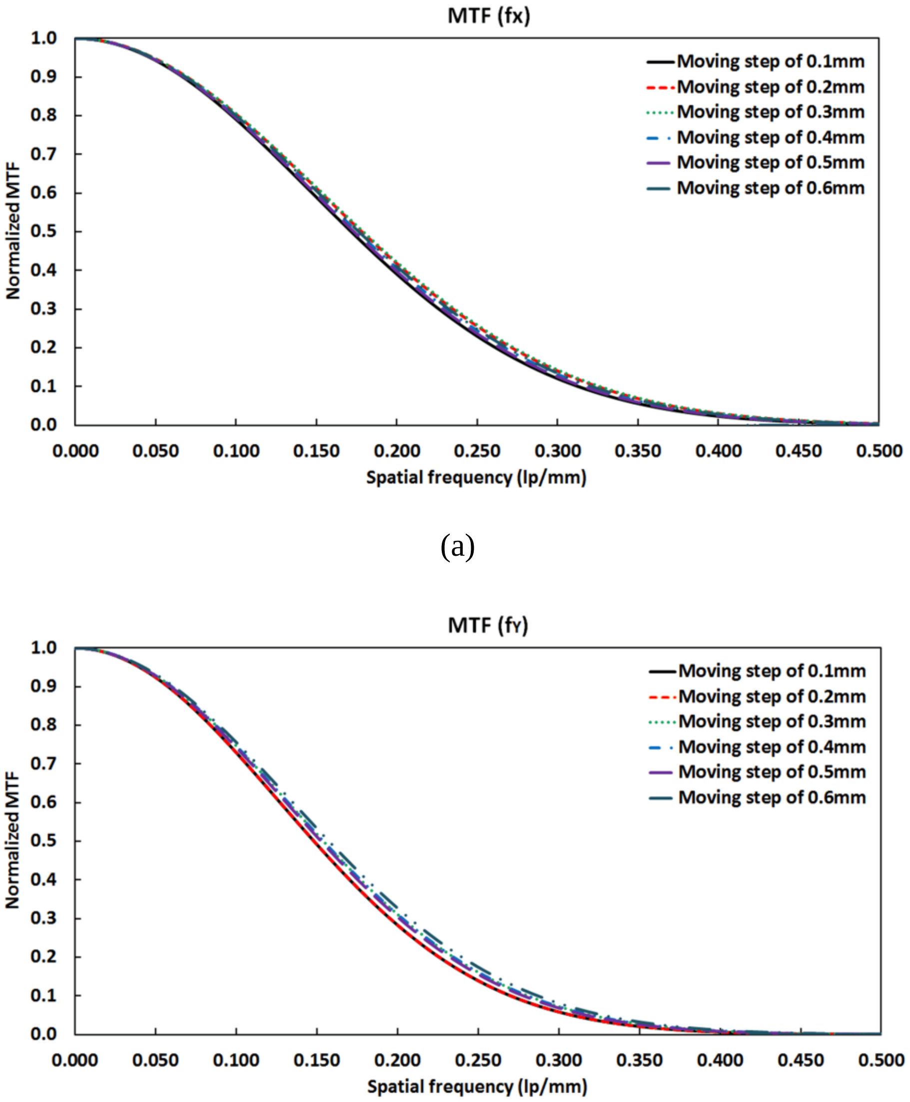

(a)

(b)

Figure 71. MTFs measured in X- and Y- directions with moving steps from 0.1mm - 0.6mm; only slight derivations are observed in each set of MTFs.

7.3.3 Influence of collimator-to-object distance on MTF measurements

An important factor limiting the spatial resolution is the collimator-to-object distances in either direction. As analyzed and expected in section 7.2.4, the MTFs shown in Fig. 72 are degraded with increased collimator-to-object distances in either direction. Therefore, great efforts should be made to minimize these distances in XFM system for a better imaging performance [22, 153].

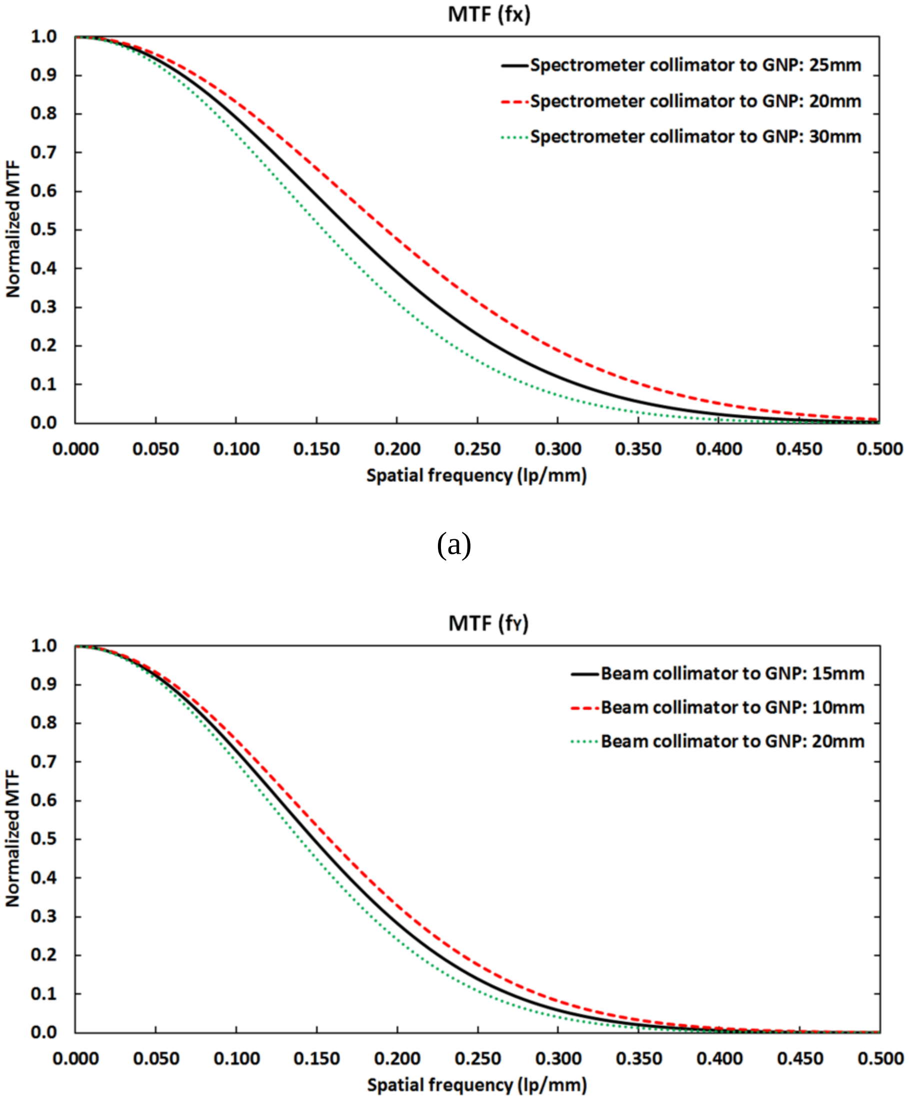

(a)

(b)

Figure 72. MTF measured with collimator-to-object distances of (a) 20mm, 25mm and 30mm in the emission path (b) 10mm, 15mm and 20mm in the excitation path.

7.4 Discussion

With a standard container in cuboid shape, sharp edges made by GNPs are formed and imaged to acquire the ESF data, based on which a method is proposed to determine the MTF in XFM system.

As in the derivations of Eq. (55) and (56), the dimensions of the collimators play pivotal roles in determining the MTF in XFM system. The spatial resolution could be potentially improved as the diameters of the collimators are reduced while the thicknesses are increased. However, it must be noted that these modifications of the collimators may lead to undesired efficiency reduction [22]. Thus, the diameters of collimators after the modifications should remain in mm level and the consideration of diffraction effect on MTF determination is not necessary. The experimental investigations regarding the influences of collimators dimensions on the MTF determinations are not performed in this chapter due to the relatively low power X-ray source (~55 W) and the design limitations of collimators. However, it would be useful and meaningful to conduct the experimental study in the future, making a full understanding how the dimensions of the collimators could influence the MTF determinations.

Another aspect that is not considered but may affect the MTF determination is the concentration of the GNP solutions under investigation. For the disease such as breast cancer at an early stage, the amount of GNP accumulations in tumors might be less than the concentration of 1% mass percentage [146, 147]. Thus, it would be a great challenge for characterizing the system performance because the measuring uncertainty and noise level for each fluorescence peak would be significantly increased with lower

GNP concentrations. That is the reason why the GNP solution with high contrast is utilized, in an effort to promise precise MTF measurements.

Even for the GNP solution with given concentration, the characteristics behave differently for different fluorescence peaks, such as SBR and measuring uncertainty. The ESF data acquired from the fluorescence peaks with high SBR may have better performance and accuracy because of the relatively lower uncertainty and noise level. However, those fluorescence peaks, in general, are restricted by low energy level and low penetrability through phantom/tissue, thus significantly limiting their usages in biomedical applications [21]. In contrast, the fluorescence peaks with high energy level such as K_α are much more popularly used in theoretical analysis and experimental studies [21, 68, 91, 92, 94, 110]. This is another important reason, besides reducing the noise, why the averaged ESF data combining all three fluorescence peaks from GNP with various SBRs and measuring uncertainties is determined and utilized for MTF estimates. It is noteworthy that the selection of the fluorescence peaks for MTF determinations may be subject to change in practically biomedical applications.

In this chapter, the MTFs are measured with GNP solution placed in air, so that the scatter and absorption within phantom/tissue are not considered. If the GNP solution is inserted into the phantom/tissue, on the contrary, two significant issues would directly influence the measurements of the MTF. First, the fluorescence peaks from GNP with lower energies and penetrability (e.g., L_α, L_β and L_γ) may be attenuated or even totally disappeared, depending upon the thickness and attenuation coefficients of the surroundings. Under such condition, only the fluorescence peaks with high energies (e.g., $K_{\alpha 2}$ and $K_{\alpha 1}$) can be used. Second, some photons would interact within the phantom/tissue and be scattered before escaping out of the phantom/tissue, causing a loss of SBR and adding unwanted statistical noise for evaluating the system performance. In addition, the method for attenuation calibration of fluorescence signals needs to be adjusted since the surroundings may have inhomogeneous property with respect to the LACs.

7.5 Chapter summary

In conclusion, this chapter presents a method for characterizing the resolving capability of an XFM imaging system using GNPs. Specifically, the method can be used to determine MTFs of an XFM system in two perpendicular directions. The influences of the GNP moving steps, collimator-to-object distances and other factors on MTF measurements are theoretically analyzed and experimentally verified. With modified imaging trajectories, this practical technique could be translated to measure the resolving power of other XRF based imaging systems.

Chapter 8: X-ray spectral measurement in micro-CT system

8.1 Chapter introduction

As described in Chapter 2 that those regular alignment methods specifically proposed for general X-ray imaging systems cannot be directly applicable or transferrable to a rotating gantry based micro-CT system, because this type of micro-CT system doesn’t provide the possibility to change the scanner geometry easily, meaning that normally the SDD is completely fixed and extremely limited when compared to a micro-CT prototype system [108]. In addition, the X-rays backscattered inside the gantry are not negligible due to the short SDD. Therefore, it is necessary to develop a specific alignment method for the X-ray spectral measurement in rotating gantry based micro-CT systems without introducing additional backscatters.

In recent years, 3D printing technology has been widely used in various applications with very high efficiency and accuracy [154]. In this chapter, supporting structures including a stand and a cover are manufactured using a 3D printer to facilitate the spectrometer system placement inside the gantry and to assist the alignment procedure. The spectra acquired under precise alignment and slight misalignment conditions are compared qualitatively and quantitatively.

8.2 Description of micro-CT scanner and spectrometer system

The micro-CT scanner (Quantum FX, Perkin Elmer, Waltham, MA, USA) utilized in this study mainly consists of a polychromatic X-ray source (target: W) and a flat panel X-ray imaging detector. The source and detector are mounted on the opposite sides of a rotating gantry with a fixed SDD of 265mm. The nominal voltage and current ranges of the X-ray source are 30 to 90kVp and 20 to 200 μA, respectively. Besides the CT scan mode that develops a tomographic image, a live mode lasting up to 150 seconds is available to view the subjects in real time with/without rotating the gantry, providing the possibility of achieving spectral alignment and measurement.

The same spectrometer system is utilized in this chapter. In order to acquire an acceptable photon rate level to prevent spectral pile-up distortion, the sensitive element of the detector is covered by a specific collimation set (Collimation Kit, Amptek, Bedford, MA, USA) including three tungsten pinholes with small diameters and 2mm in thickness and a brass spacer (36 mm in length and 3000 μm in diameter) separating them. The detailed schematic of the collimation set is illustrated along with the spectrometer placement in Fig. 73, where above the spacer are two pinholes with 200 μm and 1000 μm diameters, and below is one with 400 μm diameter. The collimation configuration is vital for the spectral measurement considering the extremely limited space inside the gantry and strong exposure, even with a minimum current of 20 μA applied during the spectral measurement.

8.3 3D printed supporting structures and the advantages

As shown in Fig. 73, the gantry was fixed at the perfectly upright position with the X-ray source at the top and the flat panel detector placed at the bottom, and therefore, the spectrometer needed to be placed upright toward the X-ray source. In order to facilitate the spectral measurement, supporting structures including a stand and a cover were fabricated to support the spectrometer system while leaving sufficient space for power supplies as well as connectors to protect the flat panel detector from excessive pressure, respectively. These two structures were specifically designed by AutoCAD software and printed by the desktop 3D printer (Makerbot, Replicator).

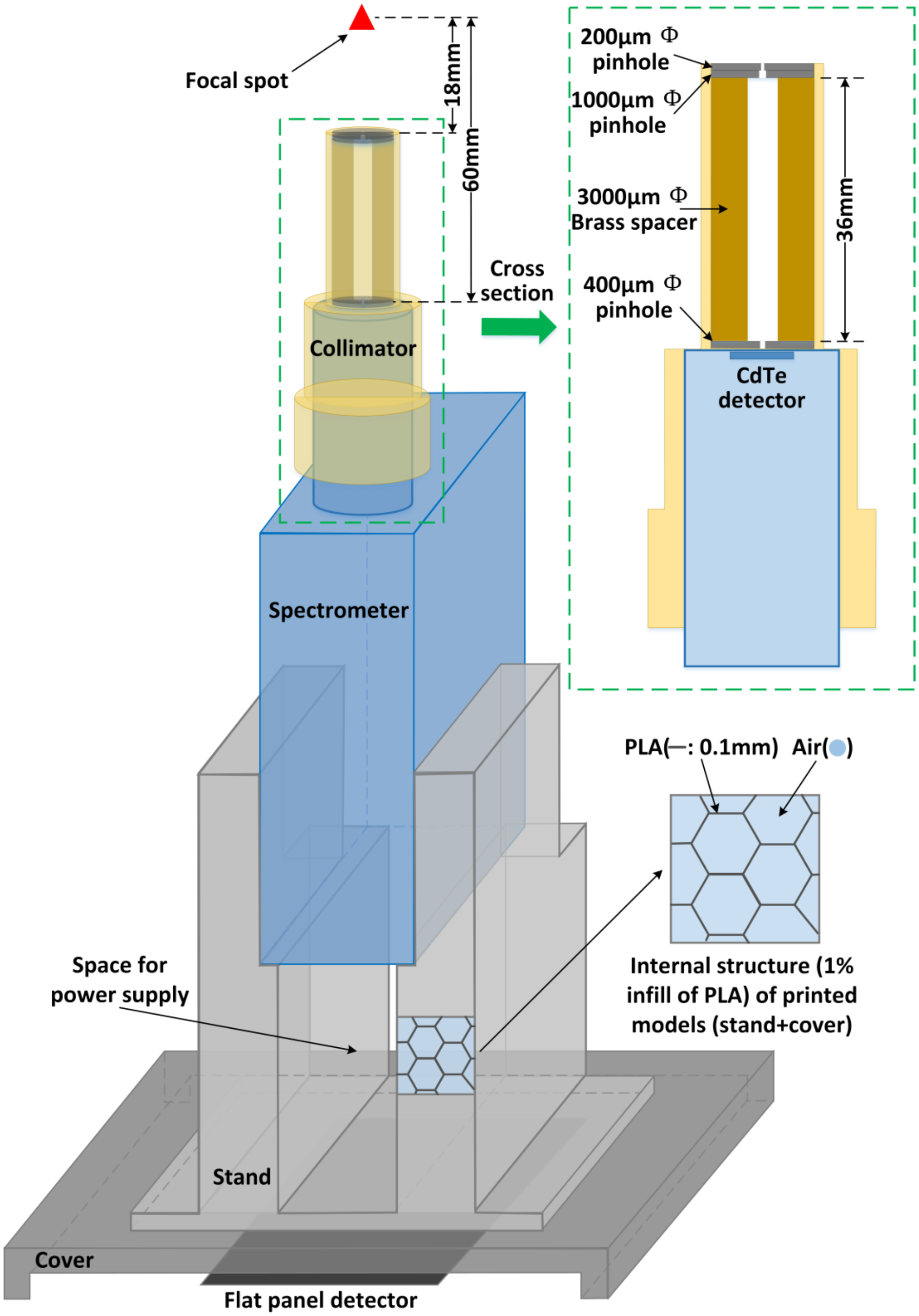

Figure 73. The spectrometer placement inside the gantry and the configuration of spectrometer collimator used for covering the CdTe detector.

Compared to conventional machining technique using materials such as metals, plastic and wood, 3D printing has more advantages in facilitating biomedical investigations in this application. First, 3D printing is easily mastered and accessible for all researchers even without prior machining experiences because the operation of a 3D printing system is sufficiently simple and safe.

Second, 3D printing provides competitive positioning precisions of 0.0004 inch in XY plane while 0.0001 inch in Z direction. Also, the paper-thin layers (100μm) ensure professional quality and high resolution of printed models, thus no further sanding, finishing, or postproduction is needed.

Third, the infill of the filament of polylactic acid (PLA) could be set as low as 1% (lower inset in Fig. 73) during the printing process while maintaining a very high solidity. This low percentage of infill has essential impacts: 1) it significantly lowers the cost of printing because it uses less materials; 2) due to the lower utilization of PLA, the printed models have lower weight compared to those if machined using other regular materials in conventional machining, as calculated in Table 7, and therefore have less pressure upon the platform such as the cover and the flat panel detector in this application; 3) the lower infill of PLA makes 3D printing a fast process from several minutes to a couple of hours, depending how low the infill percentage is and how many layers are needed, in comparison to a couple of days for conventional machining including the transportation time and communication efforts; 4) most importantly, less backscattered X-rays are caused inside the printed models, compared to a full infill of those created in conventional machining, because more X-ray photons from the primary beam could penetrate through the model rather than being interacted and backscattered, and then influencing the precise spectral measurement.

Table 7. Weight comparison of the supporting structures printed by 3D printer and conventional machining.

Material	Density (g/cm^3)	Cover weight (g)	Stand weight (g)	Total weight (g)	Infill percentage
PLA	**-**	**122.37**	**55.50**	**177.87**	**1%**
Steel	7.85	1549.59	1058.06	2607.65	100%
Copper	8.94	1764.76	1204.98	2969.73	100%
Aluminum	2.71	535.35	365.54	900.89	100%
Acrylic	1.19	234.91	160.39	395.30	100%
Glass	2.50	493.50	336.96	830.46	100%
Wood	0.85	167.79	114.57	282.36	100%

8.4 Two-step approach for spectral alignment

As shown in Fig. 73, even with careful calculations to reduce the cover thickness and to lower the spectrometer position, the source-to-spectrometer distance was still quite small due to the extremely limited space inside the gantry. Based on the estimated distances from the focal spot to the top (18mm) and the bottom (60mm) of the spectrometer collimator, the diameter of the acceptance aperture projected onto the plane of the focal spot was approximately less than 1mm, indicating that the spectral alignment and the received photon rate were very sensitive to the lateral spectrometer position [13]. Therefore, a good alignment of the spectrometer-stand assembly to the X-ray central beam was crucial for an accurate spectral measurement. Also it should be noted that considering the extremely limited distance between the X-ray focal spot and the collimator front surface, none useful information of guiding the alignment process would be observed in the acquired projection image if the spectrometer-stand assembly was directly imaged under the micro-CT live mode. Thus, a practical approach for spectral alignment and measurement in the rotating gantry based micro-CT system was proposed with two steps, a rough alignment without putting the spectrometer system onto the stand and a precise alignment through translating the spectrometer-stand assembly.

First, according to the relative position between the spectrometer system and the stand, the upright projection of the spectrometer collimator down to the stand was determined and then marked by a tungsten pinhole (2mm thick with 2000µm hole), as shown in Fig. 74. Thus, without positioning the spectrometer system on the stand, a visible alignment indicator of the X-ray central beam and the spectrometer collimator (represented by tungsten pinhole) could be established in the micro-CT live mode. In order to make sure that the spectrometer surface was perpendicular to the central beam, meaning that the tilting angle between the printed structure and the flat panel detector was acceptable (assuming that the flat panel detector is right perpendicular to the X-ray central beam), the diameters of the pinhole in two mutually perpendicular directions in the resultant projection image were calculated and compared.

Afterwards, the spectrometer was positioned back onto the stand and the precise alignment was achieved by slightly and gradually translating the spectrometer-stand assembly around the rough location back and forth until finding a “sweet spot” with the highest photon rate and proper distribution of the X-ray photons in the resultant spectrum. In order to facilitate the translation process and improve the translation efficiency and accuracy during both rough and precise alignments, two strategies were adopted to the printed cover. One was to press the cover closely against the sides of the gantry so that it is not shifted when moving the stand. The other was to mark the cover top with 2D coordinates, assisting to record the positions of the stand, so that the stand can be located in the right place determined in the rough alignment process after mounting the spectrometer. Since the stand translation was completely manual in the current study, the X-ray exposure had to completely cease during each translation.

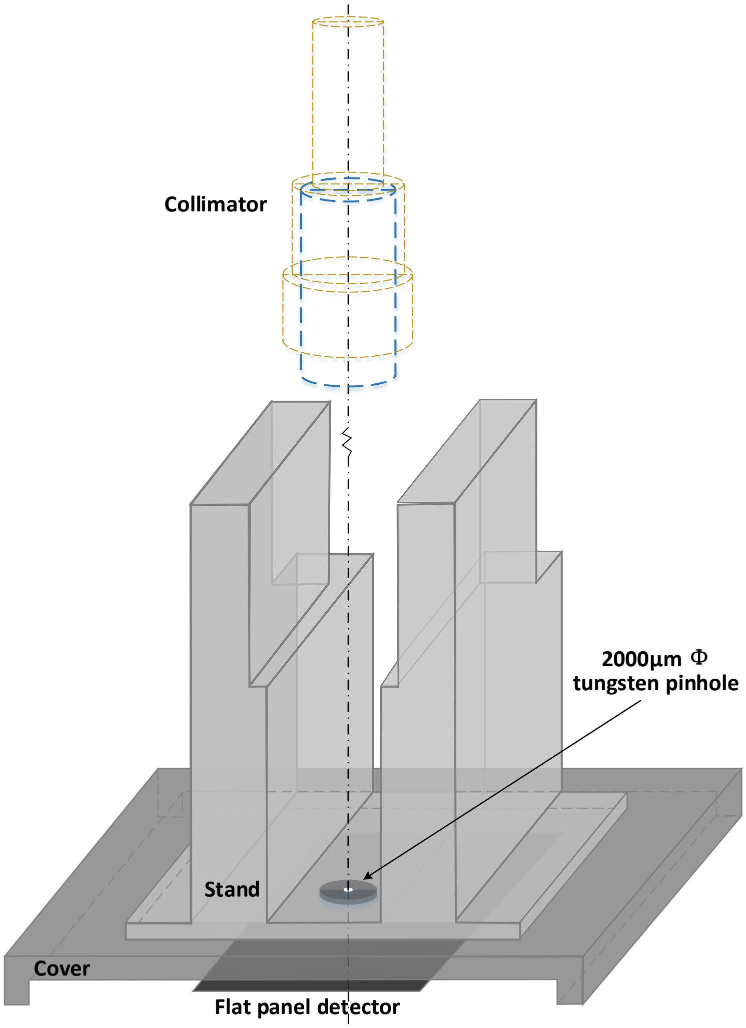

Figure 74. A tungsten pinhole was used to mark the upright projection of the spectrometer collimator onto the stand; the spectrometer system was removed from the supporting system when achieving the rough alignment.

8.5 Evaluation of measured spectra

Compared to regular spectral measurement that is operated in an open space, the measurement in a gantry based micro-CT system involves the addition of the incident primary beam and the backscattered X-rays [155]. Since most spectrum simulation software is developed for regular spectral measurement without considering the involvement of backscatter effect, these simulated spectra can't be directly utilized to verify the accuracy of spectral alignment and measurement in the current application. Instead, qualitative and quantitative analysis was performed to emphasize the importance of precise spectral alignment and to evaluate the degradation of spectra with misalignment.

As aforementioned, qualitative analysis included the observations of the received photon rate and the presences of the characteristic peaks from the X-ray tube target. On the other hand, energy resolution of the characteristic peaks and mean energy of the whole spectrum were calculated as well for the quantitative evaluation purposes. These evaluations were important because they could indicate how the precision of the spectral measurement is influenced by the misalignment between the X-ray central beam and the spectrometer device. Energy resolution (R) of the characteristic peak $K_{\alpha 1}$ and the mean energy are calculated using Eq. (12) and (16).

8.6 Results and discussion

The projection image acquired under the condition of rough alignment is shown in Fig. 75, where the two dotted lines intersect indicates the X-ray central beam direction, which coincides with the geometrical/imaging center of the flat panel detector. In order to determine the surface smoothness of the printed models and to ensure an acceptable tiling angle, the diameters of the pinhole in two mutually perpendicular directions in the projection image are calculated and compared in Fig. 75. The diameters in the mutually perpendicular directions are 24.435mm and 24.486mm, respectively, indicating a relative difference of 0.21% and a smooth surface of the printed models and an acceptable tilting angle. Also, another important advantage of using 3D printing compared to the conventional machining is that higher contrast could be achieved in the projection image due to the less infill percentage of PLA inside the printed models.

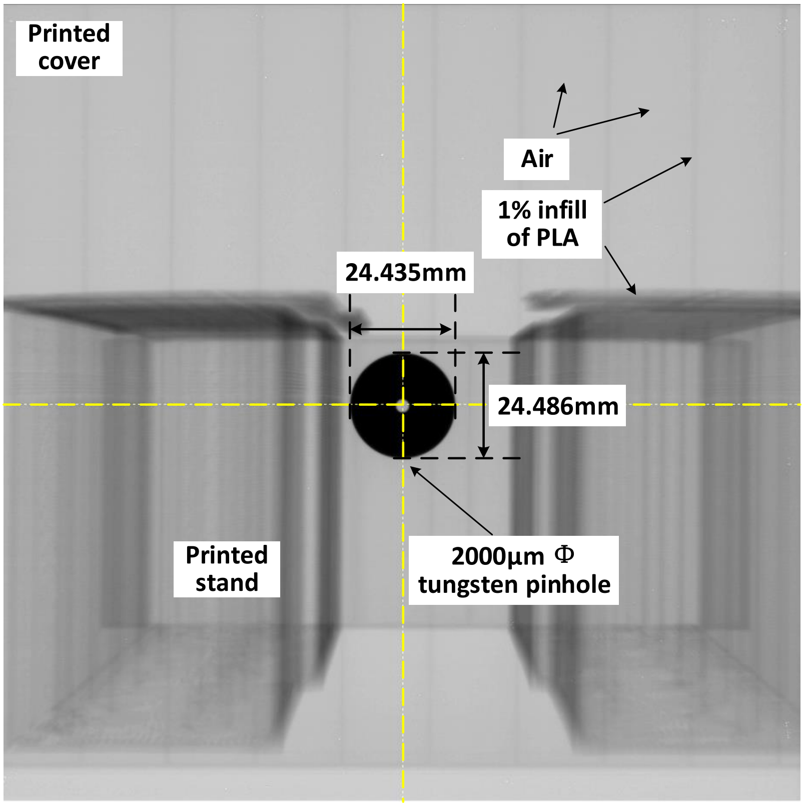

Figure 75. Determination of the rough alignment position through translating and imaging the stand as well as the pinhole.

After achieving the rough spectral alignment, the spectrometer system was mounted on the stand and precise alignment was accomplished by slightly and gradually translating the spectrometer-stand assembly around the rough location. All the spectral measurements were performed under the identical condition of 90kVp, 20μA, collimation, and duration of 100 seconds in the micro-CT live mode. The photon rate is limited to 147 photons per second per square millimeter (unit: $s^{-1}mm^{-2}$) with precise alignment. In this condition, as shown in Fig. 76 (a) - (c), the characteristic peaks (K_α and K_β) predominating the measured spectrum (solid black curve) can be clearly distinguished. As a comparison, spectra are also measured with misalignment of approximately 0.2, 0.5, and 1.0mm away from the precise alignment position, as shown in Fig. 76 (a) - (c) as well. With misalignment, not only the photon rate is reduced to $122s^{-1}mm^{-2}$, $115s^{-1}mm^{-2}$ and $46s^{-1}mm^{-2}$, but also the whole spectral distribution is distorted. With slight misalignment of 0.2mm, a small fraction of X-ray photons in the central beam is blocked by the collimator by either absorption or deflection (with reduced photon energy). The characteristic peaks first start to deteriorate because characteristic peaks occupy discrete energies and both of the X-ray photon absorption and deflection can significantly influence and reduce the photon numbers under the characteristic peaks. On the other hand, the photon number reduction in the lower energy part in the detected spectrum seems not obvious due to the compensation of deflected photons from high energy part. With more misalignment of 0.5mm, more photons in the X-ray central beam are blocked and interacted with collimators, and the characteristic peaks are further influenced. Also, more photons with low energies can’t reach the detector due to the misalignment. With further misalignment of 1.0mm which is beyond the acceptance aperture, the whole detected spectrum is totally distorted and inaccurate.

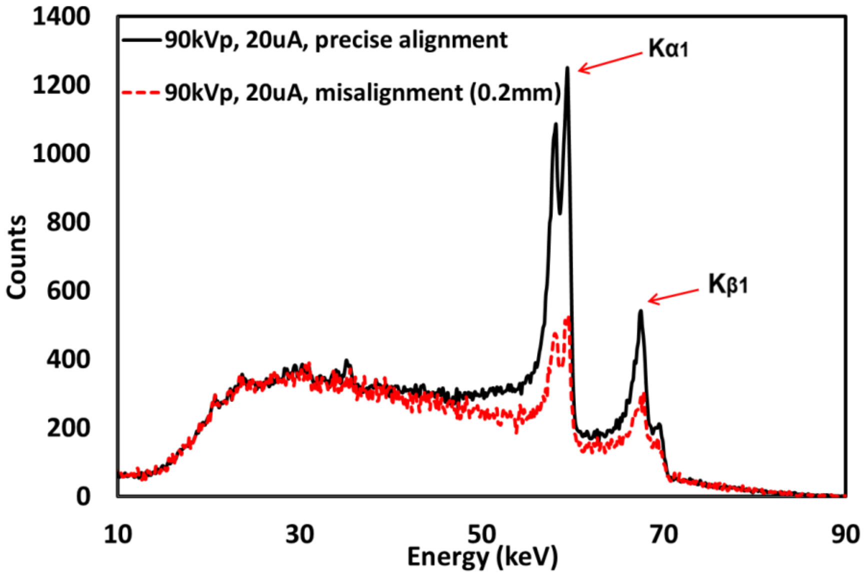

(a)

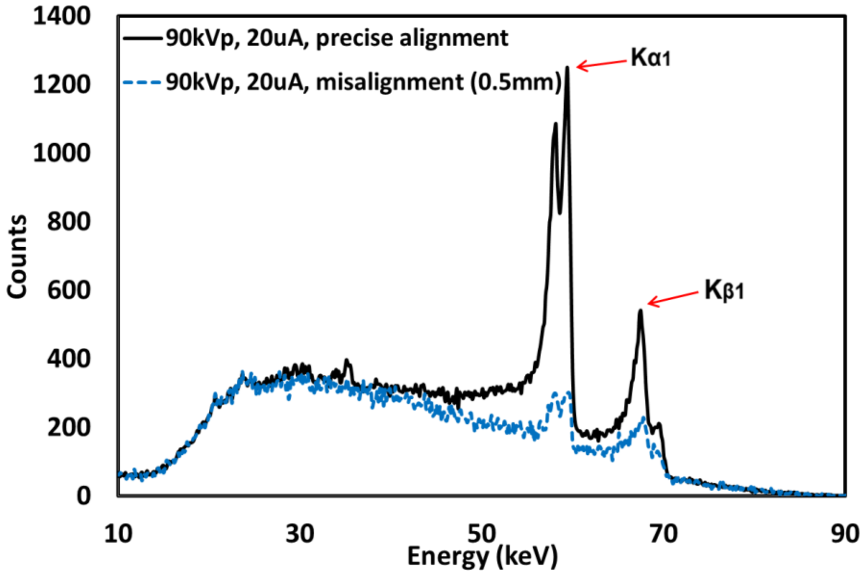

(b)

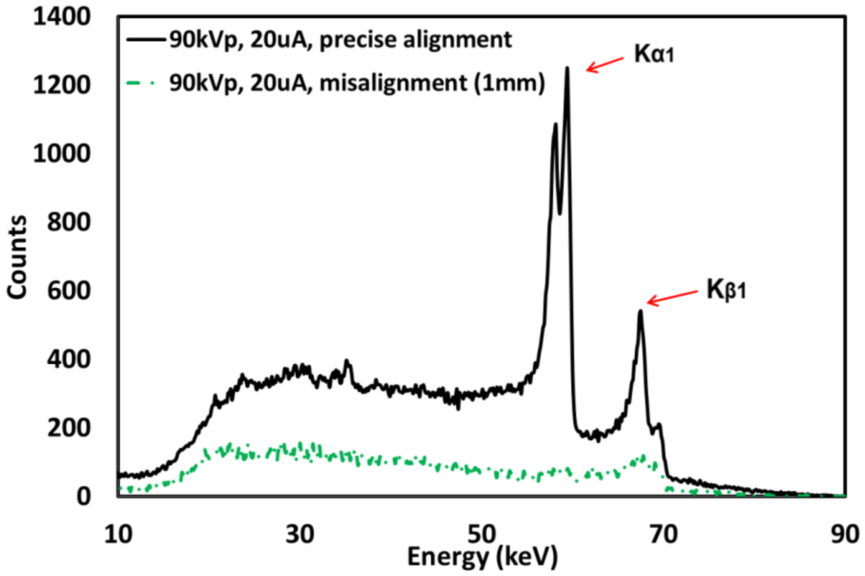

(c)

Figure 76. Comparisons of spectra acquired with precise alignment and misalignment of approximately (a) 0.2mm; (b) 0.5mm; (c) 1mm away from the precise alignment position, in terms of photon rate and characteristic peak features.

The energy resolutions for characteristic peak of $K_{\alpha 1}$ are calculated as 1.56% under precise spectral alignment, while 1.84% and 2.40% for misalignment of 0.2mm and 0.5mm. Since the characteristic peak of $K_{\alpha 1}$ has been completely diminished in the spectrum measured under misalignment of 1mm, no corresponding energy resolution can be acquired. Similarly, the mean energy is reduced from 43.93keV under precise alignment condition to 40.97, 39.63 and 37.78keV under misalignment conditions. Both of energy resolution and mean energy quantitatively indicate that the accuracy of measuring spectra is significantly influenced by the alignment precision.

Even with the coordinates marked on the cover, manual translation of the stand to reach the rough/precise alignment position is still a time-consuming process due to the cease of the X-ray exposure for each adjustment. A possible automated solution is to attach the stand and cover to a stepper motor. In this way, the translation process may be performed continuously in the micro-CT live mode, and the alignment efficiency and accuracy can be greatly improved. However, this solution would significantly increase the cost and the hardware complexity and further reduce the distance between the focal spot and the surface of the spectrometer collimator. Nevertheless, it provides the possibility to build an automated platform to realize the rough/precise alignment in rotating gantry based micro-CT systems efficiently and accurately.

8.7 Chapter summary

This chapter proposed a practical alignment method for spectral measurement in a rotating gantry based micro-CT system using 3D printing technology. Specifically, the alignment process was performed in two steps, rough alignment and precise alignment. The significance of precise alignment was indicated by comparing the spectral characteristics acquired under good alignment and misalignment conditions. The measurement results facilitate the investigation in next chapter.

Chapter 9: X-ray spectral filtration impacts in micro-CT

9.1 Chapter introduction

In this chapter, with the use of two imaging phantoms, we investigated the impact of spectral filtrations including Al, Cu and their combinations on CT number variation, noise level and image quality indicators such as CNR. Based on the evaluations of CNRs for soft tissue, muscle and bone with low density, we further analyzed the influence of spectral filtrations on low-contrast resolution, an important estimator in micro-CT imaging [156, 157]. Our overall objective is to assess the feasibility of developing and applying a new evaluation tool that can provide useful evaluation results or references for selecting the optimal scanning parameters in micro-CT systems in future imaging applications.

9.2 Materials and methods

9.2.1 Spectral measurement and evaluation

The same micro-CT scanner and X-ray spectral measurement method described in previous chapter are used. Inherent filtrations with the purpose of reducing the fluence of low-energy photons include a 150 μm thick output window of Be, 100 μm Al, and 60 μm Cu. The spectra are measured with inherent filtration and various additional spectral filtrations in the live mode under the condition of 90kVp, 200 μA and 150s. The additional spectral filtrations included Al, Cu and their combinations: 0.5mm Al, 1.0mm Al, 1.5mm Al, 2.0mm Al, 2.5mm Al, 3.0mm Al, 3.5mm Al, 4.0mm Al, 0.2mm Cu, and 0.2mm Cu + 2.5mm Al. For each measuring condition, three spectra were acquired and averaged to reduce the stochastic noise. The energy resolution (R) of the characteristic peak $K_{\alpha 1}$ was calculated using Eq. (13) to quantitatively monitor the measurement accuracy.

The beam quality was evaluated by calculating the mean energy and HVL, which provide the criteria for beam quality improvements with increasingly additional filtrations. The mean energy was directly calculated from the measured spectra using Eq. (16). In contrast, the HVL was measured using sheets of Al (type-1100) and a recently calibrated ion-chamber [22]. During the HVL measurement, the ion-chamber was flatly placed inside the gantry facing upward to the X-ray focal spot and the sensitive as well as the geometric center of the ion-chamber coincided with the isocenter of the rotating gantry.

9.2.2 Imaging phantoms and scan protocol

Two imaging phantoms were used, a uniform water phantom with a diameter of 28mm for measuring the CT number uniformity, and a water-filled mouse phantom (Model 091, CIRS, Norfolk, VA, USA) for evaluating the impact of the additional filtrations on the image quality. Note that these two phantoms were filled with deionized (DI) water to avoid any unnecessary imaging uncertainties. The mouse phantom consists of 11 rods of varying mineral loading and dimension in a water-tight, polycarbonate housing which is very durable and resistant to many chemicals. Seven rods representing different compositions (i.e. lung, muscle, adipose, and bone with various densities of 0, 50, 250 and 750mg/cc) within mammals were selected. The varied bone densities are realized through blending hydroxyapatite (HA), the principal constituent of teeth and bones within mammals, in a soft-tissue equivalent, polymer background. The cross section containing the rods of interest is shown in Fig. 77 with more detailed dimensions.

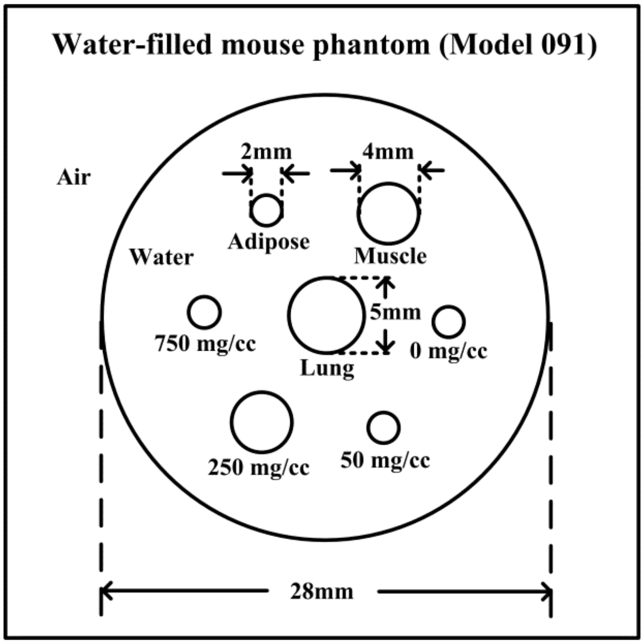

Figure 77. Schematic of the water-filled mouse phantom, the length is 30mm for the rod representing lung while 32mm for other rods.

Under each spectral filtration condition, the water phantom and the mouse phantom were scanned with 40mm FOV and 90kVp but different currents adjusted from 60 μA to 200 μA to provide the same entrance exposure to the object as a baseline for CT number uniformity and image quality comparison. The entrance exposure was measured using the same ion-chamber and in the same way as in the HVL measurements. Through adjusting the current while keeping the same exposure time (e.g. 12 s), similar exposure levels were achieved and the corresponding currents were determined for different scan conditions. Note that the process of acquiring equivalent entrance exposure was performed in the micro-CT live mode, but the determined currents were applicable to the scan mode due to the constant source-to-object distance.

Then, two CT scans, a standard scan of 17s and a fine scan of 2min, were performed on both imaging phantoms under each scan protocol.

9.2.3 CT number uniformity measurement and image quality assessment

With various spectral filtrations, the reconstructed images acquired from the water phantom were analyzed to compare the CT number uniformity, while those from the mouse phantom were to compare the CT numbers, noise levels, and CNRs of ROIs for different materials within the mouse phantom. Since the source spectrum was significantly modified with the interaction of spectral filtrations, CT number calibration was performed with two specifically selected ROIs, one for air and the other for water, before the image acquisition under each scanning setting. The averaged CT number for the air ROI was calibrated as -1000, while 0 for the water ROI. Then, eleven circular ROIs with different diameters were defined, four for water as well as bones, and one for lung, muscle, adipose each, as in Fig. 78. The mean value within each ROI in the current slice was regarded as the CT number, $Exper\_CT_k$ for that corresponding material k of interest.

In addition, the CT number for each material could be theoretically predicted using Eq. (57) with the *a priori* knowledge of mean energy and LACs. Where k indicates the material of interest (e.g. lung, muscle, adipose, bones and water) and $Theor\_CT_k$ is the theoretical CT number for material k ; $\mu_{k,ME}$ and $\mu_{bg,ME}$ represent the LACs under the mean energy for material k and background of water [22].

$$Theor\_CT_k = \frac{\mu_{k,ME} - \mu_{bg,ME}}{\mu_{bg,ME}} \times 1000 \qquad (57)$$

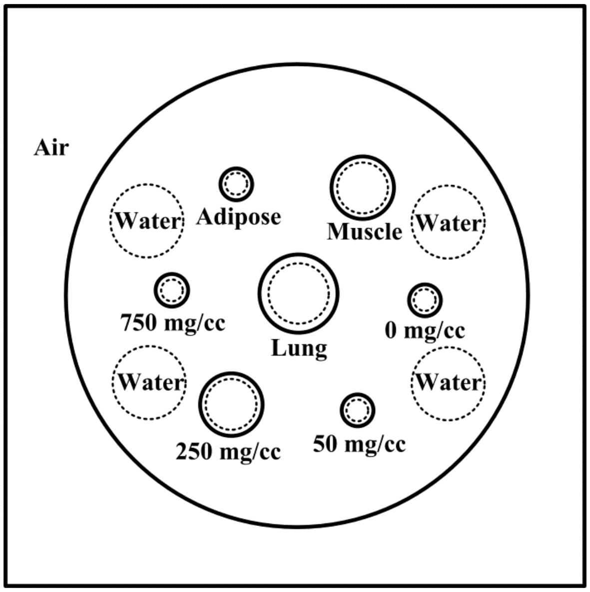

Figure 78. Eleven ROIs defined for water, lung, muscle, adipose and bones.

In order to minimize the background information such as ring artifacts, beam hardening artifacts, streaking artifacts, and cone-beam artifacts, two sequential acquisitions of the image were acquired, and the noise was calculated from the subtraction of one acquisition from the other. Specifically, the noise level (N_{bg}) was determined through dividing the standard deviation (SD) in the four water ROIs on the subtraction image by a factor of $\sqrt{2}$, as shown in Eq. (58) [158].

$$N_{bg} = SD/\sqrt{2} \qquad (58)$$

Then, the experimental and theoretical CNRs of each material of interest were calculated using Eq. (59) and (60). In Eq. (56), the relationship between theoretical CNR and LAC under mean energy for each material was established through substituting Eq. (57) and considering $Theor\_CT_{bg} = 0$.

$$Exper\_CNR_k = \frac{Exper\_CT_k - Exper\_CT_{bg}}{N_{bg}} \tag{59}$$

$$Theor\_CNR_k = \frac{Theor\_CT_k - Theor\_CT_{bg}}{N_{bg}} = \frac{\frac{\mu_{k,ME} - \mu_{bg,ME}}{\mu_{bg,ME}} \times 1000}{N_{bg}} \tag{60}$$

The standard derivations ($\sigma_{Exper\_CNR_k}$ and $\sigma_{Theor\_CNR_k}$) of experimental and theoretical CNRs were calculated using Eq. (61) and (62), where $\sigma_{Exper\_CT_k}$, $\sigma_{Exper\_CT_{bg}}$, $\sigma_{N_{bg}}$, $\sigma_{\mu_{k,ME}}$ and $\sigma_{\mu_{bg,ME}}$ were the standard derivations of $Exper\_CT_k$, $Exper\_CT_{bg}$, N_{bg}, $\mu_{k,ME}$ and $\mu_{bg,ME}$ either acquired experimentally (multiple measurements) or theoretically (e.g. curve fitting).

$$\sigma_{Exper\_CNR_k} = \frac{1}{N_{bg}} \sqrt{\sigma^2_{Exper\_CT_k} + \sigma^2_{Exper\_CT_{bg}} + \frac{(Exper\_CT_k - Exper\_CT_{bg})^2 \sigma^2_{N_{bg}}}{N^2_{bg}}} \tag{61}$$

$$\sigma_{Theor\_CNR_k} = \frac{1000}{\mu_{bg,ME} N_{bg}} \sqrt{\sigma^2_{\mu_{k,ME}} + \frac{\mu^2_{k,ME}\sigma^2_{\mu_{bg,ME}}}{\mu^2_{bg,ME}} + \frac{(\mu_{k,ME} - \mu_{bg,ME})^2 \sigma^2_{N_{bg}}}{N^2_{bg}}} \tag{62}$$

In summary, fifty consecutive slices in the reconstructed images were selected for experimental assessments of CT number, noise level and CNRs in each test.

9.3 Results

9.3.1 Spectra evaluation and current determinations

As shown in the second column of Table 8, all spectra were acquired with acceptable photon rates less than 2000 p/s corresponding to a photon flux of about 222 photons $s^{-1}mm^{-2}$ so as to avoid the pileup phenomenon. For each spectrum, the channel-to-energy calibration were performed using two characteristic peaks from K line of W, $K_{\alpha 1}$ and $K_{\beta 1}$. Then, energy resolution and mean energy were derived using Eq. (13) and (16) from the measured spectra and listed in the third and fourth column of Table 8. Due to the restriction of the received photon rate, high energy resolutions ranging from 1.46% to 2.05% were achieved. According to the calculation of mean energy and the measurement of HVL (fifth column), the beam quality was improved with increasingly additional filtrations. In the sixth column, the current (μA) for each filtration was determined to provide identical entrance exposure, as a baseline for image quality comparison with various spectral filtrations. Each entrance exposure lasted for 12 s: the values in the last column being the average of three repeated measurements, with a maximum relative deviation below 2.1%. All measured spectra are demonstrated in Fig. 79, indicating improved beam qualities with increasingly additional filtrations.

Table 8. Spectral evaluations with respect to photon rate, energy resolution and mean energy, HVL measurement in terms of the thickness of Al, and current determination; all these data were calculated or measured at 90kVp.

Additional filtration (mm)	Photon rate (p/s)	Energy resolution (R: %)	Mean energy (keV)	HVL (mm Al)	Current (μA)	Entrance exposure (12s: mR)
None	1930±55	1.65±0.15	46.68±0.11	3.48	63	474±5.0
0.5Al	1723±25	1.65±0.15	47.53±0.17	3.69	72	470±7.3
1.0Al	1552±29	1.60±0.18	47.99±0.07	3.83	80	480±6.8
1.5Al	1397±14	1.46±0.18	48.70±0.04	4.04	87	474±5.4
2.0Al	1272±32	1.89±0.00	49.01±0.17	4.34	98	471±9.9
2.5Al	1198±10	1.84±0.35	49.79±0.04	4.72	107	480±1.8
3.0Al	1102±12	1.65±0.15	50.15±0.08	4.94	118	472±2.6
3.5Al	1051±13	1.94±0.31	50.73±0.06	5.17	129	474±8.8
4.0Al	971±7	1.65±0.15	51.09±0.09	5.41	140	477±4.5
0.2Cu	938±11	1.97±0.11	51.16±0.10	5.45	144	472±8.3
0.2Cu+2.5Al	724±5	2.05±0.11	52.94±0.04	6.81	200	474±4.0

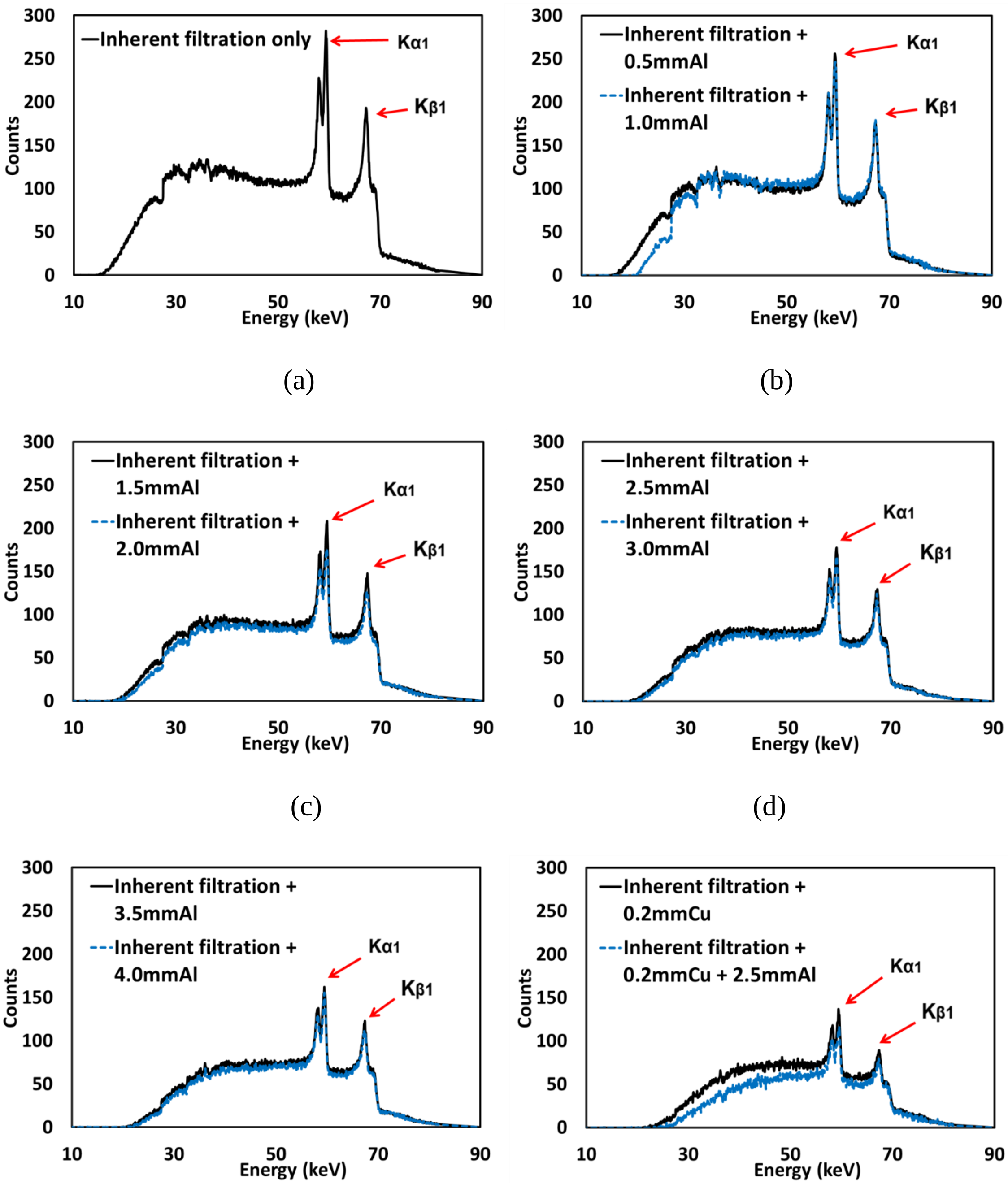

(a) (b)

(c) (d)

(e) (f)

Figure 79. Measured spectra with (a) inherent filtration only and (b)-(f) various additional filtrations.

9.3.2 CT number uniformity and image quality analysis

The CT number uniformities were compared by plotting the CT number profile of the central line in each acquired image from the water phantom. The comparison with an internal filtration only and with an additional 4mm Al filtration is presented in Fig. 80, showing that both uniformities are acceptable. This insignificant improvement may be because that the object used in this micro-CT imaging system is relatively small and the internal filtration of Al and Cu has already removed most of the X-ray photons with low energies which are the major contributor to the beam hardening effect.

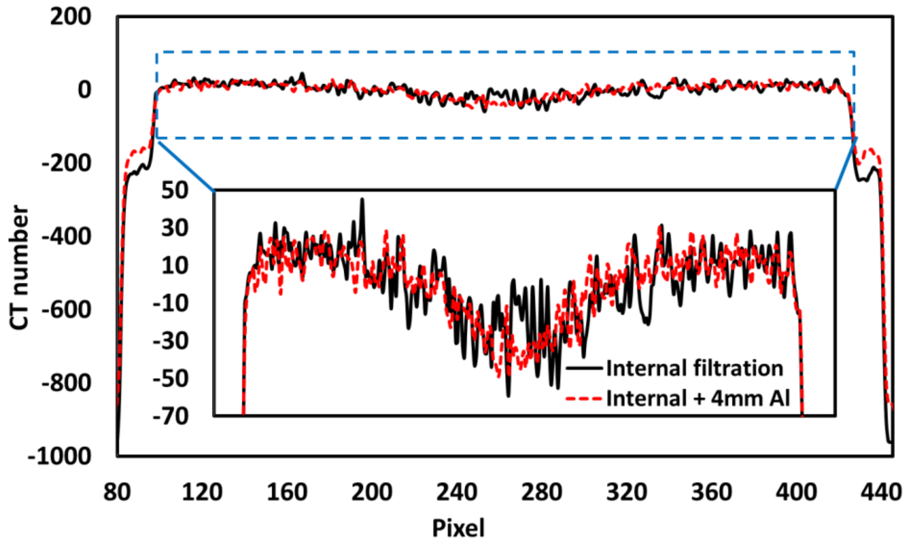

Figure 80. CT number profiles using a uniform water phantom, one with internal filtration only and the other with additional 4mm Al filtration.

Five compositions (i.e. water, air, muscle, adipose and bone with high density) were selected for the theoretical calculations and predications of CT number and CNR. The LACs of these compositions were obtained from the National Institute of Standards and Technology (NIST, USA), but only with discrete energies (e.g. 10 keV, 20 keV et. al) [132]. In order to acquire the LAC data under the mean energies (46.68 - 52.94 keV) when different spectral filtrations were utilized, a second-order polynomial fitting method was applied on the available data at the energies of 40 keV, 50 keV and 60 keV for each composition, and the fitting results are listed in Table 9. Corresponding CT number calculated theoretically using Eq. (57) is presented as well. It is not surprising that the LAC for each composition is decreased with the improved beam quality due to the increased mean energy as well as the stronger penetrability. Also, the configuration is consistent for all filtrations because the CT number in air and water are very similar or equal, while for adipose, muscle, and bone, the absolute CT numbers are monotonically decreased with increasingly additional filtrations.

Table 9. Determination of LACs (cm-1) and CT numbers (Hounsfield unit: HU) using a second-order polynomial fitting and Eq. (53).

Additional filtration (mm)	Mean energy (keV)	Water (1.00g/cm^3)		Air (0.001205g/cm^3)		Adipose (0.95g/cm^3)		Muscle (1.05g/cm^3)		Bone (1.92g/cm^3)	
		LAC	CT	LAC	CT	LAC	CT	LAC	CT	LAC	CT
None	46.68	0.238	0	2.64E-4	-998.892	0.209	-123.304	0.250	47.989	0.940	2944.062
0.5Al	47.53	0.235	0	2.60E-4	-998.893	0.207	-120.025	0.246	47.660	0.905	2848.796
1.0Al	47.99	0.234	0	2.59E-4	-998.893	0.206	-118.293	0.245	47.486	0.887	2798.434
1.5Al	48.70	0.231	0	2.56E-4	-998.894	0.204	-115.685	0.242	47.223	0.860	2722.482
2.0Al	49.01	0.230	0	2.54E-4	-998.894	0.204	-114.571	0.241	47.110	0.849	2690.035
2.5Al	49.49	0.228	0	2.51E-4	-998.895	0.202	-111.844	0.238	46.834	0.822	2610.437
3.0Al	50.15	0.226	0	2.50E-4	-998.896	0.201	-110.622	0.237	46.709	0.809	2574.734
3.5Al	50.73	0.225	0	2.48E-4	-998.896	0.200	-108.706	0.235	46.513	0.791	2518.663
4.0Al	51.09	0.224	0	2.47E-4	-998.896	0.200	-107.550	0.234	46.394	0.779	2484.795
0.2Cu	51.16	0.223	0	2.47E-4	-998.897	0.199	-107.328	0.234	46.372	0.777	2478.295
0.2Cu+2.5Al	52.94	0.219	0	2.41E-4	-998.898	0.196	-102.045	0.229	45.824	0.726	2322.955

The CT numbers acquired by experiments for water, lung, adipose, muscle and bones are shown in Tables 10 and 11 under the scan condition of 17 s and 2 min, respectively, and a reconstructed image sample of mouse phantom is shown in Fig. 81. The results of CT number determination agree with the theoretical calculations with regard to water, adipose, and bone with high density. The CT number variations of muscle and bone with low density (e.g. 50 mg/cc) are not obvious, because their LACs are quite similar as that of water, and therefore, the results are prone to be affected by the imaging noise. Since most part of the lung is composed by air, the lung CT number shows a variation tendency towards to -1000 as that of air rather than to 0.

Table 10. CT numbers (HU) determined by experiments under a standard scan of 17s: the values below being the average derived from fifty consecutive slices in the reconstructed image; the CT number symbols are indicated after the material names except water (Note: the standard deviation value is not associated with the CT number in a given slice, but is derived as the variation of CT numbers from fifty consecutive slices in the reconstructed images for each material).

Additional filtration (mm)	Water	Lung	Adipose	Muscle
None	-1.584±1.032	-631.432±108.613	-113.181±109.614	33.271±107.614
0.5Al	-4.495±1.042	-642.102±106.194	-113.952±105.102	32.771±104.603
1.0Al	-1.768±0.982	-645.553±104.812	-119.803±101.974	37.184±102.762
1.5Al	-2.172±0.990	-647.632±104.632	-105.421±102.402	37.973±102.302
2.0Al	-0.864±1.023	-647.652±102.602	-104.472±102.072	37.372±101.612
2.5Al	1.037±1.024	-649.341±101.182	-102.871±97.364	39.324±98.362
3.0Al	0.910±0.988	-650.512±101.193	-93.814±100.253	39.903±98.712
3.5Al	-0.505±0.986	-648.403±102.042	-99.403±99.962	35.432±99.703
4.0Al	-0.841±1.001	-649.451±101.321	-98.743±99.293	37.871±99.173
0.2Cu	2.489±2.032	-656.023±103.562	-90.763±100.593	40.332±99.881
0.2Cu+2.5Al	1.000±1.965	-661.301±100.762	-91.132±96.582	39.713±96.582
Additional filtration (mm)	**Bone: 0mg/cc**	**Bone: 50mg/cc**	**Bone: 250mg/cc**	**Bone: 750mg/cc**
None	-42.041±107.383	82.472±108.382	591.763±111.523	1543.741±111.532
0.5Al	-43.883±105.431	76.683±105.712	577.132±108.151	1501.132±107.215
1.0Al	-33.924±101.572	83.321±102.541	568.721±106.052	1483.112±105.045
1.5Al	-28.841±101.762	84.084±103.123	561.462±105.189	1453.204±103.741
2.0Al	-24.824±100.863	87.152±97.681	552.923±103.794	1418.161±107.314
2.5Al	-19.721±96.614	85.905±98.734	544.462±100.893	1401.784±101.052
3.0Al	-21.342±97.264	87.922±100.041	534.581±101.052	1371.182±105.142
3.5Al	-18.352±99.662	83.631±99.431	524.612±101.812	1335.183±103.653
4.0Al	-17.114±98.691	87.451±98.671	517.254±100.863	1326.264±97.426
0.2Cu	-1.813±98.762	92.312±99.441	512.413±100.774	1284.083±114.835
0.2Cu+2.5Al	-2.652±95.743	91.123±96.812	484.612±97.962	1182.583±118.071

Table 11. CT numbers (HU) determined by experiments under a fine scan of 2min: the values below being the average derived from fifty consecutive slices in the reconstructed image; the CT number symbols are indicated after the material names except water (Note: the standard deviation value is not associated with the CT number in a given slice, but is derived as the variation of CT numbers from fifty consecutive slices in the reconstructed images for each material).

Additional filtration (mm)	Water	Lung	Adipose	Muscle
None	-8.588±1.001	-642.721±48.174	-124.842±41.213	31.338±41.214
0.5Al	-8.565±0.985	-651.594±47.123	-121.341±38.844	29.261±38.194
1.0Al	-6.964±1.012	-651.162±47.043	-117.082±39.001	31.232±39.112
1.5Al	-8.016±1.032	-652.902±47.021	-115.743±38.384	29.663±39.532
2.0Al	-6.721±0.974	-651.812±46.072	-113.253±39.473	32.112±38.971
2.5Al	-4.793±0.995	-651.572±46.012	-109.274±38.593	32.663±38.523
3.0Al	-4.582±0.985	-653.402±45.232	-109.650±38.614	32.001±38.001
3.5Al	-4.780±1.015	-654.602±45.241	-107.251±38.623	33.602±37.612
4.0Al	-4.201±1.014	-655.162±45.583	-106.552±38.261	34.592±37.301
0.2Cu	-0.392±2.021	-659.331±49.421	-102.193±38.831	38.102±38.832
0.2Cu+2.5Al	-2.929±2.012	-662.041±49.672	-98.001±38.614	36.003±38.492

Additional filtration (mm)	Bone: 0mg/cc	Bone: 50mg/cc	Bone: 250mg/cc	Bone: 750mg/cc
None	-48.291±40.112	81.352±40.762	588.091±43.662	1628.621±41.832
0.5Al	-45.861±37.632	81.659±39.253	581.069±42.291	1602.741±40.925
1.0Al	-39.737±38.924	84.992±39.371	572.038±42.382	1572.101±40.412
1.5Al	-36.921±39.333	84.403±39.443	560.463±41.942	1536.771±40.325
2.0Al	-32.718±38.363	85.214±39.162	551.593±41.682	1501.982±45.565
2.5Al	-29.129±37.701	86.804±38.001	544.274±40.914	1481.413±37.864
3.0Al	-26.314±37.662	89.342±37.863	535.663±40.871	1447.834±43.505
3.5Al	-20.749±37.802	90.403±37.871	526.824±40.302	1420.723±43.065
4.0Al	-18.833±37.332	89.381±37.624	519.687±40.241	1396.775±46.562
0.2Cu	-8.041±37.615	96.923±38.221	514.692±40.704	1371.889±54.912
0.2Cu+2.5Al	-6.962±37.703	91.932±37.473	481.197±39.562	1268.388±57.803

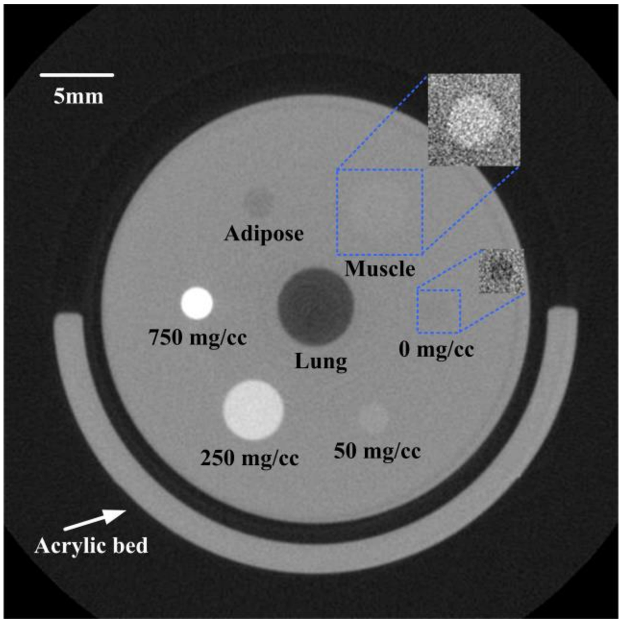

Figure 81. Reconstructed image sample of mouse phantom; the gray level values are scaled for muscle and 0mg/cc.

The results determined by Eq. (58) indicate a reduction of noise with additional spectral filtrations under both standard and fine scan, as shown in Table 12. The trends seen in the table may be caused by improved beam quality and narrower spectra with filtration. Also, the reduction of noise provides a potential to achieve improved CNR for certain materials based on the tissue characteristic.

Table 13 summarizes the theoretical CNRs and the corresponding standard derivations derived from Eq. (60) and (62) for muscle, adipose, and bone (1.92 g/cm^3), respectively, while the experimental CNRs and their standard derivations directly determined using Eq. (59) and (61) for lung, muscle, adipose and bones (0-750 mg/cc) are summarized in Tables 14 and 15. The theoretical and experimental results have high association. Both show that the CNR for bone with higher density (e.g. 1.92 g/cm^3, 750 mg/cc and 250 mg/cc) decreases with additional spectral filtrations. Similar phenomenon is also observed in soft tissue such as adipose and bone with a density of 0 mg/cc. However, opposite situations occur in lung, muscle, and bone with lower density (50 mg/cc). Thus, the imaging quality indicator in terms of CNR significantly depends on the tissue characteristic, which indicates that experimental data is needed to provide useful references or guidelines for the utilization of additional spectral filtrations in future micro-CT imaging applications.

Table 12. Noise evaluation with various spectral filtrations under the condition of standard scan of 17s and fine scan of 2min.

Additional filtration (mm)	17s	2min
None	64.987±5.718	24.111±0.829
0.5Al	64.263±5.959	23.710±0.852
1.0Al	63.534±5.585	23.424±0.712
1.5Al	63.056±5.764	23.294±0.896
2.0Al	62.571±5.583	23.120±0.746
2.5Al	61.768±5.105	22.844±0.723
3.0Al	60.900±5.591	22.737±0.808
3.5Al	60.227±5.302	22.643±0.713
4.0Al	59.907±5.478	22.453±0.779
0.2Cu	59.542±5.443	22.434±0.681
0.2Cu+2.5Al	57.924±5.091	22.322±0.725

Table 13. Theoretical CNRs for bone, adipose and muscle with additional filtrations.

Additional filtration (mm)	Bone (1.92g/cm^3)		Adipose		Muscle	
	17s	2min	17s	2min	17s	2min
None	45.303±3.993	122.102±4.205	-1.897±0.165	-5.114±0.174	0.738±0.068	1.990±0.072
0.5Al	44.330±4.114	120.152±4.322	-1.868±0.172	-5.062±0.181	0.742±0.068	2.010±0.071
1.0Al	44.046±3.861	119.470±3.622	-1.862±0.166	-5.050±0.155	0.747±0.065	2.027±0.061
1.5Al	43.175±3.947	116.873±4.498	-1.835±0.169	-4.966±0.193	0.749±0.069	2.027±0.079
2.0Al	42.991±3.837	116.349±3.757	-1.831±0.161	-4.955±0.158	0.753±0.068	2.038±0.067
2.5Al	42.262±3.486	114.271±3.610	-1.811±0.153	-4.896±0.158	0.758±0.059	2.050±0.061
3.0Al	42.278±3.889	113.238±4.030	-1.816±0.167	-4.865±0.173	0.767±0.073	2.054±0.076
3.5Al	41.819±3.677	111.231±3.501	-1.805±0.162	-4.801±0.155	0.772±0.065	2.054±0.062
4.0Al	41.477±3.782	110.666±3.826	-1.795±0.164	-4.790±0.165	0.774±0.068	2.066±0.069
0.2Cu	41.623±3.814	110.469±3.359	-1.803±0.165	-4.784±0.146	0.779±0.076	2.067±0.067
0.2Cu+2.Al	40.104±3.513	104.066±3.369	-1.762±0.159	-4.571±0.153	0.791±0.069	2.053±0.066

Table 14. Experimental CNRs with standard scan of 17s.

Additional filtration (mm)	Bone (750mg/cc)	Bone (250mg/cc)	Bone (50mg/cc)	Bone (0mg/cc)	Adipose	Muscle	Lung
None	23.779±2.706	9.130±1.894	1.293±1.672	-0.623±1.653	-1.717±1.693	0.536±1.657	-9.692±1.876
0.5Al	23.429±2.739	9.051±1.881	1.263±1.649	-0.613±1.642	-1.703±1.643	0.580±1.629	-9.922±1.891
1.0Al	23.371±2.637	8.979±1.846	1.339±1.618	-0.506±1.599	-1.700±1.612	0.613±1.618	-10.132±1.875
1.5Al	23.081±2.675	8.939±1.858	1.368±1.640	-0.423±1.614	-1.637±1.631	0.637±1.623	-10.236±1.905
2.0Al	22.678±2.652	8.850±1.837	1.407±1.566	-0.383±1.612	-1.656±1.638	0.611±1.609	-10.337±1.881
2.5Al	22.678±2.488	8.798±1.788	1.374±1.602	-0.336±1.564	-1.682±1.582	0.620±1.593	-10.529±1.855
3.0Al	22.500±2.692	8.763±1.844	1.429±1.648	-0.365±1.597	-1.555±1.652	0.640±1.622	-10.697±1.930
3.5Al	22.177±2.603	8.719±1.857	1.397±1.655	-0.296±1.655	-1.642±1.666	0.597±1.656	-10.758±1.941
4.0Al	22.153±2.598	8.648±1.860	1.474±1.653	-0.272±1.653	-1.634±1.664	0.646±1.656	-10.827±1.960
0.2Cu	21.524±2.755	8.564±1.865	1.509±1.676	-0.072±1.659	-1.566±1.695	0.636±1.678	-11.060±2.012
0.2Cu+2.5Al	20.399±2.715	8.349±1.844	1.556±1.677	-0.063±1.653	-1.591±1.700	0.668±1.668	-11.434±2.009

Table 15. Experimental CNRs with fine scan of 2min.

Additional filtration (mm)	Bone (750mg/cc)	Bone (250mg/cc)	Bone (50mg/cc)	Bone (0mg/cc)	Adipose	Muscle	Lung
None	67.902±2.908	24.747±2.001	3.730±1.695	-1.647±1.664	-4.821±1.717	1.656±1.666	-26.300±2.193
0.5Al	67.959±2.991	24.869±1.995	3.805±1.661	-1.573±1.588	-4.756±1.647	1.595±1.612	-27.120±2.214
1.0Al	67.413±2.679	24.719±1.959	3.926±1.685	-1.399±1.662	-4.701±1.671	1.631±1.670	-27.502±2.175
1.5Al	66.316±3.083	24.404±2.031	3.967±1.700	-1.241±1.689	-4.624±1.657	1.617±1.698	-27.684±2.282
2.0Al	65.254±2.884	24.148±1.964	3.976±1.699	-1.124±1.660	-4.608±1.714	1.680±1.686	-27.901±2.187
2.5Al	65.058±2.643	24.035±1.946	4.009±1.668	-1.065±1.651	-4.573±1.695	1.639±1.687	-28.312±2.204
3.0Al	63.878±2.968	23.760±1.986	4.131±1.672	-0.956±1.657	-4.621±1.706	1.609±1.685	-28.535±2.233
3.5Al	62.954±2.748	23.477±1.927	4.203±1.678	-0.705±1.670	-4.525±1.712	1.695±1.662	-28.698±2.193
4.0Al	62.396±2.997	23.333±1.966	4.168±1.682	-0.652±1.663	-4.558±1.711	1.728±1.662	-28.992±2.265
0.2Cu	61.169±3.071	22.960±1.943	4.338±1.709	-0.341±1.676	-4.538±1.736	1.716±1.748	-29.372±2.376
0.2Cu+2.5Al	56.954±3.183	21.688±1.907	4.205±1.684	-0.181±1.689	-4.259±1.735	1.744±1.725	-29.527±2.423

9.4 Discussion

Since certain bone disorders may be directly or indirectly associated with decreased BMD, better visualization of bone with low density is of significant importance in this situation. As reported in Tables 14 and 15, the CNRs of imaging low density bone (50mg/cc), when additional filtration applied, were increased by up to 20.29% and 16.29% for 17s and 2min scan, respectively, compared to the condition with no additional filtrations, since the imaging noise was greatly suppressed.

Similarly, the CNRs of imaging muscle were increased by up to 24.61% and 5.31% for 17s and 2min scan, indicating that applying additional filtrations to the micro-CT imaging system utilized in this study may also be beneficial for imaging muscle related disorders. Another potential clinical application of micro-CT imaging technique is to detect and characterize breast cancer through performing a micro-CT imaging on breast biopsy specimens [159, 160]. For this clinical utilization, the application of additional filtrations may provide better low contrast resolution when imaging micro-calcification with low density or imaging tumors with similar density (CT number) as that of muscle. Therefore, additional filtrations would be recommended under the aforementioned micro-CT imaging conditions.

Conversely, no additional filtrations would be recommended if the soft tissue such as adipose is preferentially to be visualized, because the CNRs of imaging adipose are continuously decreased by up to 6.86% and 11.66% with maximum filtration applied. Though the impact of applying additional filtrations on imaging bones with high density and lung seems extremely significant compared to imaging others, it may not be the decisive factor since their CNRs with respect to water or soft tissue background are always sufficient.

In this chapter, we demonstrated a unique experimental approach to validate the accuracy and/or reliability of applying the theoretical models developed from conventional CT systems to a dedicated micro-CT system. Comparing the experimental results with the results predicted by the theoretical models, we found that as in the derivations of CT number for water, air, muscle, adipose and bone, the corresponding LACs under the mean energy for each material were acquired by a second-order polynomial fitting of the existing data. In this way, the CT number variation of certain material with known characteristic could be determined theoretically. However, establishing an accurate theoretical model of predicting and calculating the CNR is difficult because the noise level which is central for CNR determination often needs to be detected and measured by experiments rather than using mathematical calculation. Thus, it would be useful and meaningful to develop a noise evaluation model for this micro-CT scanner using an experimental data-driven learning approach, making it possible to predict CNR variation for various scanned materials with modified beam quality.

An important issue that may affect the theoretical evaluations of CT numbers and CNRs is the utilization of the mean energy of the acquired spectrum instead of the effective energy which is defined as the mono-energetic beam of photons that has the same HVL as the investigating spectrum of photons. This is because acquiring the effective energy and the HVL, which are related to not only the spectrum property but also the material characteristic, for each specific material seems difficult or even impossible. Nevertheless, it might account for the observation that the CNRs derived in theory and by experiment are slightly inconsistent, especially for muscle and adipose. Another reason is that the muscle and adipose used for theoretical calculations may not have identical features such as density and homogeneity as for experimental investigations [132].

Spectral measurement in a micro-CT system poses great challenges due to the limited space inside the gantry. Though the photon rates in this study have been successfully reduced to an acceptable level of less than 2000 p/s through using smaller pinhole collimators (i.e. the combination of 200 µm and 400 µm), the process of spectrometer adjustment is highly reliant on the operation experience and may not be effective and reproducible each time. A possible alternative is to first measure the 90 ° Compton scattered photons from a given sample [e.g. polymethylmetacrylate (PMMA), polyethylene, and carbon electrode] with known property. Then, the actual spectrum incident upon the scattering sample can be reconstructed from the scattered spectrum using an energy correction and the Klein-Nishina function [134]. This indirect method effectively avoids the pileup phenomenon, saves the space, and more importantly, is easily repeatable with larger pinholes such as 1000 µm or 2000 µm. Also, previously reported spectral modeling techniques can be utilized to generate the X-ray spectrum and to predict the impact of spectral modifications on imaging quality indicators such as CNR discussed in this chapter [39]. However, the specificity of the modeling for certain micro-CT system needs to be verified by experiments before they can be applied for theoretical calculation and analysis.

9.5 Chapter summary

This chapter investigates the impact of additional spectral filtrations on image quality in a micro-CT system. The evaluations of CT number, noise level, and CNR were performed using a water-filled mouse phantom. The experimental results agreed well with the theoretical calculations that, with a baseline of identical entrance exposure to the imaged mouse phantom, the CNRs were degraded with improved beam quality for bone with high density and soft tissue, while those were enhanced for bone with low density, lung, and muscle. The findings in this study may provide useful references for optimizing the scanning parameters of general micro-CT systems in future imaging applications.

Chapter 10: Summary and future perspective

10.1 Summary

In summary, this dissertation applied X-ray spectral measurement and analysis methods in XRF based and micro-CT imaging modalities. Chapter 2 gave comprehensive backgrounds for X-ray spectrum measurement and analysis, XRF spectroscopic analysis, EPR effect with passive/active targeting strategies, and the importance and difficulty of X-ray spectral measurement and analysis in a rotating gantry based micro-CT system.

Chapters 3 - 7 investigated a new XRF based imaging modality, XFM, in terms of establishing a theoretical model of GNP K-shell XRF imaging system in Chapter 3, determining the optimal energy windows and corresponding neighboring energy bins for each of the gold K-shell fluorescence peaks using fluorescence-only spectra acquired in an experimental way and comparing the background removal methods quantitatively in Chapter 4, introducing a novel approach for 3D XFM of a GNP-loaded object in Chapter 5, demonstrating the feasibility of applying XFM to address the issue of accurately depicting breast tumors located posteriorly, close to the chest wall musculature in Chapter 6, and evaluating the spatial resolution in XFM imaging system through computing the MTF curves in Chapter 7. Chapters 8 - 9 presented a practical alignment method for X-ray spectral measurement in a rotating gantry based micro-CT system using 3D printing technology, based on which, the impact of spectral filtrations on image quality are comprehensively evaluated using a mouse phantom comprising 11 rods for modeling lung, muscle, adipose, and bones.

10.2 Future perspectives

With the solid foundation laid in this dissertation regarding the X-ray spectral measurement and analysis in XRF and micro-CT imaging, the future perspectives may include: (1) improvement of XRF imaging geometry by employing X-ray fan/cone beam and 1D/2D energy resolved detector arrays, in an effort to significantly reduce the imaging time; (2) radiation dose calculation and evaluation in XFM imaging systems, especially in comparison with XFCT and micro-CT imaging of small animal sized phantoms; (3) determination of optimal XRF signal acquisition time under various GNP concentrations, in order to improve the imaging efficiency; (4) applications of XFCT and XFM imaging modalities to small animal imaging, with improved imaging geometry and reasonable radiation dose level; (5) further investigations of X-ray spectral filtration impact on other aspects of image qualities such as scattering reduction, spatial resolution improvement and absorbed dose changes.

References

1. Grubbé, E.H., *Priority in the Therapeutic Use of X-rays.* Radiology, 1933. **21**(2): p. 156-162.

2. Izumi, S., et al., *High energy X-ray computed tomography for industrial applications.* Nuclear Science, IEEE Transactions on, 1993. **40**(2): p. 158-161.

3. Mould, R.F., *Röntgen and the discovery of X-rays.* The British Journal of Radiology, 1995. **68**(815): p. 1145-1176.

4. Krug, K.D., et al., *Detecting explosives or other contraband by employing transmitted and scattered X-rays*. 1997, Google Patents.

5. Fitzgerald, R., *Phase‐Sensitive X‐Ray Imaging.* Physics Today, 2000. **53**(7): p. 23-26.

6. Wilms, J., A. Allen, and R. McCray, *On the Absorption of X-Rays in the Interstellar Medium.* The Astrophysical Journal, 2000. **542**(2): p. 914.

7. Jones, K., et al., *Application of synchrotron radiation to elemental analysis.* Nuclear Instruments and Methods in Physics Research Section B: Beam Interactions with Materials and Atoms, 1984. **3**(1): p. 225-231.

8. Seibert, J.A., *The AAPM/RSNA physics tutorial for residents. X-ray generators.* RadioGraphics, 1997. **17**(6): p. 1533-1557.

9. L'Annunziata, M.F., *Handbook of radioactivity analysis*. 2012: Academic Press.

10. Boone, J.M., O. Velazquez, and S.R. Cherry, *Small-animal X-ray dose from micro-CT.* Molecular imaging, 2004. **3**(3): p. 149-158.

11. Karellas, A. and S. Vedantham, *Breast cancer imaging: A perspective for the next decade.* Medical Physics, 2008. **35**(11): p. 4878-4897.

12. Ay, M.R., et al. *The Influence of X-Ray Spectra Filtration on Image Quality and Patient Dose in the GE VCT 64-Slice Cardiac CT Scanner*. in *Bioinformatics and Biomedical Engineering , 2009. ICBBE 2009. 3rd International Conference on*. 2009.

13. Zhang, D., X. Li, and B. Liu, *X-ray spectral measurements for tungsten-anode from 20 to 49 kVp on a digital breast tomosynthesis system.* Medical Physics, 2012. **39**(6): p. 3493-3500.

14. Debertin, K. and R.G. Helmer, *Gamma-and X-ray spectrometry with semiconductor detectors.* 1988.

15. Saha, G.B., *Gas-Filled Detectors*, in *Physics and Radiobiology of Nuclear Medicine*. 2001, Springer New York: New York, NY. p. 66-74.

16. Martin, N., *Scintillation detectors for x-rays*. Measurement Science and Technology, 2006. **17**(4): p. R37.

17. Kawaguchi, S., et al., *Reconstruction of mammography x-ray spectrum by using Rayleigh and Compton scattering corrections*, in *World Congress on Medical Physics and Biomedical Engineering, September 7 - 12, 2009, Munich, Germany: Vol. 25/2 Diagnostic Imaging*, O. Dössel and W.C. Schlegel, Editors. 2009, Springer Berlin Heidelberg: Berlin, Heidelberg. p. 231-233.

18. Duan, X., et al., *CT scanner x-ray spectrum estimation from transmission measurements*. Medical physics, 2011. **38**(2): p. 993-997.

19. Meyer, P., et al., *Evaluation of the use of six diagnostic X-ray spectra computer codes*. The British journal of radiology, 2014.

20. Zhang, D., et al., *A convenient alignment approach for x-ray imaging experiments based on laser positioning devices*. Medical Physics, 2008. **35**(11): p. 4907-4910.

21. Ren, L., et al., *Three-dimensional x-ray fluorescence mapping of a gold nanoparticle-loaded phantom*. Medical Physics, 2014. **41**(3): p. 031902.

22. J. Bushberg, J.S., M. Leidholdt, Jr., J. Boone, *The Essential Physics of Medical Imaging*. Third ed. 2012: Lippincott Williams & Wilkins.

23. Kmetec, J.D., et al., *MeV x-ray generation with a femtosecond laser*. Physical Review Letters, 1992. **68**(10): p. 1527-1530.

24. LINTON, O.W., *Medical Applications of X Rays*. 1895.

25. Evans, J.P. *X-ray imaging for security applications*. 2004.

26. Baker, D.R., et al., *An introduction to the application of X-ray microtomography to the three-dimensional study of igneous rocks*. Lithos, 2012. **148**: p. 262-276.

27. Taylor, A., *Improved Demountable Crystallographic Rotating Anode X‐Ray Tube*. Review of Scientific Instruments, 1956. **27**(9): p. 757-759.

28. Ladisich, W., et al., *Total reflection X-ray fluorescence analysis with monoenergetic excitation and full spectrum excitation using rotating anode X-ray tubes*. Nuclear Instruments and Methods in Physics Research Section A: Accelerators, Spectrometers, Detectors and Associated Equipment, 1993. **330**(3): p. 501-506.

29. Tkachuk, A., et al., *X-ray computed tomography in Zernike phase contrast mode at 8 keV with 50-nm resolution using Cu rotating anode X-ray source*, in *Zeitschrift für Kristallographie - Crystalline Materials*. 2007. p. 650.

30. Chen, G.-H., et al., *Small-angle scattering computed tomography (SAS-CT) using a Talbot-Lau interferometer and a rotating anode x-ray tube: theory and experiments*. Optics Express, 2010. **18**(12): p. 12960-12970.

31. Wiesmann, J., et al., *X-Ray Diffractometry with Low Power Microfocus Sources – New Possibilities in the Lab.* Particle & Particle Systems Characterization, 2009. **26**(3): p. 112-116.

32. Espes, E., et al. *Liquid-metal-jet x-ray tube technology and tomography applications*. 2014.

33. Sugie, H., et al., *Carbon nanotubes as electron source in an x-ray tube.* Applied Physics Letters, 2001. **78**(17): p. 2578-2580.

34. Jeong, J.-W., et al., *A digital miniature x-ray tube with a high-density triode carbon nanotube field emitter*. Applied Physics Letters, 2013. **102**(2): p. 023504.

35. using XRAYLIB, C., et al., *XRAYLIB tables (X-ray fluorescence cross-section).* 2003.

36. Birks, L., et al., *Excitation of characteristic x rays by protons, electrons, and primary x rays.* Journal of Applied Physics, 1964. **35**(9): p. 2578-2581.

37. Kragh, H., *Niels Bohr and the Quantum Atom: the Bohr model of atomic structure 1913-1925*. 2012: OUP Oxford.

38. Boone, J.M., T.R. Fewell, and R.J. Jennings, *Molybdenum, rhodium, and tungsten anode spectral models using interpolating polynomials with application to mammography*. Medical Physics, 1997. **24**(12): p. 1863-1874.

39. Boone, J.M. and J.A. Seibert, *An accurate method for computer-generating tungsten anode x-ray spectra from 30 to 140 kV.* Medical Physics, 1997. **24**(11): p. 1661-1670.

40. Nyholm, R., et al., *A soft X-ray monochromator for the MAX synchrotron radiation facility.* Nuclear Instruments and Methods in Physics Research Section A: Accelerators, Spectrometers, Detectors and Associated Equipment, 1986. **246**(1): p. 267-271.

41. Boisseau, P. and L. Grodzins, *Fluorescence tomography using synchrotron radiation at the NSLS.* Hyperfine Interactions, 1987. **33**(1-4): p. 283-292.

42. Bonse, U. and F. Busch, *X-ray computed microtomography (μCT) using synchrotron radiation (SR).* Progress in biophysics and molecular biology, 1996. **65**(1): p. 133-169.

43. Krane, K.S., *Introductory nuclear physics.* 1987.

44. Alvarez, L.W., *Discovering Alvarez: Selected Works of Luis W. Alvarez with Commentary by His Students and Colleagues*. 1987: University of Chicago Press.

45. Bushberg, J.T., *The AAPM/RSNA physics tutorial for residents. X-ray interactions.* RadioGraphics, 1998. **18**(2): p. 457-468.

46. Poludniowski, G., P.M. Evans, and S. Webb, *Rayleigh scatter in kilovoltage x-ray imaging: is the independent atom approximation good enough?* Physics in Medicine and Biology, 2009. **54**(22): p. 6931.

47. Hall, H., *The theory of photoelectric absorption for X-rays and γ-rays.* Reviews of Modern Physics, 1936. **8**(4): p. 358.

48. Victoreen, J.A., *The absorption of incident quanta by atoms as defined by the mass photoelectric absorption coefficient and the mass scattering coefficient.* Journal of Applied Physics, 1948. **19**(9): p. 855-860.

49. Wagenfeld, H., *Normal and anomalous photoelectric absorption of x rays in crystals.* Physical Review, 1966. **144**(1): p. 216.

50. Dance, D.R., K.C. Young, and R.E.v. Engen, *Estimation of mean glandular dose for breast tomosynthesis: factors for use with the UK, European and IAEA breast dosimetry protocols.* Physics in Medicine and Biology, 2011. **56**(2): p. 453.

51. Eisen, Y. and A. Shor, *CdTe and CdZnTe materials for room-temperature X-ray and gamma ray detectors.* Journal of crystal growth, 1998. **184**: p. 1302-1312.

52. Knoll, G.F., *Radiation detection and measurement*. 2010: John Wiley & Sons.

53. Lin, Y., et al., *An angle-dependent estimation of CT x-ray spectrum from rotational transmission measurements.* Medical physics, 2014. **41**(6): p. 062104.

54. Zhao, W., et al., *An indirect transmission measurement-based spectrum estimation method for computed tomography.* Physics in medicine and biology, 2014. **60**(1): p. 339.

55. O. KLEIN & , Y.N., *The Scattering of Light by Free Electrons according to Dirac's New Relativistic Dynamics.* Nature 1928. **122**: p. 398-399.

56. H. Johns, J.C., *The Physics of Radiology*. Fourth ed. 1983: Springfield.

57. WX. Cong, G.W., *X-ray fluorescence sectioning.* Physics.med-ph, 2012.

58. Kawaguchi, S., et al. *Reconstruction of mammography x-ray spectrum by using Rayleigh and Compton scattering corrections*. in *World Congress on Medical Physics and Biomedical Engineering, September 7-12, 2009, Munich, Germany*. 2009. Springer.

59. Cunha, D.M., A. Tomal, and M.E. Poletti, *Monte Carlo Simulation of X-Ray Spectra in Mammography and Contrast-Enhanced Digital Mammography Using the Code PENELOPE.* Nuclear Science, IEEE Transactions on, 2013. **60**(2): p. 495-502.

60. Bottigli, U., et al., *Comparison of two portable solid state detectors with an improved collimation and alignment device for mammographic x-ray spectroscopy.* Medical Physics, 2006. **33**(9): p. 3469-3477.

61. Brezovich, I.A. and S. Jordan *A device for precision positioning and alignment of room lasers to diminish their contribution to patient setup errors*. Journal of applied clinical medical physics / American College of Medical Physics, 2007. **8**, 2398.

62. Bambynek, W., et al., *X-Ray Fluorescence Yields, Auger, and Coster-Kronig Transition Probabilities.* Reviews of Modern Physics, 1972. **44**(4): p. 716-813.

63. Zhang, D., *Toward a more clarified detective quantum efficiency methodology: Study of the DQE theory and applications*. 2009, The University of Oklahoma: Ann Arbor. p. 182.

64. Evan, D., Y. Xin, and P. Hao, *Investigation of analog charge multiplexing schemes for SiPM based PET block detectors.* Physics in Medicine and Biology, 2013. **58**(11): p. 3943.

65. R. V. Grieken, A.M., *Handbook of X-ray Spectrometry*. Second ed. 2001: CRC Press.

66. Wagner, L.K., B.R. Archer, and F. Cerra, *On the measurement of half‐value layer in film‐screen mammography.* Medical Physics, 1990. **17**(6): p. 989-997.

67. Matsukiyo, H., et al., *X-ray fluorescence camera for imaging of iodine media in vivo.* Radiological Physics and Technology, 2009. **2**(1): p. 46-53.

68. Seong-Kyun, C., et al., *X-ray fluorescence computed tomography (XFCT) imaging of gold nanoparticle-loaded objects using 110 kVp x-rays.* Physics in Medicine and Biology, 2010. **55**(3): p. 647.

69. Fu, G., et al., *Experimental demonstration of novel imaging geometries for x-ray fluorescence computed tomography.* Medical Physics, 2013. **40**(6): p. 061903.

70. Kuang, Y., et al., *Development of XFCT imaging strategy for monitoring the spatial distribution of platinum-based chemodrugs: Instrumentation and phantom validation.* Medical Physics, 2013. **40**(3): p. 030701.

71. Brouwer, P., *Theory of XRF: Getting acquainted with the principles*. 2006: PANalytical BV.

72. *X-Ray Fluorescence (XRF): Understanding Characteristic X-Rays* X-ray Fluorescence Tutorial.

73. Brunetti, A., et al., *A library for X-ray–matter interaction cross sections for X-ray fluorescence applications.* Spectrochimica Acta Part B: Atomic Spectroscopy, 2004. **59**(10): p. 1725-1731.

74. Bennal, A. and N. Badiger, *Measurement of K shell absorption and fluorescence parameters for the elements Mo, Ag, Cd, In and Sn using a weak gamma source.* Journal of Physics B: Atomic, Molecular and Optical Physics, 2007. **40**(11): p. 2189.

75. Thomsen, V., *Basic fundamental parameters in X-ray fluorescence.* SPECTROSCOPY-SPRINGFIELD THEN EUGENE THEN DULUTH-, 2007. **22**(5): p. 46.

76. Kaya, N., E. Tıraşoğlu, and G. Apaydın, *Determination of K shell absorption jump factors and jump ratios in the elements between Tm (Z= 69) and Os (Z= 76) by measuring K shell fluorescence parameters.* Nuclear Instruments and Methods in Physics Research Section B: Beam Interactions with Materials and Atoms, 2008. **266**(7): p. 1043-1048.

77. Poehn, C., J. Wernisch, and W. Hanke, *Least‐squares fits of fundamental parameters for quantitative x‐ray analysis as a function of Z (11⩽ Z⩽ 83) and E (1 keV⩽E⩽50 keV).* X‐Ray Spectrometry, 1985. **14**(3): p. 120-124.

78. Broll, N., *Quantitative x‐ray fluorescence analysis. Theory and practice of the fundamental coefficient method.* X‐Ray Spectrometry, 1986. **15**(4): p. 271-285.

79. Matsumura, Y. and H. Maeda, *A New Concept for Macromolecular Therapeutics in Cancer Chemotherapy: Mechanism of Tumoritropic Accumulation of Proteins and the Antitumor Agent Smancs.* Cancer Research, 1986. **46**(12 Part 1): p. 6387-6392.

80. Hashizume, H., et al., *Openings between Defective Endothelial Cells Explain Tumor Vessel Leakiness.* The American Journal of Pathology, 2000. **156**(4): p. 1363-1380.

81. Nehoff, H., et al., *Nanomedicine for drug targeting: strategies beyond the enhanced permeability and retention effect.* International Journal of Nanomedicine, 2014. **9**: p. 2539-2555.

82. Jeon, B.-H., et al., *Profound but Dysfunctional Lymphangiogenesis via Vascular Endothelial Growth Factor Ligands from CD11b+ Macrophages in Advanced Ovarian Cancer.* Cancer Research, 2008. **68**(4): p. 1100-1109.

83. Iyer, A.K., et al., *Exploiting the enhanced permeability and retention effect for tumor targeting.* Drug Discovery Today, 2006. **11**(17–18): p. 812-818.

84. MacEwan, S.R., D.J. Callahan, and A. Chilkoti, *Stimulus-responsive macromolecules and nanoparticles for cancer drug delivery.* Nanomedicine, 2010. **5**(5): p. 793-806.

85. Kobayashi, H., R. Watanabe, and P.L. Choyke, *Improving Conventional Enhanced Permeability and Retention (EPR) Effects; What Is the Appropriate Target?* Theranostics, 2014. **4**(1): p. 81-89.

86. James, F.H., N.S. Daniel, and M.S. Henry, *The use of gold nanoparticles to enhance radiotherapy in mice.* Physics in Medicine and Biology, 2004. **49**(18): p. N309.

87. Cai, W., et al., *Peptide-Labeled Near-Infrared Quantum Dots for Imaging Tumor Vasculature in Living Subjects.* Nano Letters, 2006. **6**(4): p. 669-676.

88. Hainfeld, J.F., et al., *Gold nanoparticles: a new X-ray contrast agent.* The British Journal of Radiology, 2006. **79**(939): p. 248-253.

89. McCarthy, J.R. and R. Weissleder, *Multifunctional magnetic nanoparticles for targeted imaging and therapy.* Advanced Drug Delivery Reviews, 2008. **60**(11): p. 1241-1251.

90. Qian, X., et al., *In vivo tumor targeting and spectroscopic detection with surface-enhanced Raman nanoparticle tags.* Nat Biotech, 2008. **26**(1): p. 83-90.

91. Bernard, L.J. and C. Sang Hyun, *The feasibility of polychromatic cone-beam x-ray fluorescence computed tomography (XFCT) imaging of gold nanoparticle-loaded objects: a Monte Carlo study*. Physics in Medicine and Biology, 2011. **56**(12): p. 3719.

92. Bernard, L.J., et al., *Experimental demonstration of benchtop x-ray fluorescence computed tomography (XFCT) of gold nanoparticle-loaded objects using lead- and tin-filtered polychromatic cone-beams.* Physics in Medicine and Biology, 2012. **57**(23): p. N457.

93. von Busch, H., et al. *Investigation of externally activated x-ray fluorescence tomography for use in medical diagnostics*. 2005.

94. Yu, K., et al., *First Demonstration of Multiplexed X-Ray Fluorescence Computed Tomography (XFCT) Imaging.* Medical Imaging, IEEE Transactions on, 2013. **32**(2): p. 262-267.

95. Cong, W., et al., *X-ray fluorescence tomographic system design and image reconstruction.* Journal of X-ray science and technology, 2013. **21**(1): p. 1-8.

96. Ahmad, M., et al., *Order of Magnitude Sensitivity Increase in X-ray Fluorescence Computed Tomography (XFCT) Imaging With an Optimized Spectro-Spatial Detector Configuration: Theory and Simulation.* Medical Imaging, IEEE Transactions on, 2014. **33**(5): p. 1119-1128.

97. Martin, S. and D. Mats, *Improved signal-to-noise ratio for non-perpendicular detection angles in x-ray fluorescence computed tomography (XFCT).* Physics in Medicine and Biology, 2014. **59**(21): p. 6507.

98. Jiang, Y.-B., et al., *Application of Micro-CT and MRI in Clinical and Preclinical Studies of Osteoporosis and Related Disorders*, in *Advanced Bioimaging Technologies in Assessment of the Quality of Bone and Scaffold Materials*, L. Qin, et al., Editors. 2007, Springer Berlin Heidelberg. p. 399-415.

99. Lerman, A. and E. Ritman, *Evaluation of microvascular anatomy by micro-CT.* Herz, 1999. **24**(7): p. 531-533.

100. Paulus, M.J., et al., *High Resolution X-ray Computed Tomography: An Emerging Tool for Small Animal Cancer Research.* Neoplasia, 2000. **2**(1–2): p. 62-70.

101. De Clerck, N.M., et al., *High-Resolution X-ray Microtomography for the Detection of Lung Tumors in Living Mice.* Neoplasia, 2004. **6**(4): p. 374-379.

102. Kiessling, F., et al., *Volumetric computed tomography (VCT): a new technology for noninvasive, high-resolution monitoring of tumor angiogenesis.* Nat Med, 2004. **10**(10): p. 1133-1138.

103. Silva, M.D., et al., *Quantitative analysis of micro-CT imaging and histopathological signatures of experimental arthritis in rats.* Molecular imaging, 2004. **3**(4): p. 312-318.

104. Badea, C.T., et al., *Lung perfusion imaging in small animals using 4D micro-CT at heartbeat temporal resolution.* Medical Physics, 2010. **37**(1): p. 54-62.

105. Louise, Y.D., et al., *A quality assurance phantom for the performance evaluation of volumetric micro-CT systems.* Physics in Medicine and Biology, 2007. **52**(23): p. 7087.

106. Hupfer, M., et al., *Dosimetry concepts for scanner quality assurance and tissue dose assessment in micro-CT.* Medical Physics, 2012. **39**(2): p. 658-670.

107. Bretin, F., et al., *Performance Evaluation and X-ray Dose Quantification for Various Scanning Protocols of the GE eXplore 120 Micro-CT.* Nuclear Science, IEEE Transactions on, 2013. **60**(5): p. 3235-3241.

108. Jantanayingyong, V., et al. *Small-sized computed tomography system with rotating gantry*. in *Electrical Engineering/Electronics Computer Telecommunications and Information Technology (ECTI-CON), 2010 International Conference on*. 2010.

109. Pillai, G., *Nanomedicines for cancer therapy: an update of FDA approved and those under various stages of development.* SOJ Pharm Pharm Sci, 2014. **1**(2): p. 13.

110. Wu, D., et al., *A method of measuring gold nanoparticle concentrations by x-ray fluorescence for biomedical applications.* Medical Physics, 2013. **40**(5): p. 051901.

111. Bazalova, M., et al., *Investigation of X-ray Fluorescence Computed Tomography (XFCT) and K-Edge Imaging.* Medical Imaging, IEEE Transactions on, 2012. **31**(8): p. 1620-1627.

112. Ren, L., et al., *Detection of posteriorly located breast tumors using gold nanoparticles: a breast-mimicking phantom study.* Journal of X-ray science and technology, 2014. **22**(6): p. 785-796.

113. Ren, L., et al., *Method for determining the modulation transfer function of X-ray fluorescence mapping system.* Optics Express, 2014. **22**(18): p. 21199-21213.

114. Hogan, J.P., R.A. Gonsalves, and A.S. Krieger, *Fluorescent computer tomography: a model for correction of X-ray absorption.* Nuclear Science, IEEE Transactions on, 1991. **38**(6): p. 1721-1727.

115. Yuasa, T., et al., *Reconstruction method for fluorescent X-ray computed tomography by least-squares method using singular value decomposition.* Nuclear Science, IEEE Transactions on, 1997. **44**(1): p. 54-62.

116. Schroer, C.G., *Reconstructing x-ray fluorescence microtomograms.* Applied Physics Letters, 2001. **79**(12): p. 1912-1914.

117. Golosio, B., et al., *Internal elemental microanalysis combining x-ray fluorescence, Compton and transmission tomography.* Journal of Applied Physics, 2003. **94**(1): p. 145-156.

118. La Rivière, P.J., et al., *Penalized-likelihood image reconstruction for x-ray fluorescence computed tomography*. Optical Engineering, 2006. **45**(7): p. 077005-077005-10.

119. H. K. Herglotz, L.S.B., *X-ray Spectrometry*. Practical Spectroscopy Series. Vol. 2. 1978, New York: Marcel Dekker.

120. Carapelle, A., et al., *Portable x-ray fluorescence spectrometer for coating thickness measurement.* Review of Scientific Instruments, 2007. **78**(12): p. 123109.

121. K, J., *Handbook of Spectroscopy*. Vol. 1. 2003, Weinheim: Wiley-VCH Verlag GmbH & Co. KGaA.

122. Ricketts, K., et al., *A quantitative x-ray detection system for gold nanoparticle tumour biomarkers.* Physics in Medicine and Biology, 2012. **57**(17): p. 5543.

123. Ryan, C.G., et al., *SNIP, a statistics-sensitive background treatment for the quantitative analysis of PIXE spectra in geoscience applications.* Nuclear Instruments and Methods in Physics Research Section B: Beam Interactions with Materials and Atoms, 1988. **34**(3): p. 396-402.

124. T. H. Wonnacott, R.J.W., *Introductory Statistics*. Fifth ed. 1990, Singapore Wiley.

125. MJ. Yaffe, N.B., *Handbook of Medical Image Processing and Analysis*. second ed. 2008, Burlington: Academic Press.

126. Wu, X., A. Yan, and H. Liu, *X-ray phase-shifts-based method of volumetric breast density measurement.* Medical Physics, 2012. **39**(7): p. 4239-4244.

127. Xingwei, W., et al., *Improving the performance of computer-aided detection of subtle breast masses using an adaptive cueing method.* Physics in Medicine and Biology, 2012. **57**(2): p. 561.

128. Zheng, B., et al., *Bilateral mammographic density asymmetry and breast cancer risk: A preliminary assessment.* European Journal of Radiology, 2012. **81**(11): p. 3222-3228.

129. James, M.L. and S.S. Gambhir, *A Molecular Imaging Primer: Modalities, Imaging Agents, and Applications.* Physiological Reviews, 2012. **92**(2): p. 897-965.

130. Helvie, M.A., et al., *Breast thickness in routine mammograms: effect on image quality and radiation dose.* American Journal of Roentgenology, 1994. **163**(6): p. 1371-1374.

131. http://jrtassociates.com/pdfs/c_014.pdf.

132. Hubbell, J.H. and S.M. Seltzer, *Tables of x-ray mass attenuation coefficients and mass energy-absorption coefficients 1 keV to 20 meV for elements z = 1 to*

92 and 48 additional substances of dosimetric interest, in *Other Information: PBD: May 1995*. 1995. p. Medium: P; Size: 116 p.

133. Johns, P.C. and M.J. Yaffe, *X-ray characterisation of normal and neoplastic breast tissues.* Physics in Medicine and Biology, 1987. **32**(6): p. 675.

134. Maeda, K., M. Matsumoto, and A. Taniguchi, *Compton-scattering measurement of diagnostic x-ray spectrum using high-resolution Schottky CdTe detector.* Medical Physics, 2005. **32**(6): p. 1542-1547.

135. Society, A.C., *Cancer Facts & Figures 2015.* Atlanta: American Cancer Society, 2015.

136. Hooley, R.J., L. Andrejeva, and L.M. Scoutt, *Breast Cancer Screening and Problem Solving Using Mammography, Ultrasound, and Magnetic Resonance Imaging.* Ultrasound Quarterly, 2011. **27**(1): p. 23-47.

137. Morris, E.A., et al., *Evaluation of Pectoralis Major Muscle in Patients with Posterior Breast Tumors on Breast MR Images: Early Experience.* Radiology, 2000. **214**(1): p. 67-72.

138. Bassett, L.W., J.J. Pagani, and R.H. Gold, *Pitfalls in mammography: demonstrating deep lesions.* Radiology, 1980. **136**(3): p. 641-645.

139. McKinley, R.L., et al. *Investigation of cone-beam acquisitions implemented using a novel dedicated mammotomography system with unique arbitrary orbit capability (Honorable Mention Poster Award)*. 2005.

140. Pan, D., et al., *Near infrared photoacoustic detection of sentinel lymph nodes with gold nanobeacons.* Biomaterials, 2010. **31**(14): p. 4088-4093.

141. Poulos, A., et al., *Breast compression in mammography: How much is enough?* Australasian Radiology, 2003. **47**(2): p. 121-126.

142. Poulos, A. and D. McLean, *The application of breast compression in mammography: a new perspective.* Radiography, 2004. **10**(2): p. 131-137.

143. Dustler, M., et al., *Breast compression in mammography: pressure distribution patterns.* Acta Radiologica, 2012. **53**(9): p. 973-980.

144. Sardanelli, F., et al., *Breast Biphasic Compression versus Standard Monophasic Compression in X-ray Mammography.* Radiology, 2000. **217**(2): p. 576-580.

145. Manohar, N., F.J. Reynoso, and S.H. Cho, *Experimental demonstration of direct L-shell x-ray fluorescence imaging of gold nanoparticles using a benchtop x-ray source.* Medical Physics, 2013. **40**(8): p. 080702.

146. Hainfeld, J.F., et al., *Micro-CT enables microlocalisation and quantification of Her2-targeted gold nanoparticles within tumour regions.* The British Journal of Radiology, 2011. **84**(1002): p. 526-533.

147. Khlebtsov, N. and L. Dykman, *Biodistribution and toxicity of engineered gold nanoparticles: a review of in vitro and in vivo studies.* Chemical Society Reviews, 2011. **40**(3): p. 1647-1671.

148. Stamper, P.C. and T.N. Tsangaris, *CT of Pectoralis Muscle Invasion by Breast Carcinoma.* Journal of Computer Assisted Tomography, 1993. **17**(5): p. 827-831.

149. Huo, Q., et al., *First experimental result with fluorescent X-ray CT based on sheet-beam geometry.* X-Ray Spectrometry, 2009. **38**(5): p. 439-445.

150. Ren, L., et al. *Background estimation methods for quantitative x-ray fluorescence analysis of gold nanoparticles in biomedical applications*. 2014.

151. Buhr, E., S. Günther-Kohfahl, and U. Neitzel, *Accuracy of a simple method for deriving the presampled modulation transfer function of a digital radiographic system from an edge image.* Medical Physics, 2003. **30**(9): p. 2323-2331.

152. Dobbins, J.T., et al., *DQE(f) of four generations of computed radiography acquisition devices.* Medical Physics, 1995. **22**(10): p. 1581-1593.

153. Jeon, H., et al., *Performance evaluation for pinhole collimators of small gamma camera by MTF and NNPS analysis: Monte Carlo simulation study.* Nuclear Instruments and Methods in Physics Research Section A: Accelerators, Spectrometers, Detectors and Associated Equipment, 2009. **604**(1–2): p. 93-96.

154. Gross, B.C., et al., *Evaluation of 3D Printing and Its Potential Impact on Biotechnology and the Chemical Sciences.* Analytical Chemistry, 2014. **86**(7): p. 3240-3253.

155. Hamza, B., et al., *Backscatter factors and mass energy-absorption coefficient ratios for diagnostic radiology dosimetry.* Physics in Medicine and Biology, 2011. **56**(22): p. 7179.

156. Sang Chul, L., et al., *A flat-panel detector based micro-CT system: performance evaluation for small-animal imaging.* Physics in Medicine and Biology, 2003. **48**(24): p. 4173.

157. Park, J.-Y., et al., *A New Micro–Computed Tomography–Based High-Resolution Blood–Brain Barrier Imaging Technique to Study Ischemic Stroke.* Stroke, 2014. **45**(8): p. 2480-2484.

158. Firbank, M.J., et al., *A comparison of two methods for measuring the signal to noise ratio on MR images.* Physics in Medicine and Biology, 1999. **44**(12): p. N261.

159. Tang, R., et al., *Micro-computed tomography (Micro-CT): a novel approach for intraoperative breast cancer specimen imaging.* Breast Cancer Research and Treatment, 2013. **139**(2): p. 311-316.

160. Willekens, I., et al., *High-resolution 3D micro-CT imaging of breast microcalcifications: a preliminary analysis.* BMC Cancer, 2014. **14**(1): p. 9.